

Fall 12-18-2020

Deciphering the Catalytic Mechanism of Human Manganese Superoxide Dismutase

Jahaun Azadmanesh
University of Nebraska Medical Center

Tell us how you used this information in this [short survey](#).

Follow this and additional works at: <https://digitalcommons.unmc.edu/etd>

 Part of the [Biochemistry Commons](#), [Biophysics Commons](#), and the [Structural Biology Commons](#)

Recommended Citation

Azadmanesh, Jahaun, "Deciphering the Catalytic Mechanism of Human Manganese Superoxide Dismutase" (2020). *Theses & Dissertations*. 508.
<https://digitalcommons.unmc.edu/etd/508>

This Dissertation is brought to you for free and open access by the Graduate Studies at DigitalCommons@UNMC. It has been accepted for inclusion in Theses & Dissertations by an authorized administrator of DigitalCommons@UNMC. For more information, please contact digitalcommons@unmc.edu.

DECIPHERING THE CATALYTIC MECHANISM OF HUMAN MANGANESE SUPEROXIDE DISMUTASE

By

Jahaun Azadmanesh

A DISSERTATION

Presented to the Faculty of
the University of Nebraska Graduate College
in Partial Fulfillment of the Requirements
for the Degree of Doctor of Philosophy

Biochemistry and Molecular Biology
Graduate Program

Under the Supervision of Professor Gloria E. O. Borgstahl

University of Nebraska Medical Center
Omaha, Nebraska

December, 2020

Supervisory Committee

Justin Mott, M.D., Ph.D.

Rebecca Oberley-Deegan, Ph.D.

Tahir Tahirov, Ph.D.

DECIPHERING THE CATALYTIC MECHANISM OF HUMAN MANGANESE SUPEROXIDE DISMUTASE

Jahaun Azadmanesh, Ph.D.

University of Nebraska, 2020

Supervisor: Gloria E. O. Borgstahl, Ph.D.

The livelihood of human cells is heavily dependent on the ability to modulate the presence of highly reactive oxygen-based molecules termed reactive oxygen species (ROS). In excess, ROS facilitate oxidative damage to the macromolecules of cellular life. SODs are the major family of antioxidant proteins that prevent the buildup of overwhelming amounts of ROS within cells. Sometimes dubbed the “first line of defense” against oxidative damage, SODs defend against the harmful accumulation of ROS by eliminating superoxide. Superoxide is a ROS itself that is also a precursor to much more harmful ROS molecules. MnSOD is the manganese containing form of human SODs that dwells within the mitochondria and is responsible for protecting the organelle against superoxide-mediated damage. The protein is arguably the most significant antioxidant enzyme as the mitochondria are especially integral for cellular vitality. This is exemplified by the embryonic lethality of mice lacking MnSOD and the multitude of human disease states that manifest as a result of dysfunctional MnSOD. The bioprotective attributes of MnSOD have attracted the attention of clinicians and is illustrated by the multiple ongoing clinical trials that attempt to mimic the function of the enzyme. While MnSOD has proven to be of significant importance for human vitality and has been studied extensively since its discovery over 50 years ago, its atom-by-atom mechanism has still been elusive and the mechanism of MnSOD has yet to be defined due to its nature of catalysis. MnSOD performs its function through concerted proton-electron transfers (CPETs) at specific sites of the enzyme that have been extremely difficult to detect experimentally. An emerging biophysical tool capable of circumventing previous experimental obstacles is neutron protein crystallography. This method involves diffracting

neutrons off of crystallized protein samples with controlled electronic states into a pattern that can be deciphered for specific proton sites thereby permitting the experimental coupling of proton and electron transfers. In this thesis work, significant revelations are made for the mechanism of MnSOD using a multitude of approaches, including neutron crystallography where significant developments are also made for the emerging technique.

Table of Contents

Table of Contents	iv
List of Figures.....	vi
List of Tables.....	vii
List of Appendix Figures.....	viii
List of Appendix Tables	viii
Abbreviations	ix
Chapter 1: Introduction.....	1
1.1 Reactive Oxygen Species and Mitochondria.....	1
1.2 Superoxide Production by the Mitochondria and Superoxide Dismutases.....	2
1.3 Human Superoxide Dismutases.....	3
1.4 Mitochondrial Preservation by Superoxide Dismutases.....	4
1.5 Mitochondrial Oxidative Damage and its Mechanisms.....	6
1.6 Catalytic Properties of Human Superoxide Dismutases	13
1.7 Kinetic Properties of Human Manganese Superoxide Dismutase	14
1.8 Production Inhibition.....	16
1.9 Dysfunction of Human Manganese Superoxide Dismutase	16
1.10 Mechanistic Insights from Previous Structures	18
1.12 Protein Crystallography	25
1.13 X-ray and Neutron Diffraction for MnSOD	31
Chapter 2: Substrate-analog Binding and Electrostatic Surfaces of Human MnSOD.....	36
2.1 Introduction	36
2.2 Materials and Methods	37
2.2.1 Protein Purification and Crystallization.....	37
2.2.2 Data Collection and Structure Determination.....	38
2.2.3 Electrostatic Surface Calculations	38
2.3 Results and Discussion	39
2.3.1 Azide Binding to Human MnSOD	39
2.3.2 Electrostatic Guidance of Anionic Substrate to the Active Site	44
2.3.3 Players in Electrostatic Guidance and Substrate Entry into the Active Site.....	45
2.4 Conclusions	49
Chapter 3: Developing a System for Neutron Diffraction of MnSOD	50
3.1 Introduction	50
3.2 Materials and Methods	51
3.2.1 Adaptation to Deuterium	51

3.2.2 Perdeuterated Expression	52
3.2.3 Purification	53
3.2.4 Crystallization.....	53
3.2.5 Deuterium Exchange	54
3.2.6 Preparation for Neutron Diffraction	55
3.3 Results and Discussion	56
Chapter 4: Redox Manipulation of MnSOD.....	63
4.1 Introduction	63
4.2 Materials and Methods	65
4.2.1 Perdeuterated Expression, Purification, and Crystallization	65
4.2.2 Redox manipulation.....	65
4.2.3 Neutron Data Collection	68
4.3 Results and Discussion	70
4.3.1 Redox manipulation.....	70
4.3.2 Optimizing Treatment Conditions and Determining Which Technique to Use	78
4.3.3 Feasibility for Neutron Diffraction.....	80
4.4 Conclusions	81
4.4.1 Mechanism of Interaction Between Redox Agents and MnSOD Crystals	81
4.4.2 Hydrogen Peroxide as a Reducing Agent and Substrate	82
4.4.3 Future Directions	83
Chapter 5: Neutron Structures of Oxidized and Reduced MnSOD	85
5.1 Introduction	85
5.2 Materials and methods.....	88
5.2.1 Perdeuterated expression, purification, and crystallization	88
5.2.2 Redox manipulation of perdeuterated MnSOD crystals	88
5.2.3 Neutron and X-ray data collection.....	88
5.2.4 Data processing and refinement	89
5.2.5 Computational Details	91
5.2.6 Bonding orbital analysis	92
5.3 Results and discussion	93
5.3.1 Direct evidence for CPETs at the active site metal with a previously unobserved and unusual glutamine deprotonation.....	93
5.3.2 Tyr34 demonstrates an unusual pK_a and forms a SSHB with the Gln143 amide anion	102
5.3.3 Serendipitous ligand binding to Mn^{2+} SOD helps explain catalysis.....	106
5.3.4 His30 has unusual pK_a that is tied to Tyr166 from across the dimer interface.....	108

5.4 Conclusions	113
Conclusions and Future Directions.....	116
6.1 Conclusions	116
6.2 Future Directions	119
Appendix 1: Preliminary Refinement of the Cryo-trapped W161F MnSOD-Peroxide Complex..	122
Introduction	122
Materials and methods.....	123
Results	125
Appendix 2: Preliminary Refinement of Y34F MnSOD in Oxidized Form.....	128
Introduction	128
Materials and methods.....	128
Results	131
References	133

List of Figures

Figure 1.1 $O_2^{\cdot-}$ production by the ETC.....	5
Figure 1.2 ROS are formed from $O_2^{\cdot-}$	8
Figure 1.3 Structure of human MnSOD.	19
Figure 1.4 Human MnSOD 5-6-5 mechanistic model.....	22
Figure 1.5 Bragg's law.	26
Figure 1.6 Processes leading to the solution of a crystal structure	30
Figure 1.7 X-ray Versus Neutron Diffraction	33
Figure 2.1 Active site geometry and electron density of azide-soaked human MnSOD.....	42
Figure 2.2 Solvent accessible electrostatic surfaces of oxidized human MnSOD with differing active site coordination.....	46
Figure 2.3 Charged surface residues that contribute to the electrostatic surface potential of human MnSOD in the Mn^{3+} -OH ₂ state	47
Figure 3.1 Fermenter growth of perdeuterated human MnSOD.....	58
Figure 3.2 Purification of human MnSOD.	60
Figure 3.3 Crystals of perdeuterated human MnSOD	61
Figure 3.4 The diffraction pattern of human MnSOD from the spherical detector orientation of MaNDi.....	62

Figure 4.1 Representative Images of Perdeuterated As-isolated, Oxidized, and Reduced Perdeuterated Human MnSOD Crystals	67
Figure 4.2 Redox Manipulation of Perdeuterated human MnSOD Crystals via Vapor Diffusion Within Capillaries.....	74
Figure 4.3 Procedure for the ‘Touch Soak’ Method for Reduction of Perdeuterated MnSOD Crystals	75
Figure 4.4 Procedure for Reducing Perdeuterated MnSOD Crystals by a Full Soak Within a Capillary	77
Figure 4.5 Effects of Crystal Size and Dithionite Treatment Method on MnSOD Crystal Integrity	79
Figure 5.1 Structure of tetrameric human MnSOD from PDB ID 5VF9	87
Figure 5.2 Proton transfer between Gln143 and the Mn-ligated solvent molecule WAT1	95
Figure 5.3 The suggested mechanism of Gln143 → WAT1 proton transfer.....	98
Figure 5.4 Differential protonations and active site coordination of MnSOD	104
Figure 5.5 Residual density for the hydroxyl group of Tyr34 in Mn ²⁺ SOD of chain B	105
Figure 5.6 Solvent accessibility differences between chains of the asymmetric AB dimer for <i>P</i> 6 ₁ 22 MnSOD	107
Figure 5.7 Differential protonation states of His30 and Tyr166 for Mn ³⁺ SOD.....	109
Figure 5.8 Protonation states of His30 and Tyr166 for Mn ²⁺ SOD	111
Figure 5.9 A suggested mechanism for MnSOD-active site proton transfers that coincide with electron gain or loss at the Mn.....	115

List of Tables

Table 1.1 Comparison of WT and Y34F MnSOD Attributes.....	34
Table 2.1 Crystallographic Data and Refinement Statistics for hMnSOD and hMnSOD-azide	40
Table 2.2 Active Site Geometry Comparisons of Native and Azide-Bound MnSOD	41
Table 3.1 X-ray and Neutron Data Collection Statistics for a 0.26 mm ³ Crystal	57
Table 4.1 Neutron Data Collection Statistics for Oxidized and Reduced Crystals	69
Table 5.1 Data collection and refinement statistics for oxidized and reduced MnSOD	90
Table 5.2 Gln143 bonding character from CLPO analysis.....	99
Table 5.3 Charge and energy interactions of donor-acceptor CLPO analysis.....	100
Table 5.4 Percent covalence of shared hydrogen atoms in SSHBs bonds from CLPO analysis....	101

List of Appendix Figures

Figure A-1.1 X-ray data of cryo-trapped peroxide at the active site of the W161F MnSOD	126
Figure A-1.2 Neutron data of cryo-trapped peroxide at the active site of the W161F MnSOD.....	127
Figure A-2.1 Preliminary structural refinement of neutron data obtained from a perdeuterated and oxidized Y34F MnSOD crystal	132

List of Appendix Tables

Table A-1.1 Data collection statistics for W161F-MnSOD-Peroxide.....	124
Table A-2.1 Data collection statistics for Y34F MnSOD.....	130

Abbreviations

ADP	Adenosine Diphosphate
ATP	Adenosine Triphosphate
C	Carbon
CPET	Concerted Proton-Electron Transfer
CuZnSOD	Copper Zinc Superoxide Dismutase
D	Deuterium
DFT	Density Functional Theory
dG	Deoxyguanosine
D ₂ O ₂	Deuterated Peroxide
DNA	Deoxyribose Nucleic Acid
EC-CuZnSOD	Extracellular Copper Zinc Superoxide Dismutase
<i>E. coli</i>	<i>Escherichia coli</i>
ETC	Electron Transport Chain
FeSOD	Iron Superoxide Dismutase
H	Hydrogen
H ₂ O ₂	Hydrogen peroxide
IC-CuZnSOD	Intracellular Copper Zinc Superoxide Dismutase
MaNDi	Macromolecular Neutron Diffractometer
MIMS	Mitochondrial Intermembrane Space
MnSOD	Manganese Superoxide Dismutase
MM	Molecular Mechanics
N	Nitrogen
NO•	Nitric Oxide
NiSOD	Nickel Superoxide Dismutase
NMR	Nuclear Magnetic Resonance
NPC	Neutron Protein Crystallography
O	Oxygen
ONOO ⁻	Peroxynitrite
O ₂ ^{•-}	Superoxide
•OH	Hydroxide
•OH	Hydroxyl Radical
QM	Quantum Mechanics
ROS	Reactive Oxygen Species
SOD	Superoxide Dismutase
SSHB	Short-Strong Hydrogen Bond
<i>T. thermophilus</i>	<i>Thermus thermophilus</i>

Chapter 1: Introduction

1.1 Reactive Oxygen Species and Mitochondria

Reactive oxygen species (ROS) are oxygen-based molecules that are characterized by high reactivity. The majority of ROS are oxidants, meaning that they abstract electrons from the molecules they interact with. At basal levels, ROS are integral to cellular processes and human vitality. Major physiological systems of the human body rely on ROS for modulating their function. For example, the cardiovascular system utilizes ROS as signaling molecules for regulating vasodilation while white blood cells of the immune system use ROS to eliminate invaders [1,2]. In excess, the high reactivity of ROS imposes deleterious consequences to cells. Copious amounts of ROS inflict havoc on the molecules of cell that may lead to dysfunction of cellular processes or death. This is especially detrimental to the human body when cardiomyocytes and neurons are the recipients of high levels of ROS. Excessive ROS in these cells correlate with the presence of cardiovascular disorders and neurodegenerative diseases [1,2]. While these are only two examples of the detrimental effects on the human body, a plethora of disease states are related with elevated levels of ROS [3].

Mitochondrion are essential for supplying cells with energy but are also responsible for the majority of endogenous cellular ROS production as a byproduct of energy metabolism [4]. To counteract the enrichment of ROS oxidants within and proximal to the organelle, evolution has provided several antioxidant systems that decrease ROS levels. This balance of ROS generation and ROS elimination composes the ROS-oxidative stress axis. A proper oxidative balance is present when antioxidant systems can properly decrease an abundance of ROS generated from mitochondrial metabolism. During this balance, ROS are prevalent only at the basal levels needed for optimal cellular function. A perturbation of the balance where ROS levels overwhelm the levels of antioxidants is termed oxidative stress [5]. Cells harbor an oxidative stress response to upregulate the expression of antioxidant genes during these periods. Such an adaptation is often

found in cell types with increased energy demands where the use of mitochondrial metabolism is elevated, such as cardiomyocytes [2]. In the event the cell's oxidative stress response is not adequate for the amount of ROS present, such as in the presence of a mutated antioxidant gene or aberrant gene regulation, oxidative damage begins to occur.

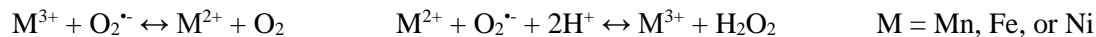
1.2 Superoxide Production by the Mitochondria and Superoxide Dismutases

The mitochondrial electron transport chain (ETC) is a group of protein complexes responsible for supplying cells with adenosine triphosphate (ATP), the 'energy currency' that powers processes within the cell. Electrons are transferred across the complexes of the ETC for the purpose of creating a proton gradient. The electrochemical gradient is then utilized by the ETC to drive the production of ATP within the mitochondria. While the mitochondrial ETC is the primary source of energy for cells, it is also the primary source of intracellular ROS [4]. Electron transport between complexes does not harbor complete fidelity due to the prevalence of electron leakage from the ETC. These leaky electrons have the potential to perform a one-electron reduction with molecular oxygen (O_2) to form superoxide ($O_2^{\cdot-}$), the first ROS created sequentially as a byproduct mitochondrial metabolism. Whereas $O_2^{\cdot-}$ is poorly reactive toward biological macromolecules, it is a precursor for the formation of highly reactive forms of ROS that are capable of causing damage to biological macromolecules. If left unmanaged, excessive amounts of $O_2^{\cdot-}$ lead to an abundance of damaging ROS that are the basis of several disease states [6].

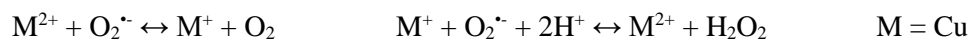
Superoxide dismutases (SODs) are antioxidant metalloproteins that are the 'first line of defense' against excessive ROS by lowering the levels of $O_2^{\cdot-}$. These metalloprotein enzymes convert $O_2^{\cdot-}$ into either O_2 or H_2O_2 depending on the redox state of the active-site metal. For all SODs excluding the CuZn isoform, a trivalent metal oxidizes $O_2^{\cdot-}$ to form O_2 while a divalent metal reduces $O_2^{\cdot-}$ with the coupling of two proton transfers to form H_2O_2 (Scheme 1) [7]. The Cu of CuZnSOD instead shuffles between divalent and monovalent states while the divalent Zn plays

only a structural role (Scheme 2). The catalytic activity of SODs can thereby consist of cyclic redox reactions of the active site metal to convert $O_2^{\cdot-}$ into its products.

Scheme 1:



Scheme 2:



The different isoforms of SODs can be defined by their core metal(s) coordinated at the active site: Ni, Fe, Cu/Zn or Mn. NiSOD is exclusive to prokaryotes while the other three are found in both prokaryotes and eukaryotes. In eukaryotes, FeSOD is found within chloroplasts, and CuZnSOD resides within the cytoplasm, mitochondrial intermembrane space (MIMS), and extracellular environment. MnSOD dwells within the mitochondrial matrix. The CuZn and Mn SODs are the only isoforms found in humans. The capacity for SODs to decrease $O_2^{\cdot-}$ levels within cells is associated with longevity and the presence or absence of disease states. Each human isoform seems to play a preventive role in specific pathologies that reflects their location [8].

1.3 Human Superoxide Dismutases

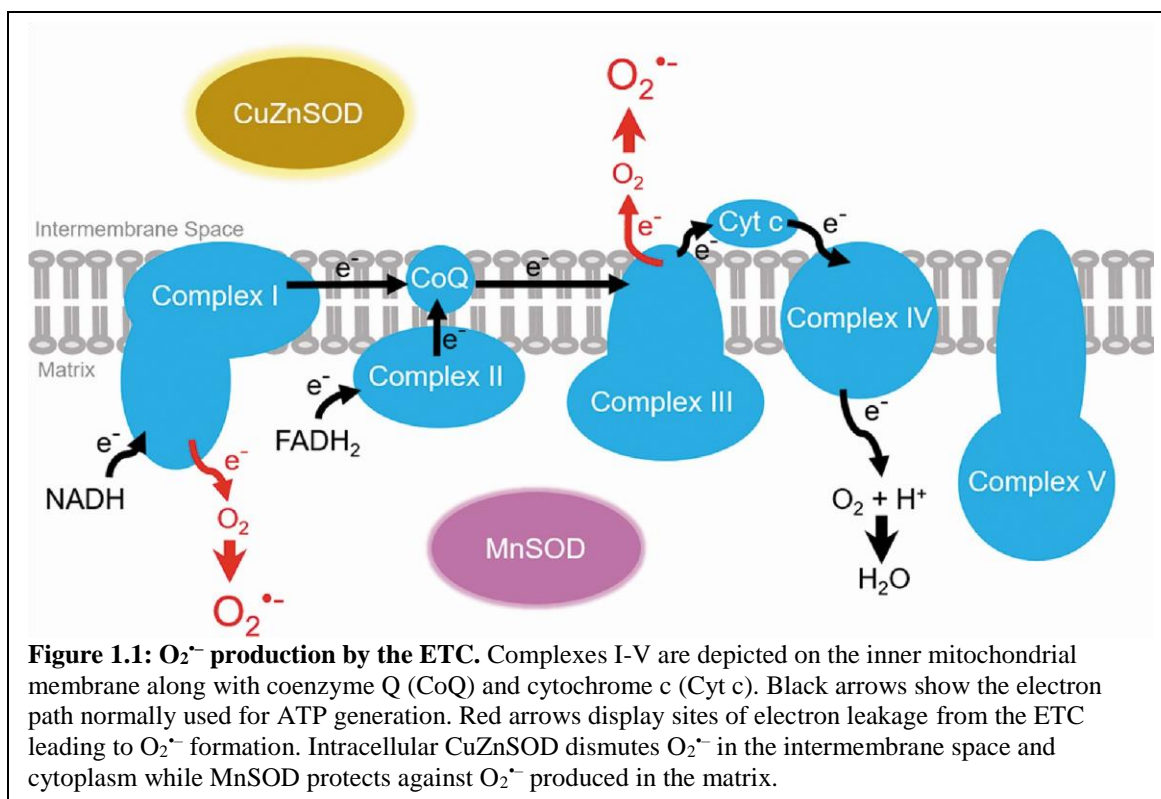
The two human isoforms of CuZnSOD, intracellular-cytoplasmic/MIMS and extracellular forms (hereafter referred to as IC-CuZnSOD and EC-CuZnSOD, respectively), are 60% homologous with similar active site architecture and are likely to follow the same catalytic mechanism [9,10]. EC-CuZnSOD residing within the extracellular environment provides cells a defense against $O_2^{\cdot-}$ generated from exogenous or environmental stress. EC-CuZnSOD does not seem to play a direct role in shielding mitochondria against ROS [11]. It is nonetheless vital in preventing oxidative effects outside cells, such as fibrosis in chronic obstructive pulmonary disease [9]. In regards to preserving mitochondrial function, the residence of IC-CuZnSOD within the MIMS is of major importance in conjunction with the mitochondrial MnSOD.

For humans, IC-CuZnSOD compromises 90% of total SOD within a cell [12]. While MnSOD constitutes only a small fraction of total SOD, its specific concentration within mitochondria is significant due to the high levels of ROS production by the organelle [4]. IC-CuZnSOD and MnSOD work in tandem to avert mitochondrial degeneration, as observed in knockout mice [12]. Mice lacking IC-CuZnSOD have ~70% of the lifespan compared to their wildtype counterparts [13]. These knockout mice appear normal during weaning but develop adult-onset neuropathies as a consequence of mitochondrial dysfunction, which includes motor neuron degeneration and axonal damage [14]. Knockout mice of MnSOD die within the first ten days of life due to impairment of mitochondrial function in neurons and cardiac myocytes [15,16]. Together, IC-CuZnSOD and MnSOD are vital in preserving the mitochondria and thereby cellular function.

1.4 Mitochondrial Preservation by Superoxide Dismutases

Among the mitochondrial ETC members involved in shuttling electrons, complexes I and III are the dominant sites of electron leakage for $O_2^{\cdot-}$ formation (Figure 1.1). Complex I leaks toward the mitochondrial matrix whereas complex III leaks toward the intermembrane space [17]. Due to the permeability of the outer mitochondrial membrane, ROS may freely diffuse to the cytoplasm after passing through the intermembrane space. Conversely, $O_2^{\cdot-}$ that is generated because of complex I electron leakage is confined within the matrix. This compartmentalization of $O_2^{\cdot-}$ generation requires similar assortment of SODs to counteract the deleterious effects of the ROS.

IC-CuZnSOD cannot compensate for lack of MnSOD and vice versa which reflects their non-redundant and strategic locations [11]. The presence of IC-CuZnSOD in the intermembrane space and cytoplasm safeguards against $O_2^{\cdot-}$ produced from complex III while the residence of MnSOD in the matrix dismutates $O_2^{\cdot-}$ formed by complex I. However, $O_2^{\cdot-}$ within the matrix is more



detrimental because of its confinement by the inner mitochondrial membrane, as ROS produced in the intermembrane space can diffuse to the cytoplasm. This explains why mice lacking MnSOD have a significantly short lifespan (< 10 days) compared to mice without IC-CuZnSOD (120 weeks) [11].

1.5 Mitochondrial Oxidative Damage and its Mechanisms

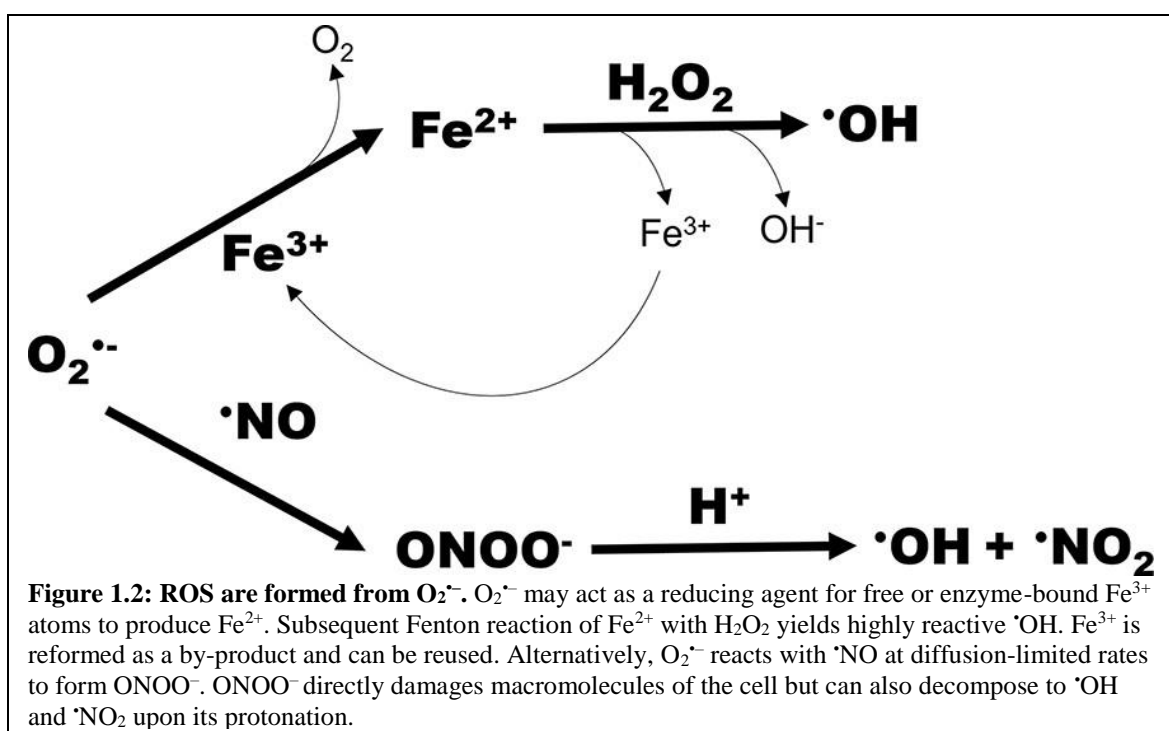
Precise workings of biological macromolecules are instrumental for the preservation of life. These include proteins that act as biological catalysts, DNA that stores genetic information and is used to produce protein, and lipids that compose the semi-permeable membrane of cells. It is therefore in the interest of cells to maintain the integrity of these macromolecules to prevent dysfunction or death by utilizing their antioxidant systems. However, when the antioxidant systems become overwhelmed from excessive amounts of ROS, damage occurs due to the high-reactivity oxidative nature of ROS. This leads to protein inactivation, DNA fragmentation, and alterations to the permeability of the cell membrane due to lipid peroxidation [18].

Cells are especially vulnerable to oxidative damage of the mitochondria. If oxidative damage causes mitochondrial energy supplying processes to malfunction, cells will lack the needed energy levels for life and die [19]. Excessive ROS levels are the cause of a significant number of diseases that manifest due to mitochondrial-related cell death [20]. The presence of these damaging amounts of ROS requires copious amounts of $O_2^{\cdot-}$. While $O_2^{\cdot-}$ itself reacts poorly with biological macromolecules, it reacts with other endogenous small molecules, such as nitric oxide ($\cdot NO$), to create products that are capable of harming mitochondria [21,22]. Within this section, the mechanism in which $O_2^{\cdot-}$ and its derivatives harm mitochondria is briefly discussed.

The basis for the bio-protective significance of SODs is the removal of the $O_2^{\cdot-}$ precursor that contributes to the formation of detrimental ROS. $O_2^{\cdot-}$ is capable of reacting with several molecules to produce injurious reactive species, such as peroxynitrite ($ONOO^-$), hydroxyl radical

($\cdot\text{OH}$), and nitrogen dioxide ($\cdot\text{NO}_2$) (Figure 1.2). All these molecules are highly reactive and capable of damaging the cellular macromolecules such as DNA, proteins, and lipids [4,23]. ONOO^- is a product of a reaction between $\text{O}_2^{\cdot-}$ and $\cdot\text{NO}$. The source of endogenous $\cdot\text{NO}$ are nitric oxide synthases (NOSs), which carry out physiological signaling in processes such as vasodilation and inflammation [24]. There are three isoforms of NOS: NOS1, NOS2, and NOS3, each being cell/tissue type specific [25]. Depending on the cell type, more than one NOS isoform may be expressed with subcellular-specific localization, such as the Golgi apparatus or mitochondria [26]. $\cdot\text{NO}$ is a potent signaling molecule due to its ability to diffuse across membranes freely. Produced in the mitochondria it encounters the $\text{O}_2^{\cdot-}$ confined in the mitochondria may encounter $\cdot\text{NO}$ produced within or out the organelle, formation of harmful ONOO^- within the mitochondria [27]. The likelihood of ONOO^- formation both within and outside the mitochondria is high given that the reaction between $\text{O}_2^{\cdot-}$ and $\cdot\text{NO}$ is diffusion-limited, meaning that every time a pair of the two molecules collide, ONOO^- is formed [24]. Another contributing factor to the likelihood of ONOO^- production is the concentration of $\cdot\text{NO}$. At basal physiological conditions, the concentrations of $\cdot\text{NO}$ are similar to the concentrations of endogenous SODs [24], meaning there is a delicate balance among the concentrations of $\text{O}_2^{\cdot-}$, SODs, and $\cdot\text{NO}$ that minimize ONOO^- formation in physiologically normal (i.e., under low oxidative stress) cells. A disruption in this balance increases oxidative stress, such as neuroinflammation that increases the levels of $\text{O}_2^{\cdot-}$ and $\cdot\text{NO}$ production, raising the amount of ONOO^- proportionally.

There are several ways that ONOO^- contributes to mitochondrial dysfunction. It can react with Fe-S clusters found in several crucial mitochondrial proteins, removing a Fe^{2+} atom, and inactivating them. Free Fe^{2+} can then lead to $\cdot\text{OH}$ formation via the Fenton reaction [28]. One example of vital mitochondrial protein inactivation is aconitase, which isomerizes citrate to isocitrate in the citric acid cycle. Aconitase Fe-S cluster inactivation contributes to mitochondrial dysfunction, cell death, and neurodegeneration as a result of the release of free Fe^{2+} [29]. Similarly,



ONOO⁻ can react with Fe-S clusters found in complexes of the ETC, irreversibly inactivating them and disrupting ATP synthesis [28]. However, it is debated whether the Fe-S clusters of the ETC are somehow resistant to oxidative damage [30]. ONOO⁻ contributes to a cascade of reactions that promote [•]OH formation and ATP synthesis inactivation.

ONOO⁻ can also inactivate proteins through reaction with amino acids. For example, ONOO⁻ can oxidize critical cysteine active site residues of enzymes and inactivate catalysis. Inactivation of tyrosine phosphatases by ONOO⁻ oxidation is especially noteworthy [24], as this foregoes loss of anti-apoptotic signaling cascades in brain cells, leading to programmed cell death [31]. ONOO⁻ can also oxidize methionine to form methionine sulfoxide, which can modulate enzyme activities. Excessive methionine sulfoxide formation correlates with development of Alzheimer's disease in brain tissues [24]. Both IC- and EC-CuZnSODs can be inactivated by ONOO⁻ by reacting with the active site metal and active site histidine to form a histidinyl radical, decreasing functional amounts of antioxidant systems [24]. ONOO⁻ oxidizes and inactivates complexes of the ETC and antioxidant proteins that contribute to mitochondrial dysfunction.

A large part of mitochondrial toxicity is lipid peroxidation initiated by the decomposition products of ONOO⁻, [•]OH and [•]NO₂ (Figure 1.2). These decomposition products are discussed in the subsequent paragraphs. Peroxidation of phospholipids is a prominent marker of mitochondrial dysfunction and neurodegeneration [32]. The direct effects of lipid peroxidation by [•]OH and [•]NO₂ are also explored in the subsequent paragraphs.

ONOO⁻ also damages mitochondrial DNA and culminates in cell death by dysregulation of mitochondrial processes [6,24]. In particular, guanine is the most susceptible to oxidation by ONOO⁻, which results in its fragmentation. This process induces mutagenesis and double-strand breaks of mitochondrial DNA. ONOO⁻ can also attack the sugar backbone of DNA to cause single-strand breaks. These damaging processes of ONOO⁻ to mitochondrial DNA (and nuclear DNA) are strongly related to cell death and inflammation, which ultimately generate additional ROS [24].

$\cdot\text{OH}$ is highly reactive and can damage neighboring molecules at near diffusion-limited rates [33-35]. Considered as the most biologically active and damaging free radical, $\cdot\text{OH}$ is a strong contributor to mitochondrial dysfunction that can lead to neurodegenerative pathologies [36,37]. Generation of $\cdot\text{OH}$ can occur through two reactions within mitochondria (Figure 1.2). First, a redox reaction of H_2O_2 with free Fe^{2+} leads to the formation of $\cdot\text{OH}$ with Fe^{3+} and hydroxide ion (OH^-) as byproducts [36]. This reaction is also known as the Fenton reaction. In the presence of $\text{O}_2^{\cdot-}$, pools of the reactants for this pathway of $\cdot\text{OH}$ generation (H_2O_2 and Fe^{3+}) are increased. Concentration of H_2O_2 is increased during an increase of $\text{O}_2^{\cdot-}$ concentration due to catalysis by SODs (Scheme 1). Free Fe^{2+} becomes available as a result of $\text{O}_2^{\cdot-}$ donating an electron to Fe^{3+} found in Fe-S cluster proteins of the mitochondria to generate Fe^{2+} and oxygen (Figure 1.2; top pathway). Fe in the divalent form favors disassociation from these clusters. Of note, these Fe-S clusters are abundant among proteins. Free Fe^{3+} , a product of Fenton chemistry, can also be used to produce Fe^{2+} . Second, at physiological conditions, ONOO^- is protonated and degrades to $\cdot\text{OH}$ and $\cdot\text{NO}_2$ (Figure 1.2; bottom pathway) [38]. At 37 °C, the pK_a of ONOO^- is 7.5. The mitochondrial matrix has a pH of 7 while the cytosol has a pH of 7.4, meaning that protonation of ONOO^- is likely, with protonation more common in the mitochondrial matrix due to its lower pH value [39].

$\cdot\text{OH}$ plays prominent roles during oxidative stress, specifically in the presence of O_2 . Furthermore, neurodegenerative diseases correlate with the prevalence of $\cdot\text{OH}$ formation [40]. $\text{O}_2^{\cdot-}$ is a precursor of $\cdot\text{OH}$, meaning the concentrations of $\text{O}_2^{\cdot-}$ and the activity of SODs influence the amount of $\cdot\text{OH}$ formation within the mitochondria and cytosol. This highly biologically reactive free radical interacts with mitochondrial proteins, lipids, and DNA, leading to the deterioration of the mitochondria.

Macromolecular proteins are highly vulnerable to denaturation by $\cdot\text{OH}$ because tyrosine and tryptophan amino acid residues are susceptible to oxidation. Upon exposure to $\cdot\text{OH}$, tyrosine residues bind other tyrosines covalently, and insoluble protein aggregates form due to this covalent

modification [46]. Tryptophan is also rapidly degraded by $\cdot\text{OH}$ [41]. Given the abundance of these two residues in proteins, the presence of $\cdot\text{OH}$ leads to aggregation, direct fragmentation, and intracellular proteolysis of critical proteins central for mitochondrial function.

$\cdot\text{OH}$ initiates the peroxidation of phospholipids and is a prominent marker of mitochondrial dysfunction and neurodegeneration [32]. Phospholipid peroxidation increases membrane permeability, which is catastrophic to the mitochondrial inner membrane because a large part of its biochemical function relies on a gradient of molecules between the mitochondrial matrix and MIMS [42]. A notable example of a process affected by increased membrane permeability is the generation of ATP by oxidative phosphorylation. The proton gradient that drives phosphorylation of ADP to ATP is disrupted by membrane permeability, leading to attenuated ATP synthesis. Various transporters and respiratory enzymes needed to maintain mitochondrial function and ATP synthesis are also affected by MIMS permeability. Peroxidation can also exacerbate neurological dysfunction during neuroinflammation. Lipids of myelin sheaths can undergo peroxidation by $\cdot\text{OH}$ leading to demyelination, causing impaired conductance of nerve signals [43]. Hence, peroxidation of lipids by $\cdot\text{OH}$ poses deleterious consequences to both mitochondrial function and neurological function.

One of the principal products of DNA oxidation is 8-oxo-2'-deoxyguanosine (8-oxo-dG), which is generated by the addition of $\cdot\text{OH}$ [44,45]. Mitochondrial DNA is especially susceptible to oxidation compared to nuclear DNA given that $\text{O}_2^{\cdot-}$ generation is more prominent within the mitochondrial matrix. The DNA adduct, 8-oxo-dG can lead to mutagenesis [46]. Mutations of the mitochondrial DNA may lead to aberrant protein function, including those of the ETC, leading to further electron leakage, subsequent $\text{O}_2^{\cdot-}$ generation, and exacerbating oxidative insults to the mitochondria [44,45]. Also, $\cdot\text{OH}$ can attack the sugar moieties of mitochondrial DNA that result in DNA strand breaks. Thus, $\cdot\text{OH}$ contributes to mitochondrial dysfunction by damaging the protein-encoding genes of mitochondrial DNA.

Similarly to other reactive species, $\cdot\text{NO}_2$ also contributes to mitochondrial dysfunction by damaging molecules that maintain the vitality of this organelle. For example, $\cdot\text{NO}_2$ reacts with tyrosine to form 3-nitrotyrosine, adding a bulky element and lowering the pK_a of the hydroxyl group 2–3 units [47]. When the nitro group causes steric restrictions for catalysis, or if a protonated hydroxyl group is required for hydrogen bonding critical to activity, then 3-nitrotyrosine can inactivate the enzyme. MnSOD is especially susceptible to inactivation by nitration of Tyr34, located at its active site [48]. The nitro group sterically impedes the substrate access funnel that $\text{O}_2^{\cdot-}$ can enter and lead to nearly complete inhibition of MnSOD activity. This inactivation of MnSOD promotes further oxidative stress by compromising the central mitochondrial anti-oxidant system. Other critical mitochondrial proteins that are vulnerable to inactivation by nitration include cytochrome c, voltage-dependent anion channel, and enzymes of the citric acid cycle [49,50]. Excessive nitration ultimately leads to the formation of the permeability transition pore that leads to apoptosis [47].

NO_2 initiates lipid peroxidation [49] and causes mitochondria DNA damage [51]. As a radical, NO_2 can abstract hydrogen atoms from either lipids or the sugar backbone of DNA to form lipid or sugar radicals, respectively. Lipid radicals either propagate formation of other lipid radicals by further abstracting hydrogen atoms from neighboring lipids or end up as peroxy radical groups from the addition of O_2 at the radical site. Membrane-bound proteins, such as those of the ETC, require particular lipid environments for their actions and are hampered by adjacent products of lipid peroxidation [57]. Sugar radicals lead to strand breaks of the mitochondrial DNA. Studies suggest that mitochondrial DNA damage plays a causative role to neurodegeneration [52,53]. Lipid peroxidation and mitochondria DNA damage are hallmarks of mitochondrial dysfunction and neurodegenerative diseases.

While the majority of $\text{O}_2^{\cdot-}$ mediated damage is a consequence of it acting as a precursor to form reactive species, there exists a direct mechanism of $\text{O}_2^{\cdot-}$ damage to the mitochondria. Like

ONOO⁻, O₂⁻ liberates Fe atoms from Fe-S clusters that normally act as needed cofactors for the enzymatic function of several mitochondrial proteins [54]. In particular, several enzymes of the citric acid cycle and amino acid biosynthesis pathway contain these clusters and are vulnerable to O₂⁻ mediated inactivation [54,55]. Consequently, excessive O₂⁻ levels in the mitochondria cause an elevation of free-iron levels. High free iron levels coupled with large amounts of H₂O₂ (such as from increased SOD activity due to high amounts of O₂⁻) instigates Fenton reaction to produce copious sums of [•]OH (Figure 1.2). The damage to Fe-S by O₂⁻ and increased Fe levels underlie mitochondrial dysfunction and neurodegenerative disease progression [56,57].

High levels of H₂O₂ are cytotoxic as it is a ROS and a precursor to the highly reactive [•]OH [58]. As SOD activity forms H₂O₂, it seems cells favor H₂O₂ production over the presence of O₂⁻. Several molecular attributions explain this phenomenon; first, for every two O₂⁻ molecules removed by SODs one molecule of H₂O₂ is produced, which effectively reduces the concentration of ROS within a cell. Second, H₂O₂ is capable of crossing membranes while O₂⁻ is not [59]. For mitochondria, this is important because the inner mitochondrial membrane traps O₂⁻ within the organelle while H₂O₂ can diffuse out. Third, H₂O₂ is poorly reactive against biological molecules [58]. Its harmful effects come from reacting with Fe²⁺ to produce [•]OH, meaning the cytotoxicity of H₂O₂ is dependent on free iron concentrations [60]. Finally, multiple enzyme systems within cells eliminate H₂O₂, including catalases, peroxidases, and thioredoxin interacting proteins [61]. Cells tolerate the production of H₂O₂ by SODs as a trade-off for eliminating O₂⁻.

1.6 Catalytic Properties of Human Superoxide Dismutases

A crucial component of the antioxidant power of SODs is their enzyme kinetics. SODs have one of the fastest and most efficient rates of all enzymes. MnSOD is “diffusion-limited” (k_{cat}/K_m near $10^9 \text{ M}^{-1} \text{ s}^{-1}$), meaning the enzyme is so efficient that the rate-limiting steps for enzymatic activity are the diffusion of substrate and products into and out of the active site, respectively [62]. Catalysis by IC-CuZnSOD surpasses rates that are diffusion limited (k_{cat}/K_m of 2

$\times 10^9 \text{ M}^{-1} \text{ s}^{-1}$) by being inherently catalytically efficient and using charged electrostatic potentials on the enzyme surface to guide substrate to the active site and products out [63,64]. MnSOD also enhances diffusion with its electrostatic surface. However, unlike IC-CuZnSOD, MnSOD is product-inhibited by peroxide and thus does not have the catalytic efficiency of IC-CuZnSOD [65]. The high catalytic efficiency of SODs is paramount in maintaining mitochondrial and cell vitality.

In addition to electrostatic diffusion, a second integral component for the high catalytic efficiency of SODs is a rapid proton transfer relay [63,64]. The electron transfers performed by SODs and other oxidoreductases are almost always in tandem with a proton transfer, called CPET [66]. Since the active site metal shuffles between oxidation states (e.g., Mn^{3+} and Mn^{2+} for MnSOD; Cu^{2+} and Cu^{+} for CuZnSOD), the consequent changes in charge by the metal ion are counter balanced via H^{+} transfers to allow the active site to retain the net charge needed for electron transfers to occur. This coupling of a proton and electron transfer permits a thermodynamically favorable redox reaction that avoids ionized intermediates and is extremely efficient, being integral to the highest catalytic rates among enzymes [67-69].

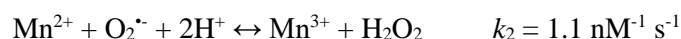
Given the high catalytic speed and efficiency of SODs, a systematic relay of proton transfers along ionizable amino acids is thought to deliver protons to molecules that are coordinated to the active site metal [63,64]. While the exact path of the relay has yet to be determined, mutagenesis studies of the active site perturb catalysis significantly [10,63,70-73]. From these studies, it is difficult to determine which amino acids are responsible for the transfer of protons because they can fulfill more than one role for catalysis, such as stabilizing hydrogen bonds for substrate or maintenance of electrostatic charge. Nonetheless, a proton shuttling network contributes to the catalytic efficiency of SODs.

1.7 Kinetic Properties of Human Manganese Superoxide Dismutase

Support for the presence of a protonation system is given by a simple comparison between the kinetics of $\text{O}_2^{\cdot -}$ disproportionation (i.e. a reaction yielding an oxidized and a reduced product)

without and with enzyme. Without enzyme, two molecules of $O_2^{\bullet-}$ are capable of reacting with each other in bulk solvent to form O_2 and H_2O_2 at a k_{cat}/K_M of $10^5 M^{-1} s^{-1}$. For the enzyme-free reaction, the protons are acquired from the water molecules and consequently lead to the pH and pK_a values dictating protonation kinetics. Due to the difference between the mitochondrial pH of 7.8 and the pK_a of 4.8 for $O_2^{\bullet-}$, the rate-limiting step for enzyme-free disproportionation is protonation of $O_2^{\bullet-}$ from solvent. [74]. For the enzyme-mediated reaction, the k_{cat}/K_M is $10^9 M^{-1} s^{-1}$ and the rate-limiting step is diffusion of substrate and product into and out of the active site [62]. This indicates that protonation is not the rate-limiting step in the enzyme-mediated reaction and the protons are primed for transfer prior to substrate entering the active site. Each redox reaction of MnSOD can be separated by their individual kinetic rates (Scheme 3) [63]. Since the rate-limiting

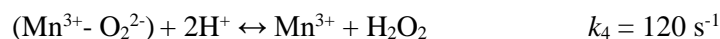
Scheme 3:



step of the reactions is the diffusion of substrate into the active site, it is thought that the electron transfer is the component of the CPET reaction that is introduced by the $O_2^{\bullet-}$ substrate while the proton transfer component is always available. Through inference of these kinetic properties, the notion that protonation rates are substantially enhanced by MnSOD is presented.

A unique characteristic of MnSOD that differentiates from other SOD isoforms is product-inhibition. At steady-state levels (substrate concentration is an order of magnitude greater than the

Scheme 4:



enzyme concentration to yield a saturated zero-order reaction), this inhibition pathway is accessed 50% of the time from Mn^{2+} and $O_2^{\bullet-}$ through the reaction of k_3 to yield an inhibited-complex that slowly releases H_2O_2 through k_4 (Scheme 4) [65,72]. Interestingly, protonation is the rate-limiting

step for k_4 . Since the interaction of Mn^{2+} and $\text{O}_2^{\bullet-}$ can either occur through k_2 or k_3 , the prevalence of each reaction is determined by the ratio of their kinetic rates. It should be noted that the kinetic appearance of k_3 is only seen when $[\text{O}_2^{\bullet-}] \gg [\text{MnSOD}]$. Otherwise, catalysis of MnSOD proceeds first-order through k_1 and k_2 where reaction rate doubles as $[\text{O}_2^{\bullet-}]$ doubles.

1.8 Production Inhibition

MnSOD product-inhibition is thought to prevent the formation of overwhelming amounts of H_2O_2 at once and allowing the systems that clear H_2O_2 , such as catalases and peroxidases, to ‘catch up’ [65,72]. This “self-regulation” performed by k_3 and k_4 (Scheme 4) is thought to use an array of proton transfers that are different from the canonical reactions, k_1 and k_2 (Scheme 3) as inferred from the kinetic rates. The inhibited complex has been suggested to be composed of a Mn-peroxo interaction ($\text{Mn}^{3+} - \text{O}_2^{2-}$) from spectroscopic studies of bacterial MnSODs. In general, the literature of MnSOD accepts this interaction as the identity of the complex though it has yet to be verified due to experimental limitations [64]. The inability in resolving the identity of the complex arises from the technical difficulty in resolving the protonation state of the molecules bound to the Mn without perturbing the redox state of the active site metal [75]. Since electronic states and protonation states are integral to a CPET mechanism, any the exact identity of the inhibited complex is needed to correctly discern a mechanism.

1.9 Dysfunction of Human Manganese Superoxide Dismutase

Given the need for adequate function of MnSOD for cellular life, dysfunction of its catalysis increases the susceptibility of an individual to mitochondrial degeneration and related pathologies [76]. The most prominent causes of dysfunction are polymorphisms (i.e., mutations) and aberrant regulation of post-translation modifications. Three polymorphic mutants and dysregulated acetylation, which neutralizes charged lysine residues that leads $\text{O}_2^{\bullet-}$ to the active site, are responsible for inadequate clearance of oxidative stress in mitochondrial degeneration.

Polymorphisms that affect MnSOD activity appear to cause late-onset diseases through various mechanisms. Some individuals with PD symptoms have an Ala16 to Val mutation in MnSOD [77], yet the same mutation has been reported in healthy individuals of Asian descent indicating that the genetic background for polymorphisms must be considered [78]. Residue Ala16 is in the mitochondrial signaling sequence, and this mutation impairs translocation of MnSOD to the mitochondria. MnSOD is a nuclear-encoded gene that is translated with a 24-amino acid N-terminal signaling sequence that mediates translocation across the mitochondrial membranes to the matrix. After translocation, the signaling peptide is cleaved off. Individuals with the Ala16Val variant have 40% lower MnSOD activity. While this mutation does not directly affect catalysis, it is a marker for several cancers [78], and it demonstrates the importance of localization of MnSOD within the mitochondria to prevent degeneration. Individuals with PD and breast cancer can also have an Ile58 to Thr polymorphism [78]. The Ile58 to Thr polymorphic variant causes two packing defects in each of the two four-helix bundles of the tetrameric interface. These cavities in the interface substantially decrease the stability of the enzyme, cause the tetramer to dissociate into dimers, and causes the enzyme to heat-inactivate at normal body temperatures with a resultant decrease in cells by one-third [79,80]. Also, a Leu60 to Phe variant found on the opposite side of the α -helix from Ile58 is prevalent among those with T-cell leukemia [81]. It appears that MnSOD polymorphic variants with translocation defects, decreased stability, and resultantly decreased activity appear to cause pathologies involving mitochondrial dysfunction.

Post-translational modifications regulate the activity of MnSOD probably by altering its electrostatic surface [82]. Acetylation of lysine residues neutralizes positive charges and alters the net electrostatic vectors that draw negatively charged $O_2^{\cdot-}$ to the active site. For example, conserved residues, Lys29, Lys65, and Lys98 are not in the active site, but their acetylation has a substantial negative effect on the activity of MnSOD which highlights the influence of long-range electrostatic effects on $O_2^{\cdot-}$ diffusion. The enzyme responsible for deacetylating MnSOD and

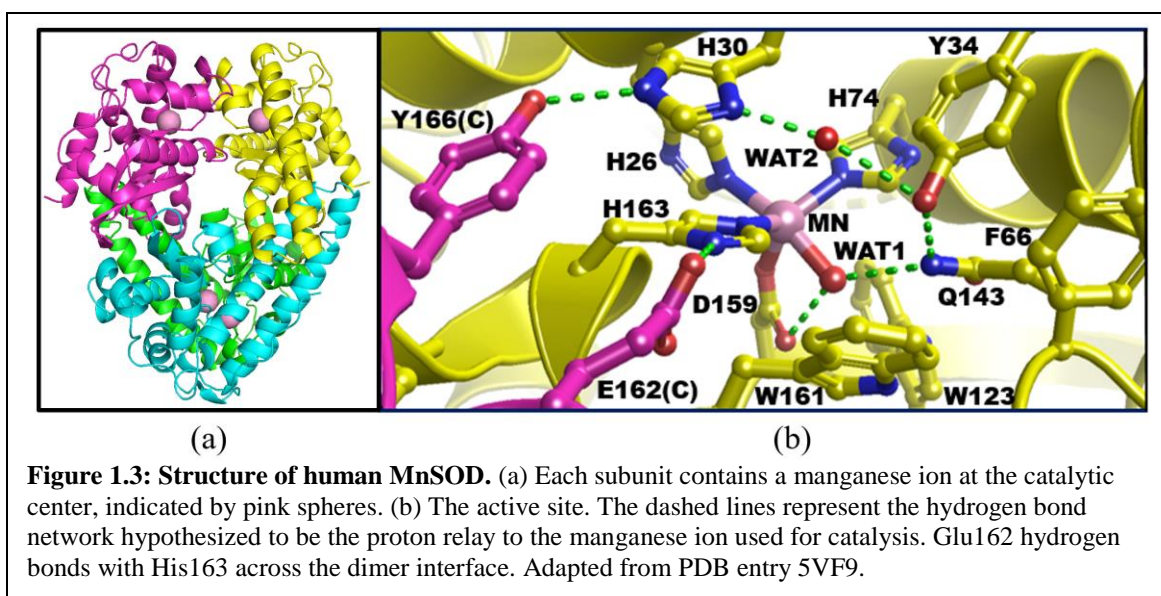
promoting its activity is Sirtuin 3 (SIRT3). SIRT3 is mostly localized to the mitochondria and has been shown to interact with MnSOD directly [83]. Mitochondrial-related pathologies show decreased SIRT3 levels and prominent examples are neurodegenerative diseases such as Alzheimer's disease, Parkinson's disease, amyotrophic lateral sclerosis, and Huntington's disease. In these diseases, SIRT3 mRNA and protein levels are decreased and correlated with hyperacetylation and decreased activity of MnSOD [84]. Consequently, oxidant levels overwhelm the proper function of the mitochondria partially due to a lack of $O_2^{\cdot-}$ clearance.

Another means of hampered MnSOD catalysis is overwhelming amounts of ROS. The conserved Tyr34 residue that is necessary for efficient enzymatic activity is susceptible to nitration by $ONOO^-$ in vitro and in vivo [85]. Nitration of this residue impedes the substrate access funnel which abolishes MnSOD activity completely [48,73]. A characteristic of several cancers is the upregulation of MnSOD with the absence of its activity as a result of $ONOO^-$ mediated inactivation.

1.10 Mechanistic Insights from Previous Structures

Human MnSOD functions as a homotetramer, with each subunit containing an active site surrounding a manganese ion (Figure 1.3a). The metal is coordinated by His26, His74, His163, Asp159, and a single oxygen-containing molecule (denoted WAT1), thought to be either H_2O or OH^- (Figure 1.3b) [82]. These amino acids and ligands, termed the “inner sphere” residues, form a direct interaction with the manganese. The next layer of contacting amino acids, called the “outer sphere” residues, are essential for efficient dismutation. These are His30, Tyr34, Phe77, Trp78, Trp123, Gln143, Trp161, and from across the dimer interface, Glu162 and Tyr166 [65,70,73,86-89]. Each of these residues play a role in catalysis.

A combination of mutagenesis, structural inference, and kinetic analysis suggest particular functions for the active site residues. Substrate is thought to diffuse into the active site through



residues His30 and Tyr34 where it binds to the manganese ion in the position opposite Asp159 [82]. The ~ 5 Å gap between His30 and Tyr34 is the only solvent-accessible area that allows entry into the active site (occupied by an oxygen molecule, denoted WAT2 in Figure 1.3b). Residues of the outer sphere, Phe77, Trp78, Trp123, and Trp161, form a hydrophobic cage around the base of the active site to promote substrate interaction with the manganese ion [65]. Glu162 and Tyr166 from the adjacent subunit hydrogen bonds with His163 and His30, respectively, to stabilize oligomerization [89]. Tyr34, Tyr166, His30, Gln143, and two single-oxygen containing molecules (denoted WAT1 and WAT2) form a hydrogen-bond network that is thought to serve as a proton relay to the manganese ion for proton-assisted electron transfer (dashed lines, Figure 1.3b) [73,86-88,90]. Investigations into the catalytic mechanism have been unable to determine the path of proton transfers owing to limitations in hydrogen detection.

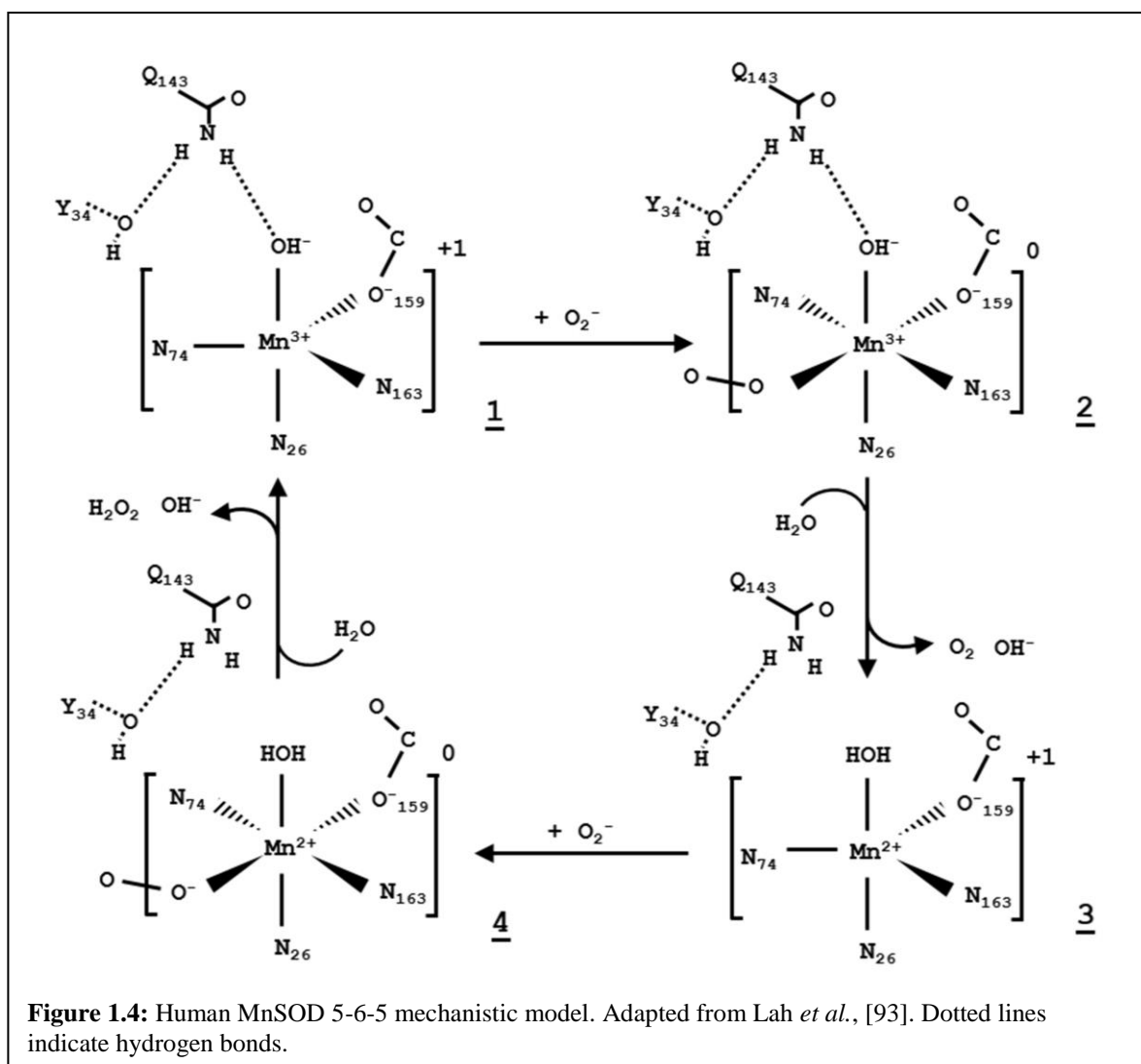
MnSOD has one of the fastest and most efficient reaction rates of all enzymes, with a k_{cat} of $40,000\text{ s}^{-1}$ and a k_{cat}/K_M of close to $10^9\text{ M}^{-1}\text{ s}^{-1}$ [91]. Given that $\text{O}_2^{\cdot-}$ is a negatively-charged substrate, MnSOD probably achieves rapid catalysis with the aid of electrostatic guidance. In 1983, Getzoff and colleagues were the first to calculate electrostatic field vectors for a SOD. For bovine Cu/ZnSOD, they found that $\text{O}_2^{\cdot-}$ guidance to the active site is a long-range process [92], which means that neutralization of a charged amino acid far from the active site, such as acetylation of a lysine, would perturb the net field vectors and hamper guidance of the substrate to the active site [82]. Prior to the work of this thesis, electrostatic analysis has not been performed for human MnSOD.

How $\text{O}_2^{\cdot-}$ interacts with the catalytic site has been difficult to investigate owing to the short half-life and high reactivity of $\text{O}_2^{\cdot-}$ in solution. Crystallographic and spectroscopic studies have instead used azide (N_3^-) as a substrate analog to study $\text{O}_2^{\cdot-}$ binding [93-95]. The azide anion is a potent competitive inhibitor of SODs and binds directly to the active site metal [96,97]. Of note, azide and $\text{O}_2^{\cdot-}$ are different enough in size that their binding to the active site can differ.

Regardless, two $O_2^{\cdot-}$ binding mechanisms have been suggested based on studies with azide, the 5-6-5 and associative-displacement mechanisms.

Lah and colleagues outlined a binding mechanism based on an azide-bound *Thermus thermophilus* MnSOD crystal structure (PDB entry 1MNG) where the azide molecule binds to a sixth coordinate position opposite to the metal-bound aspartate. They propose that the resting state of the MnSOD active site is five-coordinate distorted trigonal bipyramidal and shifts to six-coordinate octahedral upon $O_2^{\cdot-}$ binding (Figure 1.4) [93]. Widening of the angle of two adjacent histidine-ligands (His74 and His163 in Figure 1.4) accommodates binding opposite of the aspartate metal-ligand. A *Caenorhabditis elegans* crystal structure with azide bound also support this mode of binding (PDB entry 5AG2) [98]. A 100 K *Escherichia coli* MnSOD crystal structure at alkaline pH (8.5), in which the enzyme is inactive, shows a hydroxide anion at the sixth-coordinate position (PDB entry 1D5N) [99]. This further suggests that this position is the location of $O_2^{\cdot-}$ binding at the active site. However, so far no one has structurally captured the location of the highly reactive $O_2^{\cdot-}$ anion in the active site. The 5-6-5 mechanism describes the active site manganese dynamically changing its coordination during dismutation.

Whittaker and Whittaker proposed the associative displacement mechanism from their thermochromism (temperature-dependent optical spectra) studies of *E. coli* MnSOD with azide [100,101]. The associative displacement mechanism is an alternative mode of $O_2^{\cdot-}$ binding, defined by a five-coordinate manganese ion in both the resting and substrate-bound forms. Their findings suggest that active *E. coli* MnSOD remains five-coordinate trigonal bipyramidal at physiological temperature (295 K). Upon substrate binding, an unknown manganese ligand displaces, with protonated aspartate or the solvent molecule being the most likely candidates. At low-temperatures (275 – 280 K), the coordination becomes six. These spectroscopic observations are in conflict with the six-coordinate azide-MnSOD structure from *T. thermophilus* (PDB 1MNG), where the crystallization and data collection was at room temperature [93]. Since *T. thermophilus* thrives in



relatively high temperatures (320 – 350 K), room temperature may be a ‘cold’ temperature for the thermophilic species. Whittaker and Whittaker do note that the six-coordinate complex is only marginally unstable at 295 K and suggest it could act as a kinetic intermediate. Thus, the mechanism of superoxide dismutases studied with optical spectra suggest a differing mode of $O_2^{\cdot-}$ substrate binding.

Density function theory (DFT) calculations performed by Jackson and co-workers with *E. coli* MnSOD indicate that the active site with azide adducts exists in a dynamic equilibrium between five and six coordinate states at 296 K. At 273 K, the coordination shifts to predominately six [102]. However, the active site states of either coordination were not supportive of displacement of metal bound ligands, indicating that these calculations were not supportive of the associative displacement mechanism. Instead, the authors propose that the $O_2^{\cdot-}$ substrate may convert to products without coordination to the metal to remain five-coordinate, likely through hydrogen-bond interactions with Tyr34. In NMR studies of *E. coli* FeSOD by the Miller group, azide did not bind to the reduced form of the active site metal, but instead was near Tyr34. These studies could indicate that direct binding of $O_2^{\cdot-}$ to the active site metal for catalysis does not occur for at least some portions of the enzymatic mechanism [103].

1.11 Models of Enzymatic Proton Shuttling for Concerted Proton-Electron Transfer

As alluded by its $10^4 \text{ M}^{-1} \text{ s}^{-1}$ enhancement of protonation efficiency, MnSOD must have a systematic array of protonations for proton-assisted electron transfer. Extensive investigations through both experimental and theoretical approaches studied the proton-based mechanism and yielded several conflicting catalytic models [63,69,71,72,90,93,99,101,102,104-108]. The lack of consensus from the multitude of interdisciplinary approaches is a consequence of the experimental limitations of directly detecting protons.

To date, insight into the proton-based mechanism has come from indirect observations. X-ray diffraction does not detect the hydrogen atom well, but analysis of X-ray crystal structures

reveal a hydrogen bond network at the active site, consisting of Tyr166-His30-WAT2-Tyr34-Gln143-WAT1 (hereafter referred to as the superoxide-independent network, human MnSOD numbering, Figure 1.3b). This configuration is conserved in all Mn and FeSODs [109] and is thought to be involved in a proton relay for proton-assisted electron transfer at the active site metal [63,65,71,73,86,87,89,110]. Mutation of Tyr166, His30, Tyr34, or Gln143 disturb catalysis drastically, indicating the importance of these residues in enzymatic function [63].

Theoretical studies of the proton-shuttling mechanism have been performed through quantum mechanical molecular mechanics (QM/MM) and DFT [90,102,104,106,111,112]. Such approaches attempt to address the underlying complexity of how pK_a s of amino acids and solvent are influenced at the active site to allow systematic proton transfers [113]. The positively-charged manganese at the active site lowers the pK_a s of amino acids and solvent allowing easier deprotonation. Conversely, positively charged ionization would be unfavorable and increase the pK_a s of molecules with such capacity. The extent of influence that manganese has on the pK_a s of molecules at the active site is dynamically changing through shuffling of its redox state. pK_a s are further determined by whether ionization would make a non-covalent interaction more favorable. Together, the net changes in ionization (i.e. proton transfers) at the active site must be energetically downhill and be able to regenerate through cycling of the redox state of the manganese cation.

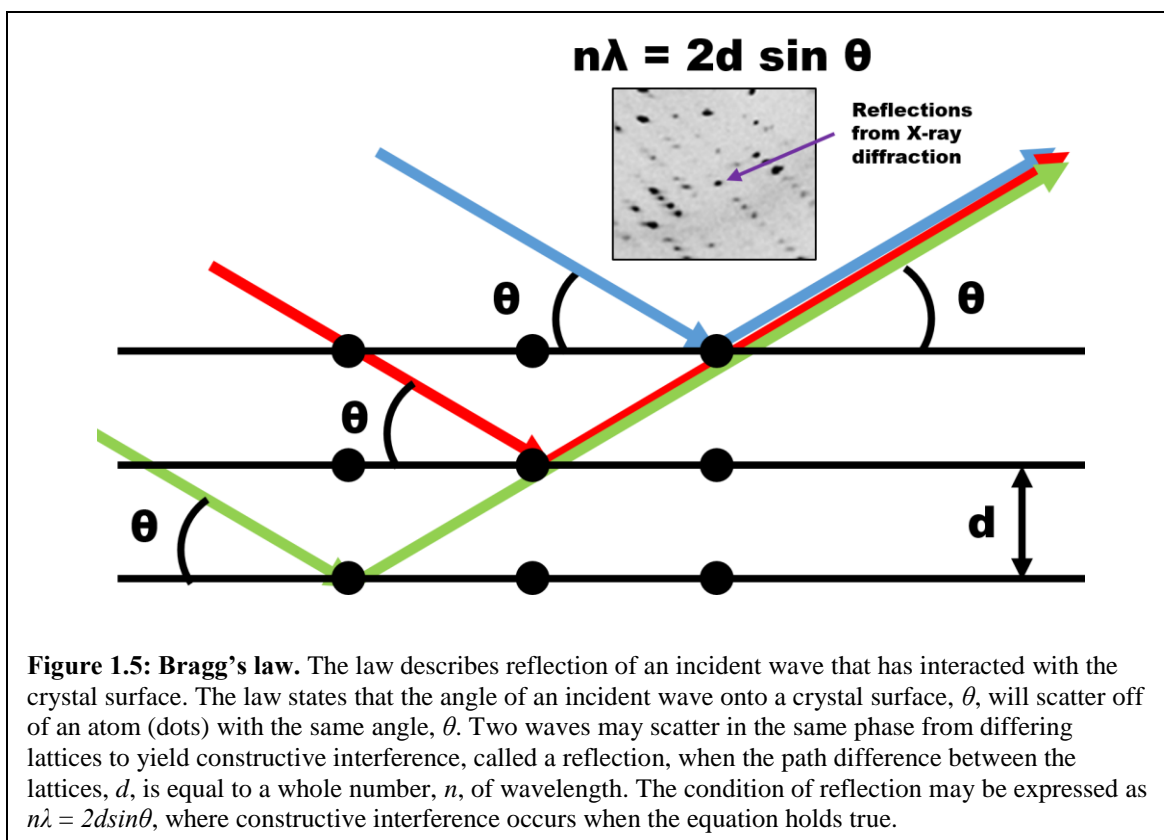
Investigations through QM/MM and DFT calculations have studied WAT1, the metal-bound solvent molecule. This molecule is probably a redox-linked proton acceptor and perhaps the most studied component of the network [69,104,114]. Our current understanding is that in the Mn^{3+} state, the solvent ligand is in the deprotonated hydroxide form (OH^-), with its ionization stabilized by the electrostatic interaction with Mn^{3+} . Upon conversion to the Mn^{2+} state, the solvent ligand is protonated to become H_2O that counterbalances the changes in the metal charge (Figure 1.4). The second half reaction regenerates the $Mn^{3+}-OH^-$ state. The proton from the solvent ligand is thought to be involved in reducing superoxide to hydroperoxyl ion (HO_2^-), which accounts for one of the

two protons for conversion into H_2O_2 . The source of the second proton to convert HO_2^- to H_2O_2 is more poorly understood and is hypothesized to come from His30, WAT2, Tyr34, or bulk solvent as evidence for any alternatives, theoretical or experimental, are not present [93,115]. Protonation and deprotonation of the solvent ligand likely happens when a superoxide is bound at the active site (not necessarily directly to the manganese) as this makes product disassociation exergonic and enhances product formation [116]. These theoretical studies attempt to clarify the source of the two protons during the enzymatic reaction of MnSOD.

1.12 Protein Crystallography

The means in which a protein functions is directly dependent on its three-dimensional arrangement of atoms. This interdependent structure-function relationship has popularized the biophysical technique of crystallography. Crystallography elucidates the three-dimensional organization of atoms by diffracting entities that can be described as particles or waves (henceforth referred to as waves) off of a crystallized sample. These waves are typically those of X-rays (photons) but may also be neutrons or electrons. The interaction between a primary beam of waves and a crystalline sample results in scattering of the waves into a diffraction pattern that may be used to construct the electron density of the individual crystallographic unit.

The advantage of using a crystallized protein sample over a solution sample arises from the ordered and predictable nature of crystals. A crystal is composed of lattices of protein units that are fixed in place in contrast to the spontaneous dispersion of protein in solution. The interaction of an incident beam and a crystal lattice leads to the phenomenon of Bragg diffraction, a manifestation of Bragg's law (Figure 1.5) [117]. Bragg diffraction yields reflections, instances of constructive interference from the scattering of waves off of a plane of atoms. Reflections only occur when the scattered waves are in the same phase, represented as the equation $n\lambda = 2d\sin\theta$ for two atoms, where n is a whole integer, λ is wavelength, d is the distance between lattices of atoms, and θ is



incident and scattering angle (Figure 1.5). The distinctive symmetry elements of crystals, called space groups, cause reflections to be arranged into predictable patterns that are representative of the ordering of the protein lattice. Bragg diffraction is one of the major principles behind the science of crystallography.

The reflections produced by a diffraction experiment must be deconvoluted to yield information on the atomic arrangement of the crystal. Utilization of the reciprocal space system is one of the first steps to deconvolution. Reciprocal space is used to describe planes of atoms of a crystal lattice. The system is useful in defining reflections that are a product of constructive interference from planes of atoms. The reflections are characterized by the Miller indices (hkl) that describe a family of planes through the crystal. By a process known as indexing, individual reflections are associated with a particular (hkl). Indexing utilizes the geometric patterns of the reflections to give insight into the symmetry of the crystal and therefore the arrangement of the planes. The mathematical system of reciprocal space directly ties the reflections from a diffraction experiment to physical features of a crystal.

While indexing correlates reflections with lattice planes, the experimental data of a crystallography experiment lies in the intensity of the reflections. The process of integration assigns intensity values (I) to reflections along with a background value (σI). Since reflections may span over many diffraction images in order to capture data from differing crystal orientations, the data measured by integration are often scaled to take into account any perturbations (e.g. radiation damage) during data collection. The intensities hold incomplete information on the structure factors (F_{hkl}) that describe the contribution of diffraction from the contents of the unit cell. Structure factors are the principle reciprocal space quantities used to form the real space electron/nuclear density (ρ_{xyz}) maps representative of the atomic structure of the unit cell.

Structure factors are the scattered waves from the lattice planes and are composed of two key parts, amplitudes ($F_{hkl}[A]$) and phases (ϕ_{hkl}). In essence, structure factors are constituent sin

waves with differing frequencies that in summation approximate the distribution of density. This describes a Fourier transform (FT), a mathematical transform that deconstructs a function (i.e. density) into component sin wave frequencies (i.e. structure factors). Thus, the FT is the means to convert from terms of real space (xyz) to that of reciprocal space (hkl).

$$\rho_{xyz} \xrightarrow{FT} F_{hkl}$$

Likewise, the goal of a crystallographic experiment is to utilize the diffraction data for the inverse Fourier transform (FT⁻¹).

$$F_{hkl} \xrightarrow{FT^{-1}} \rho_{xyz}$$

However, this transform requires both the amplitude and phase components of the structure factors. A diffraction experiment only yields the amplitudes, where the intensity of the reflections are proportional to the amplitudes of the structure factors by $I \propto F_{hkl}[A]^2$. The phase components of the structure factors are lost and need to be introduced through other methods.

Techniques to obtain phase information include isomorphous replacement, anomalous dispersion, and molecular replacement. For isomorphous replacement, a crystal sample is soaked or co-crystallized with a heavy atom. In principle, the structure factors from the heavy atom containing sample (F_{ph}) are the sum of the structure factors of the heavy atom on its own (F_p) and the native crystal (F_h), inclusive of amplitude and phase components.

$$F_{ph} = F_p + F_h$$

With the known contribution of the heavy atom, the phase of the structure factors from the native crystal can be solved. Anomalous scattering is a phasing technique that also utilizes a heavy-atom derivative. By using an incident X-ray beam with a wavelength approaching the absorption edge of the heavy atom, anomalous dispersion occurs and imparts a phase shift and magnitude change on scattering factor. Since the scattering factor of an atom is proportional to its structure factor, differences between the structure factors from anomalous scattering and non-anomalous scattering are used to obtain phasing information. In molecular replacement, phasing information is derived from a similar structure that was previously solved. From any 3D structure, a density may be

calculated which can be deconstructed into its structure factors inclusive of amplitude and phase components. Thus, the experimental amplitudes from a diffraction experiment are combined with calculated phases of a known structure to give a ‘starting’ density map. In summation, phasing information must be applied to the experimentally obtained diffraction data to yield real space density and can be provided through multiple methods.

After both the amplitude and phase components of the structure factors are known, an initial real space density map can be constructed. Using 3D graphics software, atoms may be placed in positions of density with the goal of creating a protein model representative of the density. Model building coincides with iterations of refinement, a computational process that statistically adjusts the atoms of the model to better fit the experimental data. This includes parameters for the model that ensure chemical reasonability, such as optimal bonds distances and angles. Refinement is the last but one of the most critical processes for solving a crystal structure.

A summary of the methods that lead to a protein model from diffraction of a crystal is as follows (Figure 1.6). The interaction of an incident beam with an ordered protein lattice yields reflections. These are a result of scattered waves constructively interfering according to Bragg’s law. The intensity of the reflections are the square of the structure factor amplitudes as reasoned from the physics corollary $I = A^2$. Reflections of a sole diffraction experiment do not contain structure factor phase information and are obtained through other means, such as isomorphous replacement, anomalous dispersion, or molecular replacement. The amplitudes and phases of the structure factors are utilized to build an initial real space density map that ultimately provides the information needed to construct a protein model. Model building is performed with the goal of creating a structure that is representative of the density. This is done with iterations of refinement that systematically adjust the protein model to better fit the diffraction data while ensuring chemical reasonableness. Altogether, solving a crystal structure includes the involvement of biochemistry, physics, and computer science.

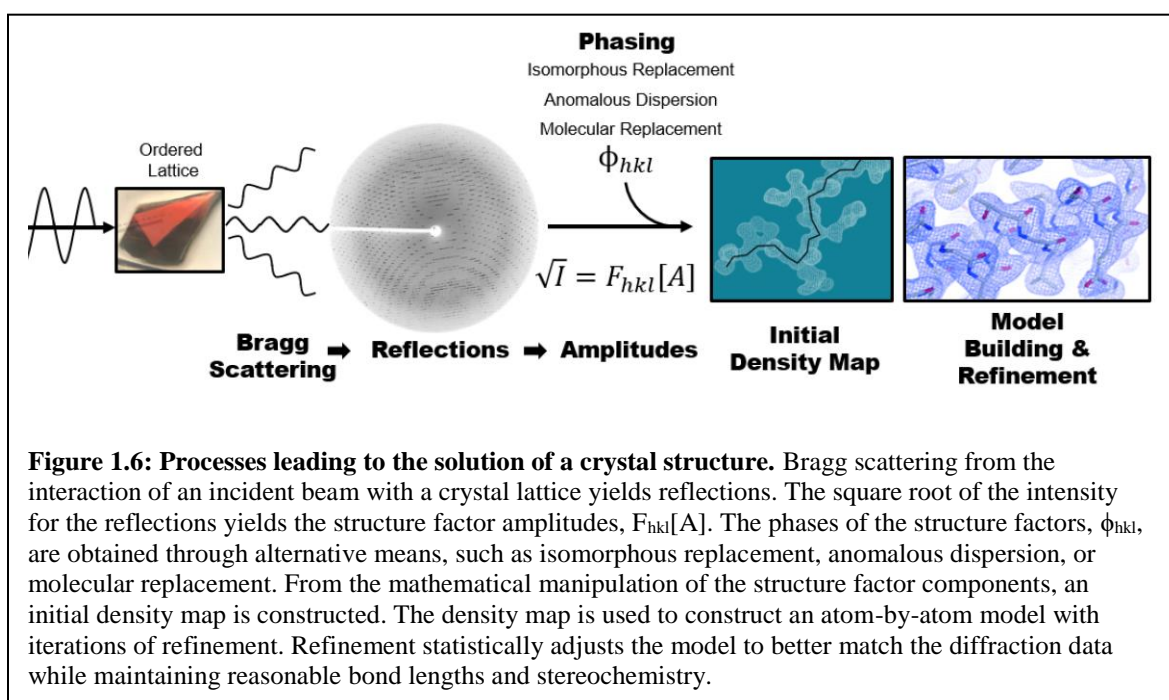


Figure 1.6: Processes leading to the solution of a crystal structure. Bragg scattering from the interaction of an incident beam with a crystal lattice yields reflections. The square root of the intensity for the reflections yields the structure factor amplitudes, $F_{hkl}[A]$. The phases of the structure factors, ϕ_{hkl} , are obtained through alternative means, such as isomorphous replacement, anomalous dispersion, or molecular replacement. From the mathematical manipulation of the structure factor components, an initial density map is constructed. The density map is used to construct an atom-by-atom model with iterations of refinement. Refinement statistically adjusts the model to better match the diffraction data while maintaining reasonable bond lengths and stereochemistry.

1.13 X-ray and Neutron Diffraction for MnSOD

The type of beam utilized for the diffraction of protein crystals has significant effects for structural analysis. Most biological structure-based knowledge is derived from X-ray diffraction of protein crystals due to the high flux and accessibility of X-rays. Small crystals that are less than 0.05 mm^3 are capable of producing a high-resolution data set due to the energies of X-ray sources that are often found at local universities. Neutron diffraction provides different but significant structural information but requires large crystals, $\sim 1.0 \text{ mm}^3$, to compensate for the lower fluxes of neutron sources. These sources are found only at large scientific institutions such as that of Oak Ridge National Laboratory due to the significant investment needed to produce neutrons. The lesser accessibility of neutron sources means users should have significant incentive to use them over X-rays. The incentive is the difference of scattering properties between the two particles.

X-rays and neutrons interact with C, N, O, and H atoms of a protein differently. X-ray scattering is the result of the interaction between a high-energy photon (i.e. an X-ray) with the electron cloud of an atom [118]. The more electrons an atom has, the greater the magnitude of scattering from X-rays. This leads to a periodic trend where X-ray scattering increases as a function of atomic number. Since C, N, and O have a similar number of electrons, they have similar scattering power (Figure 1.7a). The H atom scatters to a much lesser extent compared with the other atoms and is typically not discernible in electron density maps unless diffraction surpasses 1.0 \AA resolution. For this reason, the majority of X-ray crystal structures are modelled without H atoms.

Instead of interacting with an atom's electron clouds for scattering, neutrons scatter due to an interaction with an atom's nucleus. For this reason, the magnitude of neutron scattering for an atom depends on the contents and spin of the nucleus [119]. Atoms with neighboring atomic numbers are capable of much different scattering properties (Figure 1.7a). Likewise, isotopes of the same atom may scatter much differently due to the differences of the atomic nucleus.

For crystallography, neutron scattering is of significant value for those wishing to discern H atoms positions (Figure 1.7b-c). Scattering of H is on par with that of C, N, and O, making its discernibility in density maps feasible. However, H scattering by neutrons causes significant incoherent scattering and replacement of H in a crystal with D is preferred. D has approximately twice the absolute magnitude of coherent scattering compared to H while having 40 times less incoherent scattering. In a process called perdeuteration, recombinant expression systems specialized for fully deuterated media are prepared for the purpose of yielding protein with H replaced with D [120]. Neutron diffraction is able to discern the positions of H with much lesser difficulty compared to X-ray diffraction.

Many biological substrates and macromolecules rely on proton transfers (H^+) to facilitate their function. Of particular note are oxidoreductases, enzymes that perform electrons transfers through a CPET mechanism, where electron transfers and proton transfers are energetically coupled. Oxidoreductase mechanisms are difficult to study with X-rays due to the low scattering interaction with H and the propensity for X-rays to reduce metals during diffraction [75]. Instead, neutron diffraction is a much more feasible means to study oxidoreductase mechanisms due to the scattering of H/D being on par with C/N/O while being inert to metal electronic states. In regards to the present work, MnSOD is an oxidoreductase that relies on proton transfers to facilitate its CPET mechanism. Prior to the work of this dissertation, the enzymatic CPET mechanism of MnSOD has been unclear and filled with puzzling observations since its discovery approximately half a century ago.

To exemplify the perplexing nature of the mechanism, consider residue Tyr34, the most studied residue for MnSODs. It is the closest titratable residue to the Mn and previous studies speculate it donates a proton for CPET. Tyr34 mutation to Phe though yields peculiar results (Table 1.1). The redox potential of the enzyme is nearly unchanged compared to wildtype [105], the catalytic efficiency is unaffected [91], k_1 ($Mn^{3+} \rightarrow Mn^{2+}$) is unchanged, and the active site structure

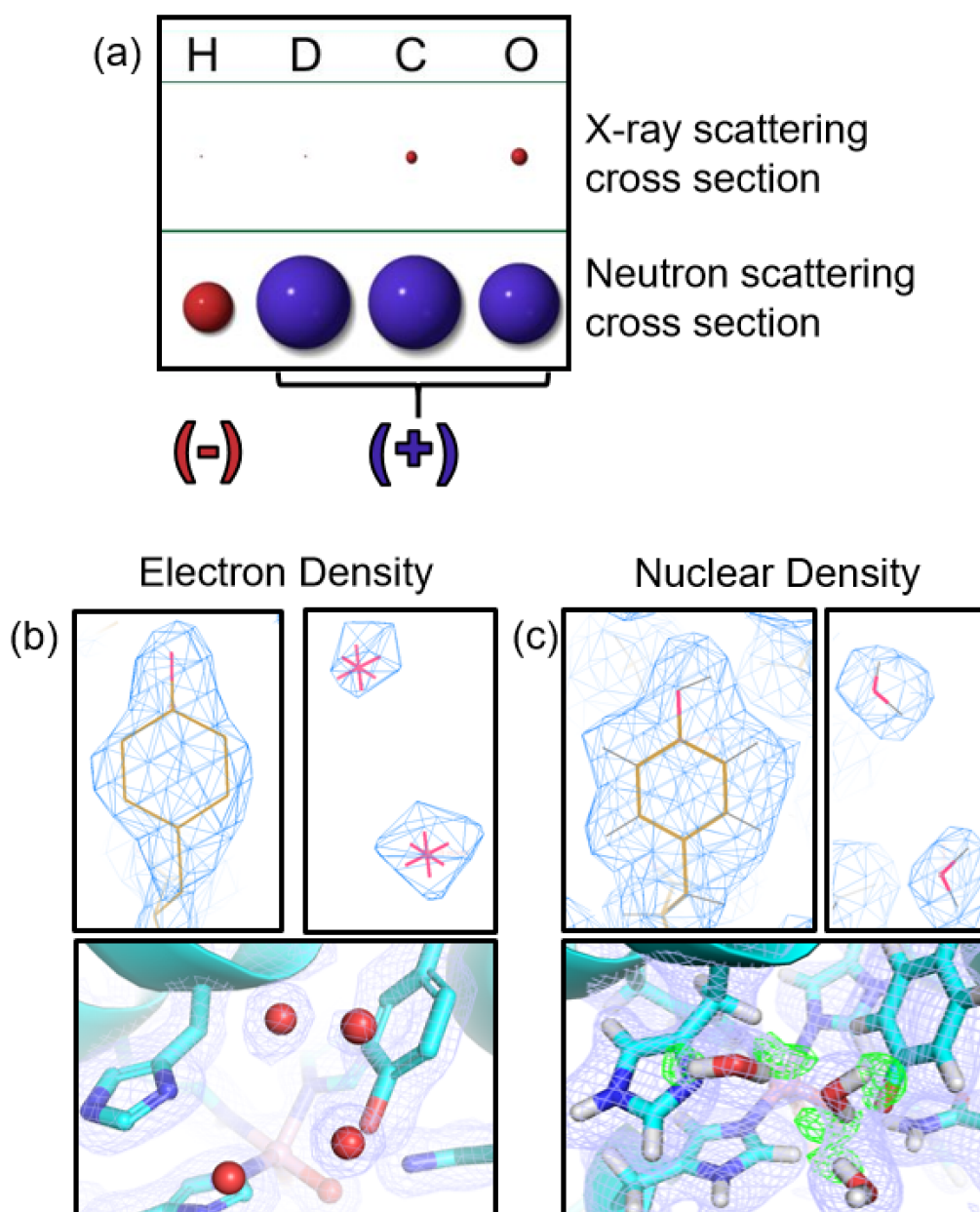


Figure 1.7: X-ray versus neutron diffraction. (a) The strength of X-ray scattering is dependent on the number of electrons the atom scatterer contains. C and O have 6 and 8 electrons, respectively, and have much greater scattering strength compared to H and D, both with 1 electron. For neutron scattering, the magnitude is related to the properties of an atom's nucleus, such as spin. Isotopes have different scattering interactions due to the differing contents of the nucleus. This causes the four atoms presented to have similar scattering power. Of note, H scatters negatively whereas the other three atoms presented scatter positively. (b-c) Representative images of electron (2.0 Å) and nuclear density (2.3 Å) to highlight differences in information obtained. The nuclear density data were obtained from a fully deuterated crystal.

Table 1.1 Comparison of WT and Y34F MnSOD Attributes

MnSOD		WT	Y34F
k_{cat}/K_M ($M^{-1} s^{-1}$)		10^9	10^9
k_{cat} (ms^{-1})		40	3.3
k_1 ($nM^{-1} s^{-1}$)	$(Mn^{3+} + O_2^{\bullet-} \leftrightarrow Mn^{2+} + O_2)$	1.5	0.55
k_2 ($nM^{-1} s^{-1}$)	$(M^{2+} + O_2^{\bullet-} + 2H^+ \leftrightarrow M^{3+} + H_2O_2)$	1.1	< 0.02
k_3 ($nM^{-1} s^{-1}$)	$Mn^{2+} + O_2^{\bullet-} \leftrightarrow (Mn^{3+} - O_2^{2-})$	1.1	0.46
k_4 ($nM^{-1} s^{-1}$)	$(Mn^{3+} - O_2^{2-}) + 2H^+ \leftrightarrow Mn^{3+} + H_2O_2$	120	52
E_m (eV)		393 ± 29	435 ± 30

is very similar to the wildtype [91]. However, k_2 ($\text{Mn}^{2+} \rightarrow \text{Mn}^{3+}$) is ablated while product-inhibition is significantly increased ($k_3 \gg k_2$) with slow disassociation ($k_4 \downarrow$) [70]. If Tyr34 is indeed a proton donor for catalysis, it would be expected for the redox potential to change and for k_1 ($\text{Mn}^{3+} \rightarrow \text{Mn}^{2+}$) to be ablated the proton donor is absent for CPET. This means proton transfer is still occurring near the Mn without Tyr34, though there are no other titratable solvent accessible residues nearby. Without being able to observe H atom positions, much is to be desired for discerning the mechanism of MnSOD.

Chapter 2: Substrate-analog Binding and Electrostatic Surfaces of Human MnSOD

2.1 Introduction

Two mechanisms for the activity of iron and manganese SODs have been suggested. The first is called the 5-6-5 mechanism and proposes superoxide coordinates to the active site metal and becomes molecular oxygen or hydrogen peroxide in a two-step fashion. Here the coordination state of the active site metal converts from five-coordinate trigonal bipyramidal to six-coordinate octahedral upon substrate binding and back to five-coordinate upon substrate release [93-95]. In this mechanism, anionic substrate-analogs are believed to bind in the same position as superoxide, opposite Asp159. The second mechanism observed with studies of thermochromism is called associative displacement. This mechanism proposes that six-coordinate anionic complexes represent an inactive form of the enzyme that is seen only at low temperatures. A five-coordinate complex represents the active form at physiological temperature, with anion binding displacing one of the manganese ligands, either bound water or Asp159 [101,121]. The azide ion is a potent competitive inhibitor and is frequently assumed to act as a substrate analog to superoxide [97,122]. Published structures of azide in complex with MnSOD have been solved at room temperature for *Thermus thermophilus* (PDB entry **1MNG**) and cryocooled for *Caenorhabditis elegans* (PDB entry **5AG2**) [93,98]. Both show the azide binding end-on to the manganese ion at the sixth coordinate. An unpublished structure of the Y174F MnSOD-azide complex from *Escherichia coli* (PDB entry **1ZLZ**) shows binding in the same manner as well, with the Y174F mutation breaking a hydrogen bond at the dimer interface. To date, the crystal structure of human MnSOD with bound azide has not been solved.

Here, the crystal structures of native human MnSOD and the human MnSOD-azide complex are reported and provide the binding position for azide in the active site. Electrostatic solvent accessible surface calculations were performed with these crystal structures to map the residues that are important for electrostatic guidance of the substrate to the active site. These

surface calculations were conducted with three differing active site states, including one with superoxide coordinated using the azide binding site as a model.

2.2 Materials and Methods

2.2.1 Protein Purification and Crystallization

Full length human MnSOD cDNA optimized for *E. coli* codons was cloned into the pACYCDuet-1 expression vector (Genscript) and transformed into the *sodA⁻sodB⁻* strain of *E. coli*, which lacks endogenous Mn and FeSODs [123]. Cells were grown in Terrific Broth with 0.8% (v/v) glycerol and supplemented with 0.75 g L⁻¹ MnSO₄ to provide the protein's active site manganese ion. Cell strain fidelity was maintained with 30 µg mL⁻¹ kanamycin. Recombinant protein was expressed upon addition of 1 mM isopropyl β-D-1-thiogalactopyranoside. Cells were harvested by centrifugation and stored at -80°C until purification. Cells were re-suspended in 50 mM potassium phosphate (K₂HPO₄/KH₂PO₄), pH 7.8, prior to lysis using an Emulsiflex. Clarified lysate was incubated at 65° C for one hour and precipitated proteins were removed by centrifugation. Soluble protein was dialyzed against 5 mM potassium phosphate, pH 7.8, and applied to pre-swollen diethylaminoethyl (DE52) cellulose resin (GE Healthcare). The protein-resin slurry was rocked for 1 hour at 10° C before vacuum filtration using Whatman #4 filter paper and a Büchner funnel. Resin was washed with an excess of 5 mM potassium phosphate, pH 7.8, then protein was eluted with 100 mM potassium phosphate, pH 7.8. Eluted protein was dialyzed against 2.5 mM 2-(N-morpholino)ethanesulfonic acid (MES), pH 5.5, applied to a carboxymethyl (CM) sepharose (GE Healthcare) column, and eluted with a NaCl gradient. Fractions were concentrated using 5 kDa molecular weight cut-off concentrators (Sartorius) to 21 mg mL⁻¹, as measured by NanoDrop ND-1000 spectrophotometer using an extinction coefficient of 43.43 L/mol⁻¹ cm⁻¹ at 280 nm. Human MnSOD crystals were grown from 1.8 M potassium phosphate, pH 7.8, by hanging-drop vapor diffusion at room temperature. Protein and reservoir solution were mixed at a 1:1 ratio to give a 2.0 µL drop and crystals appeared within 1 day. To obtain the azide

complex, 2.0 μ L of reservoir containing 200 mM sodium azide were added to drops of 6 day crystals. Data was collected 3 h after azide addition.

2.2.2 Data Collection and Structure Determination

Crystals were briefly passed through a cryoprotectant solution consisting of 3.6 M potassium phosphate, pH 7.8, using a microloop (MiTeGen). The MnSOD-azide crystals also had 150 mM sodium azide in the cryoprotectant. Crystals were plunged into a 100 K stream of nitrogen gas provided by a Rigaku X-stream. X-ray diffraction data were collected using a Rigaku FR-E Cu $K\alpha$ rotating-anode generator operating at 45 kV and 45 mA equipped with a R-Axis IV⁺⁺ detector. Data were processed using *HKL-3000* for indexing, integration, and scaling [124]. Native MnSOD and the MnSOD-azide complex were solved using Protein Data Bank coordinates **1JA8** that had the same unit cell dimensions and space group [65]. Following removal of solvent and active-site metals, simple molecular replacement was performed through rigid-body refinement and subsequent restrained-positional refinement using *REFMAC5* to 1.82 Å and 1.77 Å resolution for the native and azide complex structures, respectively [125]. Using *Coot*, omit electron density maps were analyzed and the protein model was fit [126]. New solvent structure and active-site manganese ions with bound azide were modeled into omit electron density maps. Azide occupancy was determined by adjusting until the B values refined reasonably to neighboring atoms. For both native and azide structures Tyr45 of chain B was modelled with dual conformers. Geometries of the final models were verified with *MOLPROBITY* [127].

2.2.3 Electrostatic Surface Calculations

Outside the active site, pKa calculations were performed by *PROPKA 3.1* at pH 7.0 to generate partial charges. Then the partial charges were assigned on a per-atom basis in PQR file format using *PDB2PQR* within the same automated pipeline [128]. For the active site, partial charges from the literature [129] taking into account coordination of the manganese ion were manually applied to the PQR file. These charges also assumed a pH of 7.0. Electrostatic surfaces

were generated with *APBS* using ionic strengths of 0.15 and -0.15 M for the positive and negatively charged species, respectively [130].

2.3 Results and Discussion

X-ray diffraction data from native MnSOD and MnSOD-azide complex crystals were measured at a resolution of 1.82 Å and 1.77 Å, respectively (Table 2.1). Pink, hexagonal bipyramidal crystals formed in the space group $P6_122$ with unit cell dimensions of $a = b = 77.91$, $c = 237.92$ Å (native) and $a = b = 77.90$, $c = 238.44$ Å (azide complex). The crystal structures had two subunits in the asymmetric unit that were designated as chains A and B. Native oligomerization of human MnSOD consists of a tetramer formed from a dimer of dimers by crystallographic symmetry. The tetrameric interface is comprised of a four helix bundle [131].

2.3.1 Azide Binding to Human MnSOD

The azide ion acts as a strong competitive inhibitor for SOD by binding directly to the active site metal [97,122]. A summary of active site bond distances and angles are listed in Table 2.2. Chain A shows an azide molecule binding to the manganese ion at the sixth coordinate position to form a distorted octahedral active site geometry (Figure 2.1a). The azide binds end-on to the metal in the position opposite Asp159 with a bond distance of 2.01 Å and an angle of 124° and widens the $N^{\delta 2}(H74)-Mn-N^{\delta 2}(H163)$ angle 15° compared to the native structure. Azide also interacts with WAT2 of the hydrogen bond network, with a bond distance of 3.37 Å (Figure 2.1b). The active site solvent structure is unchanged compared to the native structure, with a solvent molecule hydrogen bonded to WAT2 (designated WAT3) and another hydrogen bonded to Y34 (designated WAT4). While the hydrogen bond network is postulated to shuttle protons to the active site for superoxide dismutation, the mechanism and protonation state of the molecules in the network are not known. For chain B, the sixth position of the active site is empty and the five-coordinate active site is the trigonal bipyramidal geometry.

Table 2.1 Crystallographic Data and Refinement Statistics for hMnSOD and hMnSOD-azide
Values for the outer resolution shell are given in parentheses.

	hMnSOD	hMnSOD-azide
<i>A. Data collection statistics</i>		
Diffraction source	Rigaku FRE Cu K α rotating-anode	Rigaku FRE Cu K α rotating-anode
Wavelength (Å)	1.5418	1.5418
Temperature (K)	100	100
Detector	R-Axis IV++	R-Axis IV++
Crystal-detector distance (mm)	240	240
Rotation range per image (°)	0.5	0.5
Exposure time per image (s)	300	300
Space group	<i>P</i> 6 ₁ 22	<i>P</i> 6 ₁ 22
No. of molecules in asymmetric unit	2	2
<i>a</i> = <i>b</i> (Å)	78.24	77.90
<i>c</i> (Å)	238.47	238.44
α = β (°)	90	90
γ (°)	120	120
Mosaicity (°)	072	0.78
Resolution range (Å)	67.5-1.82 (1.85-1.82)	67.5-1.77 (1.80-1.77)
Total No. of reflections	231836	229527
No. of unique reflections	38400	40060
Completeness (%)	96.8 (89.6)	96.0 (84.0)
Redundancy	6.0 (4.6)	5.6 (3.6)
$\langle I/\sigma(I) \rangle$	20.6 (3.0)	12.7 (2.0)
R_{meas}^a	0.08 (0.38)	0.16 (0.59)
<i>B. Refinement statistics</i>		
PDB ID	5T32	5T30
Resolution range (Å)	67.76-1.82	67.46-1.77
Completeness (%)	96.5	94
No. of reflections, working set	36515 (2434)	40053 (3139)
No. of reflections, test set	1885 (162)	1964 (148)
Final R_{cryst}	0.201	0.214
Final R_{free}	0.226	0.245
No. of		
Protein non-H atoms	3138	3154
Manganese ions	2	2
Phosphate ions	2	2
Potassium ions	1	2
Azide	0	2 (x 0.4)
Water	305	354
R.m.s. deviations		
Bonds (Å)	0.009	0.011
Angles (°)	1.32	1.38
Mean <i>B</i> factors (Å ²)		
Protein	21	19
Manganese ions	17	15
Phosphate ions	39	37
Potassium ions	23	24
Azide	—	19
Water	26	24

$$^a R_{\text{meas}} = \Sigma_{hkl} \sqrt{\frac{n}{n-1}} \Sigma_{j=1}^n |I_{hkl,j} - \langle I_{hkl} \rangle| / \Sigma_{hkl} \Sigma_j I_{hkl,j}$$

Table 2.2 Active Site Geometry Comparisons of Native and Azide-Bound MnSOD

	hMnSOD		hMnSOD-azide	
	Chain A	Chain B	Chain A	Chain B
Covalent bond (Å)				
Mn-N ^{ε2} (H26)	2.26	2.20	2.27	2.19
Mn-N ^{ε2} (H74)	2.25	2.21	2.27	2.26
Mn-O ^{δ2} (D159)	2.11	2.07	2.04	2.05
Mn-N ^{ε2} (H163)	2.27	2.28	2.21	2.25
Mn-O(WAT1)	2.16	2.15	2.14	2.16
Mn-N3(AZI)	—	—	2.69	—
Hydrogen Bonds (Å)				
N ^{ε2} (Q143)-O(WAT1)	2.99	2.89	3.04	2.99
N ^{ε2} (Q143)-OH(Y34)	2.87	2.87	2.94	2.87
O(WAT2)-OH(Y34)	2.76	2.70	2.73	2.89
O(WAT2)-N ^{δ1} (H30)	2.63	2.69	2.66	2.64
O(WAT2)-N3(AZI)	—	—	2.91	3.69
OH(Y34)-N3(AZI)	—	—	4.04	3.60
Bond angles (°)				
N ^{ε2} (H26)-Mn- N ^{ε2} (H74)	94.34	89.93	94.95	91.96
N ^{ε2} (H26)-Mn-O ^{δ2} (D159)	82.71	81.98	84.09	80.17
N ^{ε2} (H26)-Mn- N ^{ε2} (H163)	93.39	93.36	90.25	92.74
N ^{ε2} (H26)-Mn-O(WAT1)	165.71	169.29	165.91	166.65
N ^{ε2} (H74)-Mn-O ^{δ2} (D159)	105.39	106.94	103.32	104.58
N ^{ε2} (H74)-Mn- N ^{ε2} (H163)	136.44	138.44	140.44	138.16
N ^{ε2} (H74)-Mn-O(WAT1)	92.20	94.02	92.50	93.59
O ^{δ2} (D159)-Mn- N ^{ε2} (H163)	118.10	114.55	116.23	117.19
O ^{δ2} (D159)-Mn-O(WAT1)				
N ^{ε2} (H163)-Mn-O(WAT1)	83.31	87.35	82.56	86.68
N ^{ε2} (H26)-Mn-N3(AZI)	90.58	90.28	91.60	91.21
N ^{ε2} (H74)-Mn-N3(AZI)	—	—	95.24	—
O ^{δ2} (D159)-Mn-N3(AZI)	—	—	72.96	—
N ^{ε2} (H163)-Mn-N3(AZI)	—	—	176.17	—
Mn-N3(AZI)-N2(AZI)	—	—	67.51	—
N1(AZI)-N2(AZI)-N3(AZI)	—	—	105.86	—
	—	—	179.57	—

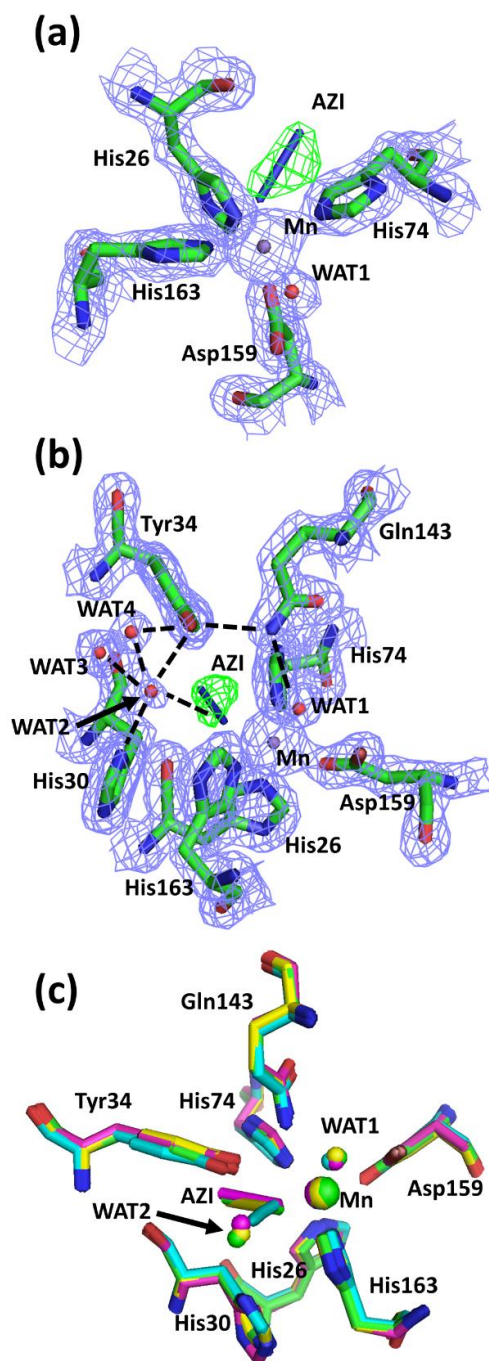


Figure 2.1: Active site geometry and electron density of azide-soaked human MnSOD. (a) Six coordinate octahedral active site geometry at chain A. (b) Azide interaction with the active site manganese at chain A. Maps were calculated before azide was modelled and refined with Fourier coefficients $F_o - F_c$ (green) contoured at 3.0σ , and $2F_o - F_c$ density (blue) contoured at 1.5σ . (c) Active site overlays of MnSOD-azide complexes from *T. thermophilus* (cyan, PDB entry 1MNG), *C. elegans* (yellow, PDB entry 5AG2), *E. coli* (pink, PDB entry 1ZLZ) and human (green, PDB entry 5T30). Overlays were performed using *SUPERPOSE*. Black, dashed lines indicate hydrogen bonds.

The extent of azide binding to the manganese of MnSODs was measured to be no more than 50% by high field electron paramagnetic resonance spectroscopy [132]. This is in good agreement with the estimate of 40% occupancy of azide molecules found in human MnSOD electron density maps of chain A. Also, it compares well with the other published MnSOD-azide complex crystal structures, with 50% occupancy for *T. thermophilus* and 30% occupancy for *C. elegans*. The average azide B factor of 16 Å² illustrates a firm presence of the molecules. Azide molecules were not found elsewhere in the electron density maps.

In the three other MnSOD-azide structures, from *T. thermophilus* (PDB entry **1MNG**), *C. elegans* (PDB entry **5AG2**), and Y174F *E. coli* (PDB entry **1ZLZ**) the azide is bound end-on at the active site manganese with the same coordination but with differing bond distances and angles (Figure 2.1c). The only structure with 100% occupancy for azide is 1ZLZ with the Y174F mutation. The other structures have partial occupancies and this complicates the interpretation of the analysis as the crystal structures represent an average between 5- and 6-coordinate active sites. The prokaryotic structures show a bond distance of 2.2 Å and an angle of 143° from *T. thermophilus* and a bond distance of 1.94 Å and an angle of 123° from *E. coli*. The eukaryotic *C. elegans* structure has a bond distance of 2.8 Å and an angle of 94°. All of the azide structures widen the N⁶²(H74)-Mn- N⁶²(H163) angle compared to their native forms. Of note, the azide molecule in the prokaryotic *T. thermophilus* structure is orientated differently than the eukaryotic structures, with the terminal N atom furthest from the manganese replacing the position of WAT2 and the geometry of the molecule deviating slightly from linearity, with a N1-N2-N3 angle of 175°. It is also noteworthy that the *T. thermophilus* structure is the only one determined at room temperature.

There are other subtle structural differences in the active site solvent. WAT2 of both structures and both chains has a B value near 30 Å² compared to the average solvent values of 26

and 24 \AA^2 of the native and azide structures, respectively. While WAT2 is the least-defined atom of the hydrogen bond network in our structures, its higher B factor may be reflective of a dynamic nature during catalysis, and the same feature has been observed in the 100 K MnSOD structure from *C. elegans* [98]. The 100 K structure from *E. coli* reveals a well-defined WAT2, with an average B value of 18 \AA^2 between the four chains among an average solvent value of 28 \AA^2 [133]. Studies of the catalytic mechanism have relied on the presence of WAT2 to shuttle protons to the active site metal but its presence in crystal structures may be a feature of cryocooling [90].

2.3.2 Electrostatic Guidance of Anionic Substrate to the Active Site

Due to the anionic substrate, the solvent accessible surface area near the active site was hypothesized to be basic [134]. To study this, three electrostatic surfaces of the human MnSOD tetramer were calculated with differing active site coordination of an oxidized manganese ion (Mn^{3+}): (1) five-coordinate with water as the solvent ligand (Figure 2.2a), (2) five-coordinate with hydroxide as the solvent ligand (Figure 2.2b), and (3) six-coordinate with hydroxide and superoxide ligands (Figure 2.2c). The position of the superoxide was modeled from the first two nitrogen atoms of the azide bound to the active site manganese in chain A. For these calculations, the partial charges for the atoms of all molecules ligated to the manganese ion were obtained from the work of Neves and coworkers [129]. These complexes represent the first half of the dismutation reaction. Unfortunately, partial charges for reduced manganese (Mn^{2+}) are currently not available.

The resulting electrostatic surfaces reveal how substrate diffusion to the active site could be enhanced. Of the three coordination states modelled, the electrostatic surface near the five coordinate active site “pit”, with water as the solvent ligand, is the most basic (Fig 2.2d). The pit is also more basic than the rest of the tetramer and there is a “valley” of positively-charged patches surrounding the pit (Fig 2.2g). Coordination of hydroxide as the solvent ligand instead of water lowers the electrostatic surface potential of the active site pit (Fig 2.2e). The differing active site states had no effect on the electrostatic surface potentials of the valleys (Fig 2.2h, i). The six

coordinate active site pit with superoxide bound with hydroxide as the solvent ligand has a nearly neutral electrostatic surface potential at the pit (Fig 2.2f). Azide and hydroxide are known inhibitors of SODs and bind to the sixth coordinate position, presumably like superoxide [93-95,133]. Binding of these inhibitors to the active site could neutralize the surface potential like superoxide does and provide yet another means of inhibition.

Direct evidence on whether the coordinated solvent ligand is a water molecule ($\text{Mn}^{3+}\text{-OH}_2$, Fig 3a) or a hydroxide molecule ($\text{Mn}^{3+}\text{-OH}^-$, Fig 2.2b) has been difficult to discern due to experimental limitations. Steady-state kinetic analysis of FeSOD from *E. coli* suggest the oxidized Iron has a hydroxide ligand coordinated ($\text{Fe}^{3+}\text{-OH}^-$) and proton uptake at the active site upon reduction of the metal ion results in $\text{Fe}^{2+}\text{-OH}_2$ [96]. NMR studies of FeSOD and MnSOD from *E. coli* reveal that amino acids at the active site do not become protonated upon metal ion reduction and the solvent ligand is the most probable proton acceptor [69]. Further studies using density function calculations show that such protonation is energetically favourable in both *E. coli* FeSOD and human MnSOD [90]. These studies support the $\text{Mn}^{3+}\text{-OH}^-$ state as the most chemically likely.

2.3.3 Players in Electrostatic Guidance and Substrate Entry into the Active Site

The most influential residues to the electrostatic surface potential were identified by mapping charged residues to the surface (Fig 2.3a). The outer ridge is populated by negatively-charged glutamate and aspartate residues while positively-charged lysine and arginine residues are found in the active site valley and pit. The residues from both subunits at the dimeric interface (red dashed line, Fig 2.3a) combine to form a valley of positive surface potential. These calculations indicate that anionic substrate is repelled away from the negatively-charged outer ridge of the hMnSOD tetramer and attracted into the center, towards an active site.

A cross-section view of the active site pit provides insight into the interaction of superoxide with the surface that enhances collision with the metal ion (Fig 2.3b). Three positively-charged residues contribute to the basic surface potential at the active site pit, Lys29 of chain A and

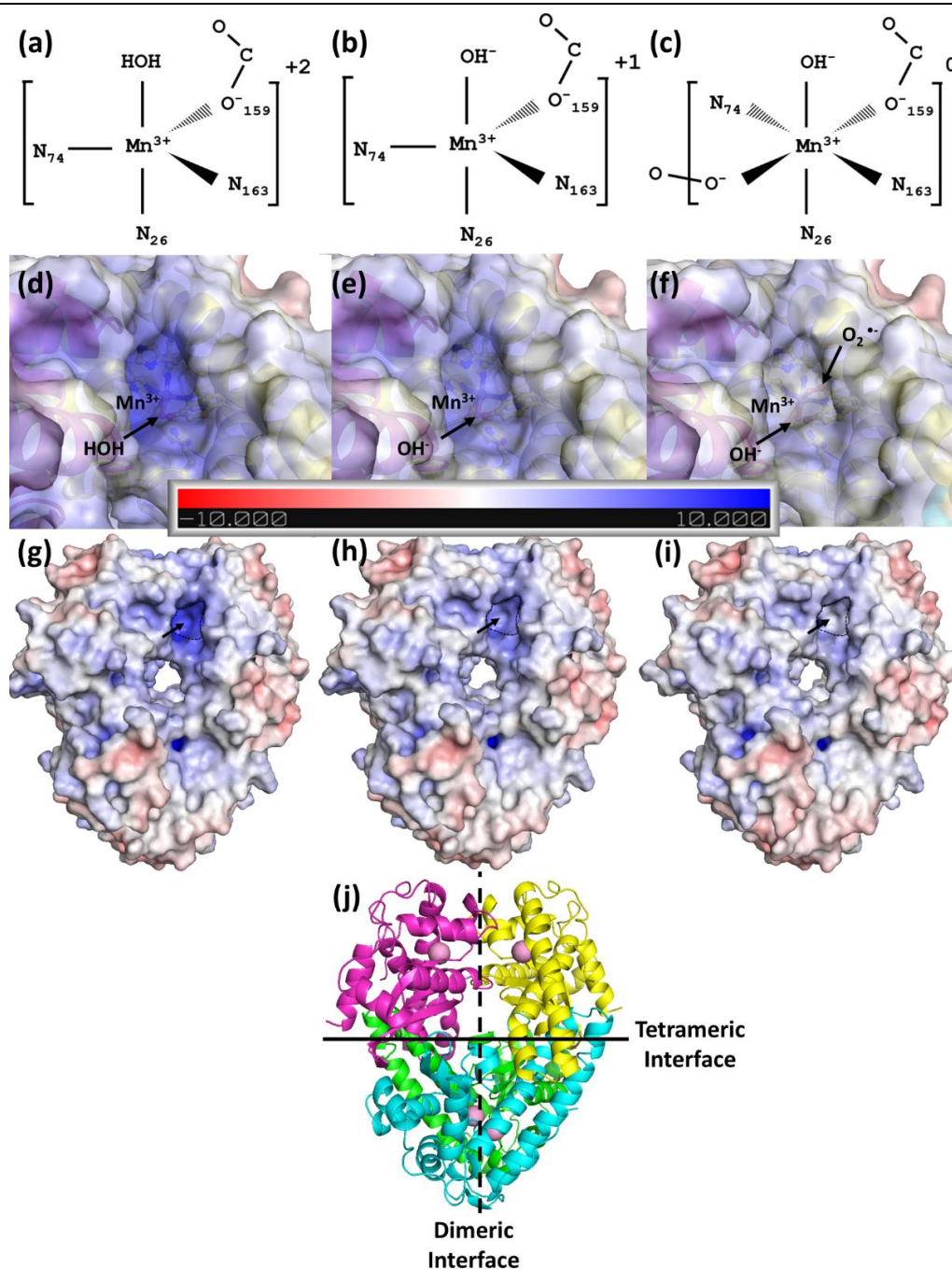
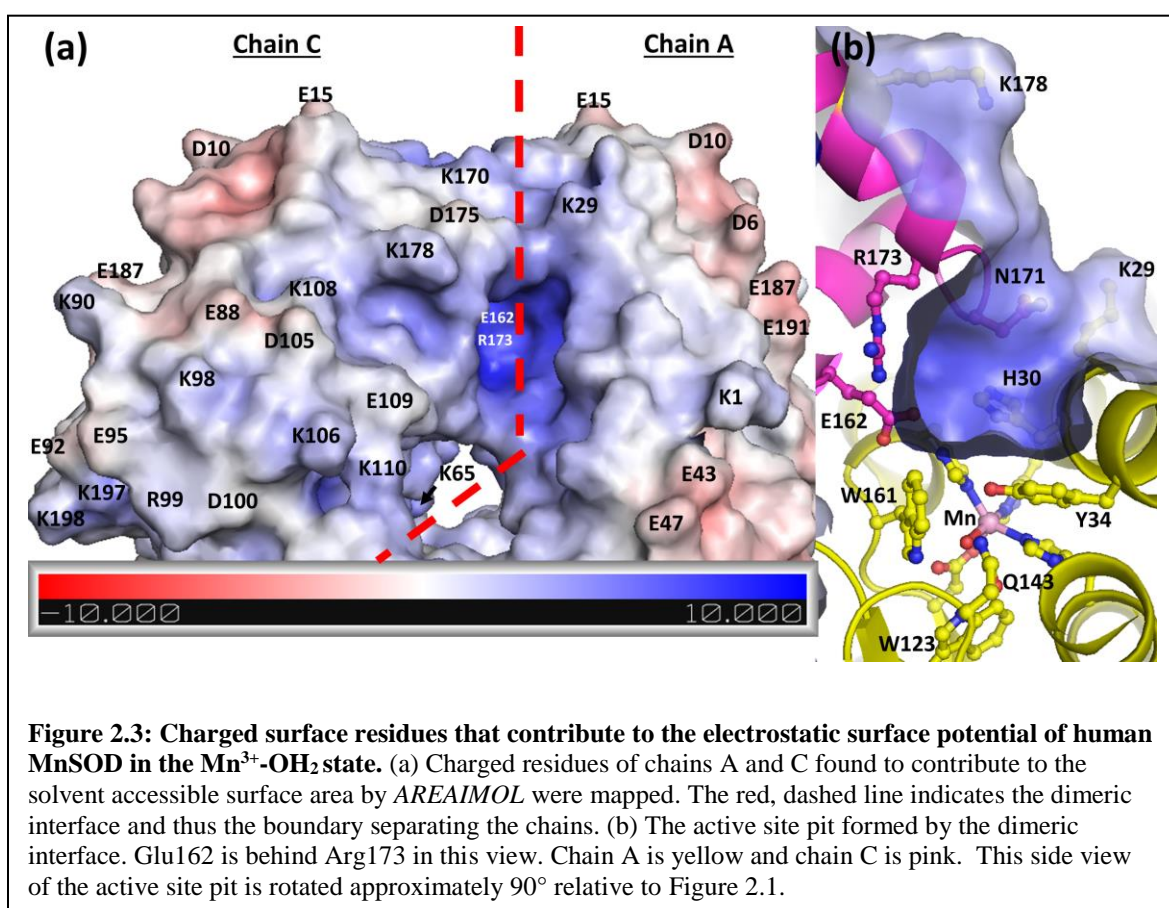


Figure 2.2: Solvent accessible (sphere radius = 1.4 Å) electrostatic surfaces of oxidized human MnSOD with differing active site coordination. (a-c) Differing models of active site coordination used to generate the subsequent electrostatic surfaces. (d-f) Electrostatic potential at the active site quantified in kT. (g-i) Electrostatic potential of the tetramer. Arrow indicates one of four active sites seen with this orientation. (j) Ribbon diagram of the tetramer. Pink spheres indicate manganese ions and location of the active sites. Vertical dashed line indicates the dimeric interface that is evolutionarily conserved and the horizontal line indicates the tetrameric interface.



Arg173 and Lys178 of chain C. For *E. coli* MnSOD, an electrostatic surface study also found a positively charged active site pit with a similar cluster of positively charged residues, consisting of four arginine residues contributed by two chains [110].

The high rate constant of MnSOD indicates that nearly all collisions to the active site are productive, and electrostatic forces may provide some pre-collision orientation. The placement of Glu162 and Arg173 6 Å apart may contribute to the effective diffusion of substrate into the active site. Glu162 is the closest negatively charged residue to the manganese ion, being 7 Å away, and Arg173 is the closest positively charged residue, being 12 Å away. Arg173 could draw in anionic substrate toward the gateway residues while Glu162 prevents non-productive association with Arg173. A similar pair of amino acids have been suggested for bovine CuZnSOD, where Glu131 and Lys134 were found to work together to diffuse superoxide towards the active site [134].

Glu162 and Arg173 are conserved spatially in the *C. elegans*, *T. thermophilus*, and *E. Coli* MnSOD structures (PDB entries **5AG2**, **1MNG**, and **1D5N**, respectively) and appear to be important for catalytic activity. Glu162 from across the dimer interface hydrogen bonds with Mn ligand His163. In *E. coli* MnSOD, residue Glu170 (Glu162 in human) is essential for dimer stability and metal selectivity [135]. For human MnSOD, Glu162Asp and Glu162Ala mutations retain the tetramer but activity is decreased 5-25% and the level of product inhibition is increased 2-fold [89], indicating that Glu162 fulfils more than an electrostatic role. Previous studies have shown a positive charge at position 173 is essential for catalysis and enzyme activity can be abolished by chemical modification at this site [136,137] This model of human MnSOD indicates that positively-charged residues line the active site pit and strategic placement of Glu162 and Arg173 may contribute to productive interaction of anionic substrate with the active site.

Human MnSOD activity is regulated by post translational modifications [138,139]. The activity of MnSOD in cells is reduced through acetylation of lysines [140,141]. Acetylation causes lysines to be neutral in charge and presumably decreases superoxide attraction to the active site.

Changes in net charge of the protein via acetylated lysines, even if far from the active site, could change the vector direction of the electrostatic field, as exemplified by Getzoff and coworkers [134]. Also, mass spectrometric analysis showed that Arg173 is dimethylated in proliferating and quiescent human fibroblast cells [142]. Methylation does not change the net charge of the arginine residue but adds bulky groups and reorients the charge. The functional role of Arg173 methylation and contribution to activity is unclear. How posttranslational modifications regulate MnSOD activity are of medical interest and the topic of future mechanistic studies.

2.4 Conclusions

The crystal structure of the human MnSOD-azide complex, and in conjunction with electrostatic surface calculations, provides a model for the entry and binding position of the superoxide substrate to the active site. When inferring mechanistic data from the postulated superoxide binding site, the human and the recent *C. elegans* structures provide better models when comparing eukaryotic MnSOD structures. Electrostatic calculations suggest anionic substrate is guided toward the active site of MnSOD by a negatively-charged outer ridge and positively charged central valleys. Superoxide is then correctly oriented by Glu162 and Arg173, enters the active site by passing gateway residues Tyr34 and His30, and binds to the manganese ion at the sixth coordinate position.

Chapter 3: Developing a System for Neutron Diffraction of MnSOD

3.1 Introduction

Despite their biological importance, the complete multistep enzymatic mechanisms of SODs are unknown due to limitations in identifying the hydrogen positions at the active site. Knowledge of the hydrogen positions are critical because (1) they are needed to differentiate the ligands in the active site, which are hypothesized to differ based on the redox state of the active site metal [93], and (2) they reveal the source and pathway of protons to the catalytic center for proton-assisted electron transfer.

All X-ray crystal structures of MnSOD and FeSOD have an oxygen molecule coordinated to the active site metal which is thought to be involved in proton-assisted electron transfer. Whether the oxygen is a water or hydroxide molecule is not known due to the low X-ray scattering factor of hydrogen atoms and insufficient diffraction resolution. The hydrogen content of the molecule is postulated to depend on the redox state of the metal [69,90]. Discerning between superoxide and hydrogen peroxide is also difficult in X-ray crystallography. Hydrogen peroxide is produced during the oxidation step of the metal and dissociation of the oxidized product inhibited complex. X-ray crystal structures of fully-oxidized metalloproteins cannot be measured since photo-electrons reduce the metals during X-ray data collection [75]. This is yet another advantage of neutron crystallography, where the oxidation state of the active site metal is unaffected by the beam.

The source and pathway of proton transfer(s) used to dismute superoxide is not known. A conserved hydrogen bond network involving the coordinated oxygen molecule to the metal and several residues has been presumed to shuttle protons from bulk solvent to the catalytic center [63,93,143]. Mutation of residues contributing to the hydrogen bond network has been shown to highly affect catalytic activity and has suggested two differing pathways for reduction of superoxide [63,71,87,144].

Neutron diffraction of human MnSOD is being used to uncover the hydrogen positions, effect of metal oxidation state, the proton relay pathway, and the catalytic mechanism of SODs. Here, methods are presented for the production of perdeuterated human MnSOD, purification, large crystal growth, and neutron data collection to 2.30 Å using the MaNDi single-crystal diffractometer at Oak Ridge National Laboratory (ORNL). Perdeuteration, replacing every hydrogen atom with deuterium, was performed using the Perdeuteration Facility at ORNL. Perdeuteration is advantageous as it decreases the incoherent scattering by 40 fold compared to a hydrogenated sample thereby reducing background and increasing the resolution of diffraction. Our crystal system was particularly challenging for neutron diffraction due to our large unit cell edge of 240 Å. The human MnSOD data set provides the largest unit cell edge to be collected via neutron diffraction to sufficient resolution where hydrogen positions can be observed.

3.2 Materials and Methods

3.2.1 Adaptation to Deuterium

Full length human MnSOD cDNA optimized for *E. coli* codons was cloned into the pCOLADuet-1 expression vector and transformed into BL21(DE3). Cells were grown in Terrific Broth with 0.8% (v/v) glycerol while cell strain fidelity was maintained with 30 µg mL⁻¹ of kanamycin for initial growth and deuterium adaptation. Deuterium adaptation was performed by subculturing from Terrific Broth to H₂O minimal media and subsequent subcultures into increasing ratios of deuterium labelled minimal media (25, 50, 75 and 100%). Subculturing was performed by 1:5 dilutions into 3 mL of media from an OD₆₀₀ of 1 to a final of 0.2. The composition of minimal medium used for deuterium adaptation and human MnSOD expression was as follows: 5 g L⁻¹ D₈-glycerol, 7 g L⁻¹ (NH₄)₂SO₄, 0.5 g L⁻¹ ammonium citrate dibasic, 5.25 g L⁻¹ Na₂HPO₄, 1.6 g L⁻¹ KH₂PO₄, 1 mL L⁻¹ of 20% MgSO₄·7H₂O, and 1 mL L⁻¹ of trace elements solution [145]. The 1000X trace elements solution contained 0.500 g L⁻¹ CaCl₂·2H₂O, 0.098 g L⁻¹ CoCl₂, 0.160 g L⁻¹ CuSO₄·5H₂O, 16.7 g L⁻¹ FeCl₃·6H₂O, 0.114 g L⁻¹ MnSO₄·H₂O, 22.3 g L⁻¹ Na₂EDTA·2H₂O, and

0.180 g L⁻¹ ZnSO₄·7H₂O [146]. For perdeuterated medium preparations used for fed-batch cultivation, minimal medium salts were dried and exchanged three times using a rotary evaporator prior to dissolution in 99.8% D₂O [147]. All other solutions were prepared with 99.8% D₂O and filter sterilized into dry, sterile containers prior to use.

3.2.2 Perdeuterated Expression

Once adapted to D₂O, glycerol stocks were stored at -80 °C for future use. All media used after adaptation used 100 µg mL⁻¹ kanamycin. In preparation for fed-batch cultivation, 25 µL of glycerol stock was used to seed 3 mL of D₂O minimal medium, which was subsequently shaken at 250 rpm and 37 °C. Once the culture reached an OD₆₀₀ of ~1, it was subcultured 3X in D₂O minimal medium at 1:20 dilution prior to scale-up for fed-batch cultivation, which utilized a Bioflo 310 bioreactor system (Eppendorf). Prior to inoculation, a 2.5 L bioreactor vessel was steam-sterilized and dried using sterile-filtered compressed air that had been first passed through a gas purifier containing Drierite® and 5 Å molecular sieves. Upon dryness, fresh perdeuterated minimal medium (1.4 L) was added to the vessel. Sensors for monitoring pH and dissolved oxygen were rinsed with deionized water and 70% ethanol prior to installation through the vessel headplate. Temperature and compressed air flow were set at 30 °C and 1.5 L min⁻¹ (1 vvm) respectively. To inoculate the vessel, 50 mL of D₂O-adapted cells were diluted to an initial OD₆₀₀ of 0.14. Throughout the experiment, agitation was increased from 200 rpm to maintain dissolved oxygen above a set point of 30% and 10% (w/w) NaOD was added on demand to control pD (>7.3). Upon depletion of D₈-glycerol, the dissolved oxygen spike was used to initiate addition (9 mL h⁻¹) of a feed solution consisting of 10% (w/v) D₈-glycerol and 0.2% MgSO₄ in 99.8% D₂O. Upon reaching an OD₆₀₀ = 8.3 after 21.8 hours, a D₂O-exchanged solution of MnSO₄ was added to 1.4 g L⁻¹ and perdeuterated human MnSOD overexpression was induced by adding IPTG to a final concentration of 1 mM. After 26.2 h, the cell suspension was collected and pelleted at 6,000 x g via centrifugation at 4 °C for 30 minutes to yield 63.7 g wet weight of perdeuterated cell paste.

3.2.3 Purification

For purification, cells were re-suspended in 50 mM potassium phosphate, pH 7.8, adjusted by altering the ratio of dibasic (K_2HPO_4) and monobasic forms (KH_2PO_4) to 91% and 9%, respectively [148]. Lysis was conducted with an Emulsiflex and clarified lysate was incubated at 60 °C for one hour to precipitate contaminant proteins which were removed by centrifugation. Soluble protein was dialyzed against 5 mM potassium phosphate, pH 7.8, and applied to pre-swollen diethylaminoethyl (DE52) cellulose resin (GE Healthcare). The protein-resin slurry was rocked for 1 hr at 10 °C and poured into a Büchner funnel set with Whatman #4 filter paper while under vacuum. Once dry, resin was washed with 5 mM potassium phosphate, pH 7.8, then protein was eluted with 100 mM potassium phosphate, pH 7.8. Eluted protein was dialyzed against 2.5 mM 2-(N-morpholino)ethanesulfonic acid (MES), pH 5.5, applied to a carboxymethyl (CM) sepharose (GE Healthcare) column, eluted with a sodium chloride gradient, and concentrated to 21 mg mL⁻¹ using 5 kDa molecular weight cut-off concentrators. Concentration was measured using a NanoDrop ND-1000 spectrophotometer using an extinction coefficient of 43.43 L mol⁻¹ cm⁻¹ at 280 nm. Purification of hydrogenated and deuterated protein were identical.

3.2.4 Crystallization

Optimization of large, hydrogenated crystal growth was conducted first. A protocol for hanging drop vapor diffusion growth was translated to a nine well glass plate sandwich box setups (sitting drop vapor diffusion, Hampton Research) and upscaled to 100 µl drops with differing ratios of protein at 21 mg mL⁻¹ to screen for large crystal growth. Well solution consisted of 1.8 M potassium phosphate, pH 7.8. Crystal setups were placed on neoprene vibration isolation pads (Grainger 5XR47) and kept inside an incubator kept at 20 °C (RUMED Rubarth Apparate GmbH). Ratios of protein to well solution of 3:2, 1:1, and 2:3 yielded the largest and highest quality crystals, as measured by X-ray diffraction resolution and mosaicity. Large crystal growth was also achieved at 10 °C using a higher salt concentration, of 2.5 M potassium phosphate at pH 7.8.

Crystals grew up to 3 mm³ after a month, although the largest crystals all had imperfections and/or diffracted X-rays poorly.

To identify if differing crystallization conditions were needed for perdeuterated crystals, a hanging drop grid screen was performed using 2 µl drops of 1:1 protein to well solution with varying pH and concentrations of potassium phosphate both at room temperature and 10 °C. Growth utilizing a reservoir solution of 1.93 M potassium phosphate, pH 7.8, at room temperature and 2.50 M potassium phosphate, pH 8.0 (adjusted by altering ratios of dibasic and monobasic forms, 94% and 6%, respectively), at 10 °C consistently yielded single crystal growth. The condition was translated to perdeuterated large crystal growth using 100 µl drops with protein, 21 mg ml⁻¹, to well solution ratios of 3:2, 1:1, or 2:3. Large volume crystals were grown at 20 °C in the same glass trays and incubator set up as described above. In these setups, perdeuterated crystals grew up to 2 mm³ after 3 weeks, though the largest crystals diffracted poorly with X-rays and displayed high mosaicity. A 0.26 mm³ perdeuterated crystal was used to collect our neutron data set.

3.2.5 Deuterium Exchange

To vapor exchange titratable hydrogens in the crystals with deuterium, a suitable deuterated substitute reservoir solution was needed. For crystals grown in 1.93 M potassium phosphate, pH 7.8, at 20 °C, total substitution of reservoir with 2.43 M deuterated potassium phosphate, pH 7.4 (pD 7.8), maintained crystal stability. Likewise, crystals grown in 2.50 M potassium phosphate, pH 8.0, at 10 °C maintained stability with substitution to 3.00 M deuterated potassium phosphate, pH 7.6 (pD 8.0). In general, a deuterated substitute reservoir solution 0.5 M above our native reservoir concentration caused no observable alterations in our crystals.

3.2.6 Preparation for Neutron Diffraction

To prepare for neutron data collection, crystals were mounted into quartz capillaries, vapor exchanged with deuterium, screened for diffraction viability using X-rays, and safely transported from the home lab to ORNL. These steps are described in detail below.

For mounting crystals, thick-walled quartz capillaries (VetroCom, 1.5 ID X 1.8 OD, CV1518-Q-100) were preferred due to their transparency to neutrons and durability during handling and travel. Crystals were carefully drawn into the capillaries from their crystallization drops using a Captrol III Drummond Scientific Aspirator connected to rubber tubing with vacuum grease. Approximately 20 μ l of reservoir solution was added to the crystallization drops prior to mounting to account for solution being drawn into the capillary. Crystals fixed to the well plates could be dislodged by repeatedly pipetting around the crystal slowly using a standard pipet. Once crystals were drawn into the capillaries, native mother liquor was removed and dried using paper wicks to avoid crystal slippage. A conservative amount of mother liquor was left on the crystal to prevent its drying. Slugs of deuterated substitute reservoir solution, 10 μ l, were placed on both sides of the crystal and the capillary was sealed by heating and cooling beeswax. To ensure saturation of deuterium exchange, capillaries were opened after 1 week with a heated syringe needle and the slugs of deuterated reservoir were replaced with fresh solution before being resealed.

To preliminarily assess whether our crystals would be viable for neutron diffraction, diffraction was tested with 5 second exposure to X-rays. Exposures were kept as short as possible to avoid radiation damage but had to be extended to 5 seconds due to the thickness of the quartz capillary and the size of the crystal.

To further secure the beeswax seals of the capillaries, a thin layer of fingernail polish was applied prior to travel. Capillaries were either placed in 15 mL conical tubes surrounded by cotton wool or fastened in DVD cases with clay. Tubes and DVD cases were placed in cushioned areas of

luggage during travel, such as between foam padding in a dedicated suitcase that was checked or in a hand carried backpack.

Upon arrival to ORNL and prior to data collection, crystals were dried again to a minimal amount of mother liquor to minimize background signal and to avoid crystal slippage. Time-of-flight (TOF) neutron diffraction data from a perdeuterated crystal 0.26 mm^3 in volume at 293K were initially recorded to 2.30 \AA using the MaNDi instrument [149,150] at the Spallation Neutron Source (SNS) onsite at ORNL using all neutrons between 2 to 4 Ångstrom (Table 3.1). The omega angle was fixed at 90° for data collection and each image was separated by a 20° phi rotation. These six images were processed and integrated using the Mantid package [151] and the Lauenorm program from the Lauegen package [152]. Lauenorm performs a wavelength normalization of the Laue data and scaling between Laue diffraction images. The X-ray diffraction data were collected at 293K on an in house Rigaku MM007-HF equipped with an RAXIS IV++ detector and were processed using the XDS package [153] and the Scala program from the CCP4 suite [154].

3.3 Results and Discussion

To produce deuterated human MnSOD, *E. coli* cells harbouring the recombinant plasmid were needed to grow in deuterated minimal media. BL21(DE3) cells with the endogenous SODs were used to adapt to fully deuterated media. Adaptation was performed by subculturing from Terrific Broth to H_2O minimal media and subsequent subcultures into increasing ratios of deuterium labelled minimal media (25, 50, 75 and 100%) at OD_{600} of 1. Subculturing was performed by 1:5 dilutions into 3 mL of media from an OD_{600} of 1 to a final of 0.2 Expression of recombination human protein upon induction with IPTG was verified with a SDS-PAGE (Figure 3.1). Purification of human MnSOD were performed with nearly identical protocols as for the

Table 3.1 X-ray and Neutron Data Collection Statistics for a 0.26 mm³ Crystal

Diffraction source	Rigaku MM007-HF	MaNDi
Wavelength(s) (Å)	1.54	2-4
Temperature (K)	293	293
Detector(s)	Raxis IV++	40 SNS Anger cameras
Xtal-to-detector distance (mm)	200	450
Rotation range per image (°)	0.25	Fixed
Number of Images Collected	400	6
Total rotation range (°)	100	60
Exposure time per image	30 seconds	48 hours
Space group	P6 ₁ 2 2	P6 ₁ 2 2
a, b, c (Å)	81.40, 81.40, 242.0	81.31, 81.31, 242.0
α , β , γ (°)	90,90,120	90,90,120
Resolution range (Å)	19.71 – 2.35 (2.48 – 2.35)	14.62 – 2.30 (2.38 – 2.30)
Total No. of reflections	228827	43593
No. of unique reflections	20582	16318
Completeness (%)	99.7 (99.8)	74.29 (68.83)
Redundancy	9.0 (11.0)	2.67 (2.07)
$\langle I/\sigma(I) \rangle$	8.7 (2.70)	5.4 (2.70)
R _{merge} (%)	7.6 (27.0)	19.2 (22.8)
R _{pim} (%)	2.30 (8.7)	11.1 (15.9)

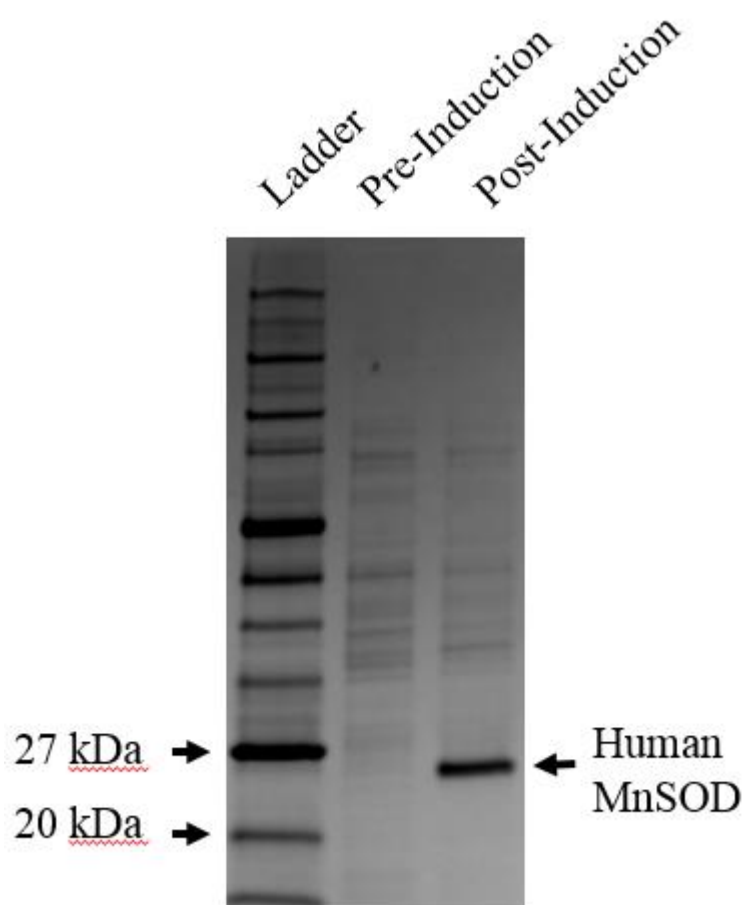


Figure 3.1: Fermenter growth of perdeuterated human MnSOD. SDS-PAGE of whole cell lysate from cells grown in perdeuterated media immediately before and 13 hr after induction. Monomeric human MnSOD has a molecular weight of 22 kDa. Samples were normalized to equivalent optical densities.

hydrogenated form (Figure 3.2). Contamination by dimeric *E. coli* SODs were not detected on native gels (data not shown). Any concerns about such contamination were relieved when the perdeuterated sample crystallized in the space group and unit cell that is only associated with human MnSOD.

Prior to obtaining our neutron data set of a perdeuterated crystal, we attempted to collect data sets with hydrogenated crystals, 1.0-1.2 mm³, with titratable hydrogens exchanged with deuterium. Though these crystals diffracted well with X-rays, neutron data collection yielded diffraction up to 2.95 Å, a resolution insufficient to accurately observe hydrogen positions. The extent of diffraction was attributed to the large unit cell edge of 240 Å and incoherent scattering given by the hydrogen atoms at non-titratable positions. To improve diffraction intensities and extend the diffraction limit, data was later collected on perdeuterated crystals. The highest diffraction limit, to 2.30 Å, was achieved with a 0.26 mm³ perdeuterated crystal (Figure 3.3).

Large unit cell axes are highly problematic in Laue diffraction experiments due to the large number of closely packed reflections they generate [155]. Without the use of TOF methods which enable a multi wavelength Laue diffraction pattern to be broken up into monochromatic slices (Figure 3.4) a large proportion of the reflections would be spatially overlapped [149,156]. Furthermore, the reflection diffraction intensity is directly related to the volume of the crystal and the volume of the unit cell making data collection on large unit cells using the low flux available at neutron beams particularly challenging.

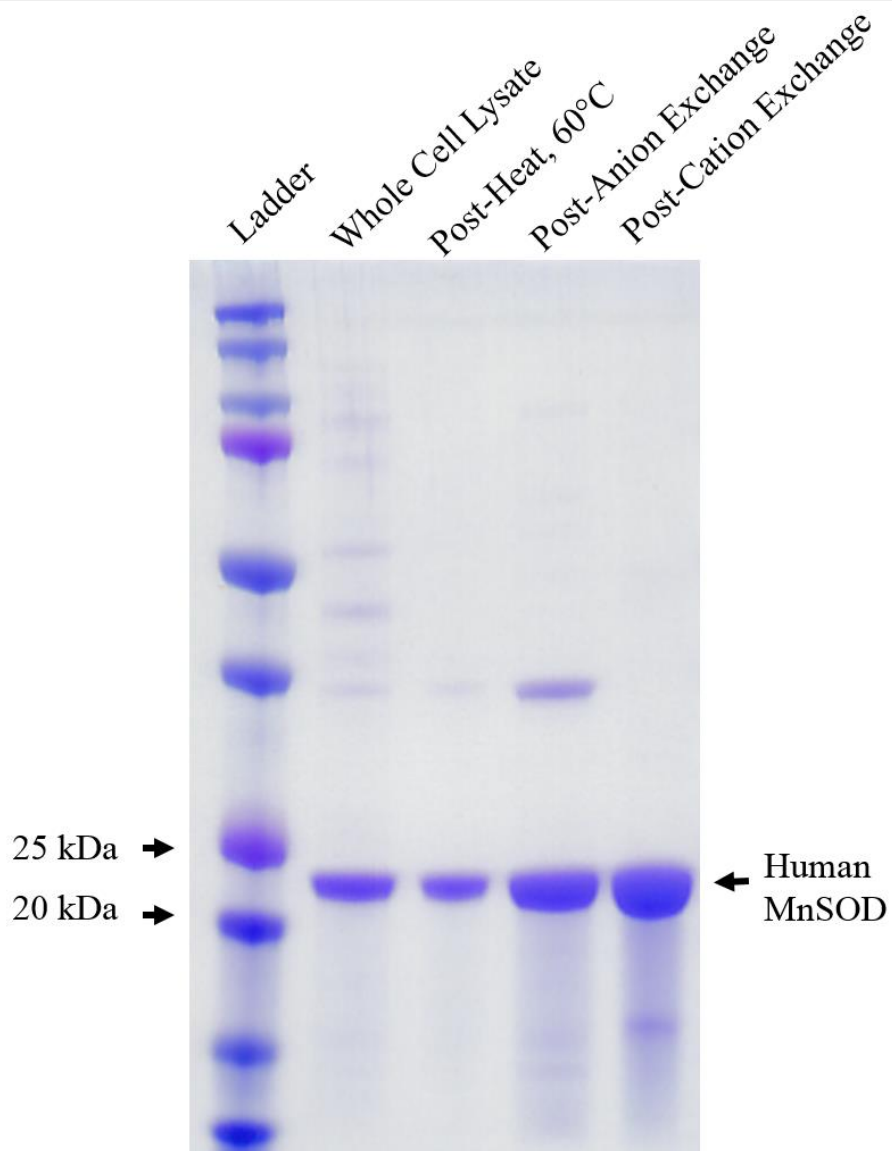
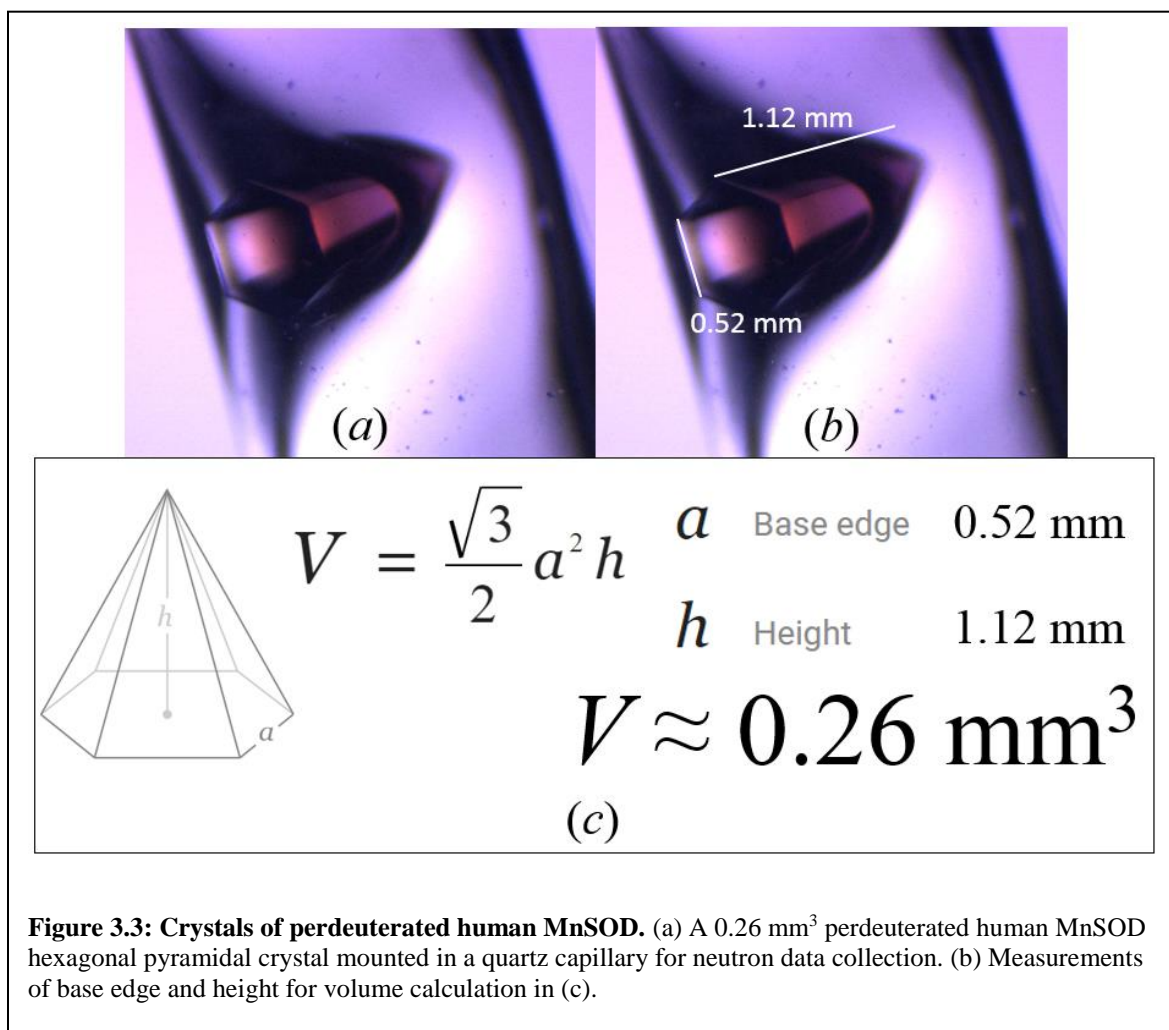


Figure 3.2: Purification of human MnSOD. SDS-PAGE of perdeuterated human MnSOD during purification. Purification steps are sequential from left to right. Heat was applied by placing samples in a water bath, anion exchange was conducted using DE52 resin and eluted with 100 mM potassium phosphate, pH 7.8, and cation exchange was performed with a CM column and eluted with a sodium chloride gradient. See materials and methods for further details of purification.



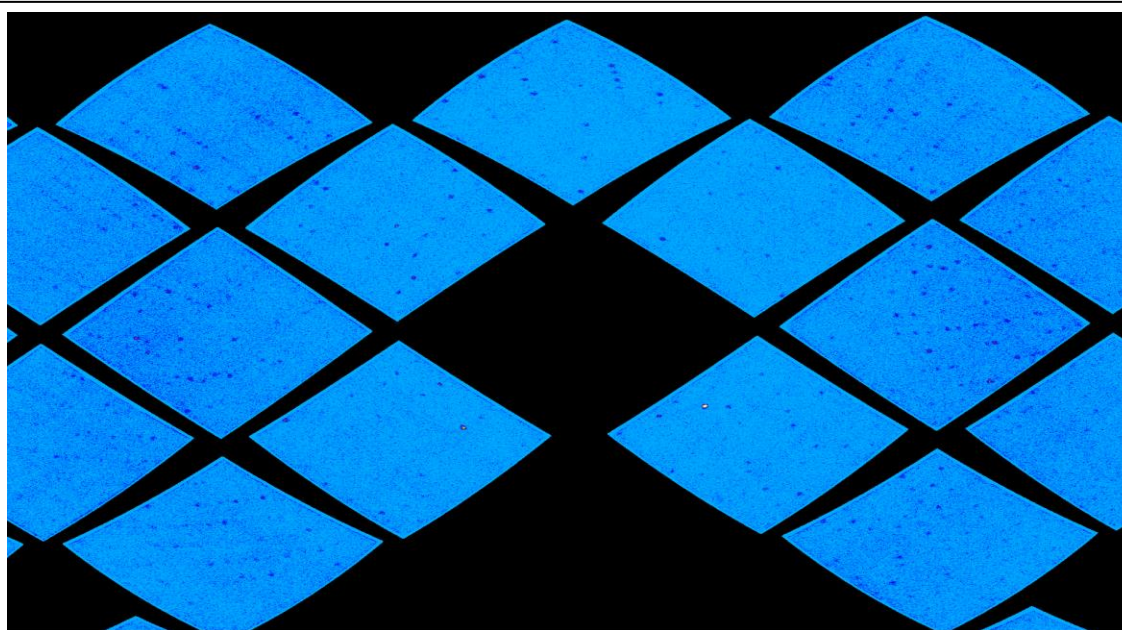


Figure 3.4: The diffraction pattern of human MnSOD from the spherical detector orientation of MaNDi. A selected time-of-flight slice of neutrons with wavelength of 3.0 - 3.1 Å is shown.

Chapter 4: Redox Manipulation of MnSOD

4.1 Introduction

A large body of literature has attempted to discern the catalytic mechanism of human MnSOD but still remains enigmatic [63,69,71,72,90,93,99,101,102,104-108,157]. The difficulty in elucidating the mechanism is attributed to limitations in detecting hydrogen positions at the active site, especially for X-ray crystallography. Knowledge of the hydrogen positions is paramount to understanding the mechanism because the cyclic redox reaction of MnSOD relies on the coupling of electron transfers to proton transfers, also called proton-coupled electron transfers (PCETs) [158]. A consensus among the MnSOD literature is that proton-shuttling relays are present around the manganese ion to mediate systematic PCETs, as noted by the following detailed reviews [63,157]. This facilitates one of the fastest ($k_{\text{cat}} = 40,000 \text{ s}^{-1}$) and most efficient (k_{cat}/K_M close to $10^9 \text{ M}^{-1} \text{ s}^{-1}$) reactions among all enzymes [91]. At least two unique relays exist, where utilization of a relay is based on the oxidation state of the manganese. The exact path of the proton relays has yet to be determined [104,112,157].

Neutron protein crystallography is able to find hydrogen positions, unlike its X-ray counterpart [120,159]. This is a consequence of neutron coherent scattering lengths of deuterium atoms being on par with carbon, nitrogen, and oxygen whereas the X-ray scattering lengths of hydrogen and deuterium are approximately an order of magnitude less than the second row organic atoms [160]. Deuterium is especially noteworthy for neutron diffraction because it has 40 fold less incoherent scattering (i.e. background noise) compared to hydrogen and scatters positively whereas hydrogen scatters negatively [120]. Perdeuteration, replacing every hydrogen atom with deuterium, takes advantage of the properties of deuterium to improve neutron diffraction of a sample. Since 50-80% of a protein crystal is typically water, using deuterated water (D_2O) and as many deuterated mother liquor components as possible causes a large reduction in incoherent neutron scattering—reducing background. Half of all atoms found in biological macromolecules are

hydrogen, so replacing all hydrogen atoms with deuterium in the protein (perdeuteration) gives a sample that is fully optimized for neutron data collection. Perdeuteration also negates the issue of nuclear scattering density cancellation, where a combination of positive and negative scattering of nearby atoms yields a net scattering of zero. Combining the above use of deuterium and neutron crystallography makes discerning the catalytic mechanism of MnSOD possible.

Investigating mechanisms of oxidoreductase metalloproteins is challenging using X-ray diffraction. Metals are susceptible to being reduced by X-ray radiation, thus studying a completely oxidized metal complex is not feasible [75]. Even X-ray structures of MnSOD that are published as containing fully oxidized manganese ions are actually partially reduced, as determined by quantum mechanical and molecular modelling [107,112,161]. When using neutrons, which are a nonionizing probe, no sort of radiation damage and consequently no redox changes occur to the metals [120,162]. As MnSOD utilizes differing proton relays based on the redox state of the manganese, being able to study both fully oxidized and fully reduced samples is crucial to understanding its mechanism [104,112,157].

In our previous work, we created a crystal system for MnSOD that was reliably applicable to neutron crystallography [163]. The known high symmetry space group ($P6_3/22$) MnSOD crystal system was attractive since all precipitating agents could be purchased in a deuterated form and complete, redundant data could be collected in a handful of data frames (neutron beamtime is precious). Unfortunately, the cell dimensions are large ($a = b = 90 \text{ \AA}$, $c = 240 \text{ \AA}$) but is the largest unit cell to visualize hydrogen positions to date. The unit cell volume is especially difficult for neutron crystallography due to the low flux of neutron beamlines and the spatial overlap of reflections that large unit cells generate [155]. The macromolecular neutron diffractometer (MaNDi) beamline at Oak Ridge National Laboratory (ORNL), commissioned in 2014, circumvented the challenge of this large unit cell by using time-of-flight Laue (i.e. multiwavelength) diffraction [164,165]. Time-of-flight information allows polychromatic

diffraction patterns to be resolved into monochromatic slices, allowing discrimination of spatially overlapped reflections that are especially problematic with crystals harbouring large unit cells [156,164]. In conjunction with MnSOD perdeuteration and moderate crystal volumes ($> 0.25 \text{ mm}^3$), neutron diffraction using the MaNDi beamline was achieved up to a resolution (2.14 \AA) where deuterium positions could be observed [163].

After developing a pipeline for MnSOD perdeuteration, large crystal growth, and neutron diffraction to a resolution where hydrogen positions can be visualized, we next endeavoured to control the redox state of the manganese ion in this system. Visualizing the proton environment where the manganese ions are either all trivalent or divalent (rather than the native, mixed state) provides important snapshots of the proton-based catalytic mechanism, where differences in proton positions can then be used to track the path of proton transfers. In this work, several methods are provided for controlling the redox state of the active site manganese ion within MnSOD crystals (i.e. after crystallization) for neutron crystallography. The redox manipulation techniques described are intended to be applicable to other sorts of crystal treatments (neutron or X-ray) or other metalloprotein crystal systems.

4.2 Materials and Methods

4.2.1 Perdeuterated Expression, Purification, and Crystallization

The details of methods for perdeuteration, expression, purification, and crystallization of MnSOD were previously described in Chapter 3 section 2.

4.2.2 Redox manipulation

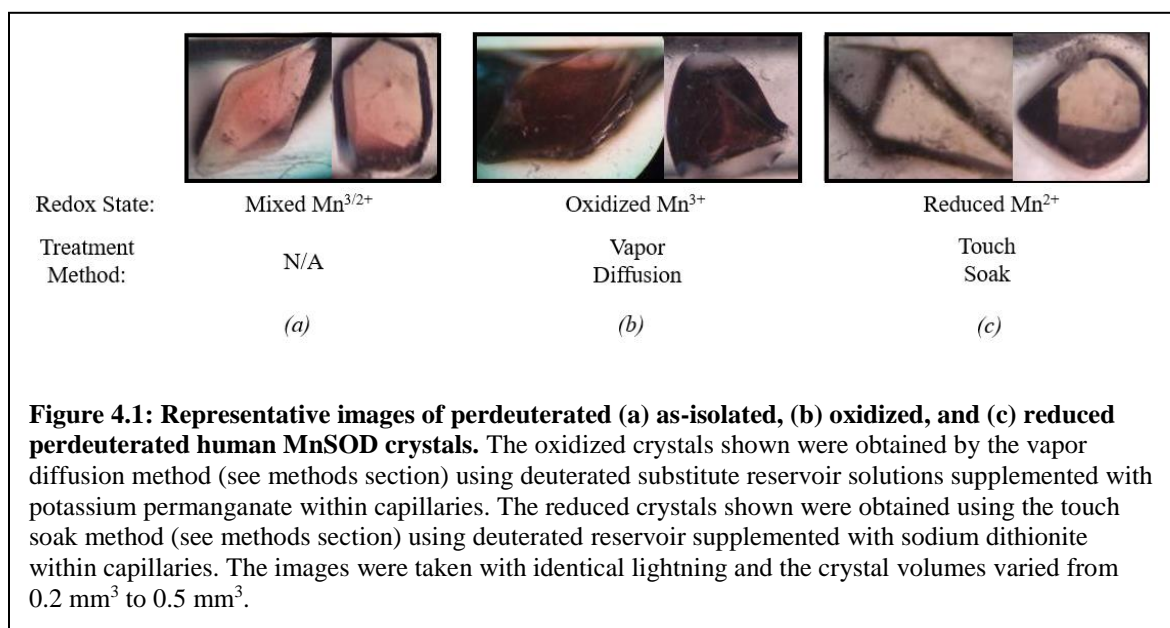
Reduction of MnSOD was achieved with these chemicals, (1) hydrogen peroxide, (2) sodium ascorbate, and (3) sodium dithionite. Potassium permanganate was used as an oxidizing agent. These chemicals were supplemented in the deuterated substitute reservoir solution, composed of 2.43 M deuterated potassium phosphate pH 7.4 (pD 7.8). The redox state of the

manganese is detected by the intensity of the pink color of the crystals (Figure 4.1). A deep pink color indicates Mn(III) ions and colorlessness indicates Mn(II) ions [93,105]. Of note, electroparamagnetic resonance and optical spectra studies verify exclusive formation of Mn(III) from potassium permanganate oxidation and not Mn(IV) [98,166-169].

Hydrogenated MnSOD was first crystallized in each well of a 24 well crystallization plate (VDXm plate from Hampton Research) via hanging drop vapor diffusion using identical crystallization conditions for each well, 1.8 M potassium phosphate pH 7.8. 1 μ l each of reservoir solution and 23 mg ml⁻¹ protein was used for the crystallization drop with crystals growing no bigger than 0.05 mm³ [163]. Redox agent was then added to each reservoir solution in a gradient concentration across the whole plate along with concentrated potassium phosphate pH 7.8 to maintain the original molarity when necessary. The ‘new’ reservoir solution and the crystal were then allowed to vapor diffuse with each other for one week. The persistence of the native light-pink color (Figure 4.1a) was representative of too little redox agent while cracked or deformed crystals were characteristic of too much. Concentrations of redox agent that were able to change the intensity of pink without visibly compromising crystal integrity were used as a starting point to optimize redox changes of larger crystals contained within a capillary.

After mounting crystals in a capillary (mounting method provided in detail in [163]), three techniques were explained to control the redox state of the manganese ions of MnSOD crystals, vapor diffusion, a ‘touch soak,’ and a full soak.

First, the oxidation state of the manganese could be controlled solely through vapor diffusion by supplementing the redox reagent into the deuterated substitute reservoir solution intended to keep the crystal hydrated. The length of time in which the redox changes could be observed varied with concentration of the agent and the distance between the solution and the crystal. This was the primary method for obtaining oxidized crystals and was achieved by allowing



reservoir solutions supplemented with 6.4 mM potassium permanganate to vapor diffuse with the sample.

Second, touch soaking was used when vapor diffusion was insufficient. This is achieved by cautiously using a pipet to move the redox agent supplemented reservoir slug within the capillary to barely contact the crystal. The slug is then pipetted away when the redox change is complete, which is intended to occur within a timeframe of seconds. To reduce the crystals with hydrogen peroxide (0.25-1.00%), this was the predominant method used.

Finally, a full soak of crystals in redox agent-supplemented deuterated substitute reservoir solution was performed while the sample is still within the capillary. Changes were observed within seconds but soaks could be performed over several days to ensure a persistent shift of oxidation state. This was the primary method for obtaining reduced crystals and was achieved by soaking crystals in reservoir solution supplemented with 0.2 M sodium dithionite.

4.2.3 Neutron Data Collection

Prior to data collection, reservoir slugs of the capillaries bearing the crystal samples were replaced with fresh deuterated reservoir solution supplemented with redox agent. Neutron data was obtained on oxidized and reduced perdeuterated human MnSOD crystals (Table 4.1). Time-of-flight wavelength-resolved neutron Laue diffraction data [156] was collected on the MaNDi instrument [164,165] at the Spallation Neutron Source (SNS) using all neutrons with wavelengths between 2-4 Å. During the collection of each diffraction pattern the crystal was held stationary and was rotated by 20° between successive diffraction patterns. The diffraction data was reduced using the Mantid [170] software and scaled and wavelength normalized using the Lauenorm [171] program from the Lauegen suite [172].

Table 4.1 Neutron Data Collection Statistics for Oxidized and Reduced Crystals

Oxidation state of Mn	Oxidized (3+)	Reduced (2+)
Diffraction source	MaNDi	MaNDi
Size (mm ³)	0.30	0.46
Wavelength(s) (Å)	2–4	2–4
Temperature (K)	293	293
Detector(s)	40 SNS Anger cameras	40 SNS Anger cameras
Crystal-to-detector distance (mm)	450	450
Rotation range per image (°)	0	0
No. of images collected	6	8
Total rotation range (°)	120	160
Exposure time per image	48 h	48 h
Space group	<i>P</i> 6 ₁ 22	<i>P</i> 6 ₁ 22
<i>a</i> , <i>b</i> , <i>c</i> (Å)	81.4, 81.4, 242.3	81.4, 81.4, 242.3
α , β , γ (°)	90, 90, 120	90, 90, 120
Resolution range (Å)	15.27–2.14 (2.22–2.14)	15.67–2.30 (2.38–2.30)
Total No. of reflections	68993	77229
No. of unique reflections	21386	20454
Completeness (%)	80.0 (69.3)	93.2 (93.6)
Multiplicity	3.23 (1.94)	3.78 (3.46)
$\langle I/\sigma(I) \rangle$	4.50 (2.70)	5.7 (4.10)
R_{merge} (%)	21.7 (28.2)	22.0 (22.8)
$R_{\text{p.i.m.}}$ (%)	10.1 (21.4)	11.4 (15.7)

4.3 Results and Discussion

4.3.1 Redox manipulation

To discover the optimal redox agent for manipulating the oxidation state of the manganese within crystals, a variety of agents, concentrations, and exposure methods were tested. Several redox agents and three manipulation methods were tested and their advantages and disadvantages are noted. Each agent and method had an appropriate use depending on the crystal size and stability as well as the susceptibility of the metal to redox changes (i.e. the redox potential) while maintaining adequate diffraction quality. In the case of MnSOD, the redox changes of the active site metal were detected by the change in intensity of the pink color of the crystals (Figure 4.1). A deep pink color is indicative of trivalent manganese ions whereas colorless crystals represent divalent manganese ions. [93,105].

Four redox agents were screened using small crystals ($<0.05 \text{ mm}^3$) grown in a 24-well plate by supplementing the agent into the reservoir solution and allowing it to interact with the crystals via vapor diffusion.

First, hydrogen peroxide is a known oxidizing agent, but in the case of its interaction with the manganese of MnSOD, it acts as a reducing agent when in excess by forcing the backwards reaction of the second half reaction [65]. This is not feasible with Cu or Fe containing proteins as hydrogen peroxide imposes Fenton chemistry with these transition metals. Concentrations above 1% hydrogen peroxide abolished diffraction without visible alterations to the crystals other than color while 0.1% was able to turn these small crystals colorless.

Second, sodium ascorbate, has been documented as a reducing agent for SODs in solution [166,173]. Signs of reduction were not detected with concentrations up to 0.85 M after one week of vapor diffusion or when soaking the crystals overnight. After 1 month, color changes were visible with concentrations of 0.85 M solely using vapor diffusion.

Third, sodium dithionite has been applied in earlier X-ray crystallographic studies of SOD using soaking methods [93,105] and has been shown to influence the absorption spectra of the MnSOD chromophore [166]. For the vapor diffusion screen, concentrations greater than 0.3 *M* would sporadically grow salt crystals within the reservoir, on the crystals, or within the crystals. For the small crystals of this screening method, 0.2 *M* was sufficient to turn the crystals colorless after 1 day.

Fourth, potassium permanganate has been shown to increase the absorption spectra of the oxidized MnSOD chromophore [166]. It was not observed to have ‘side effects’ on the crystals when using concentrations up to 7 *mM*, which easily increased the pink intensity of the samples. Higher concentrations were not used due to concern over unwanted long-term effects.

While the screening described above determined that redox manipulation of small MnSOD crystals was possible, the techniques needed to be translated to larger crystals (> 0.2 mm³) to perform neutron diffraction. The suitable redox agent concentrations discovered using the small-scale screen were used as a starting point to achieve redox manipulation of larger MnSOD crystals within capillaries. Finding the optimal concentrations for larger crystals in capillaries was more difficult owing to the large variability in crystals sizes as the amount of redox agent needed to change the redox state of the samples is proportional to the crystal volume. The distance between the reservoir slug and the crystal within a capillary also is a determinant in the potency of redox influence on the sample using vapor diffusion. Below, redox manipulation via vapor diffusion for neutron crystallography is addressed along with alternative methods for controlling the oxidation state of the active site manganese ion.

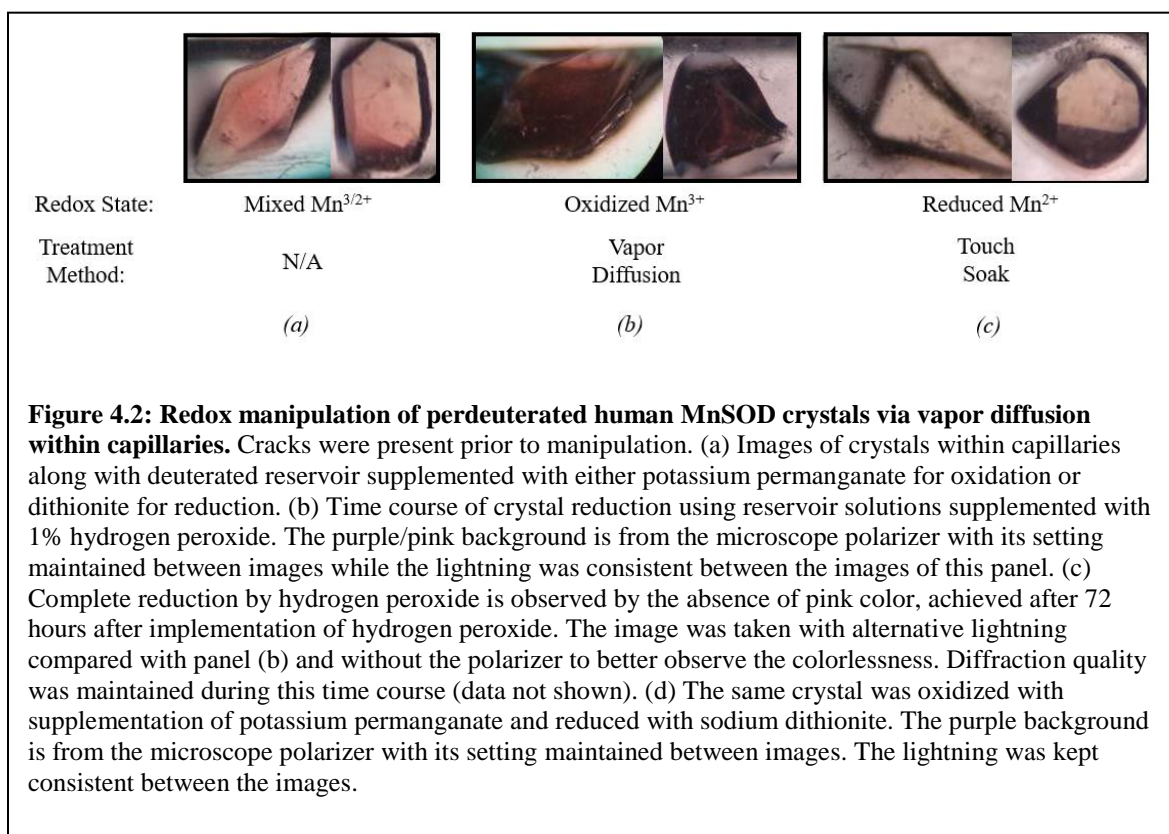
Vapor diffusion within a capillary is considered the least invasive method of redox manipulation with minimal amount of risk to crystal integrity as the crystal is not touched after it is mounted in a capillary. This technique involves simply adding the redox reagent to the deuterated substitute reservoir slugs in the capillary (**Figure 2a**), allowing vapor diffusion of both D₂O and the

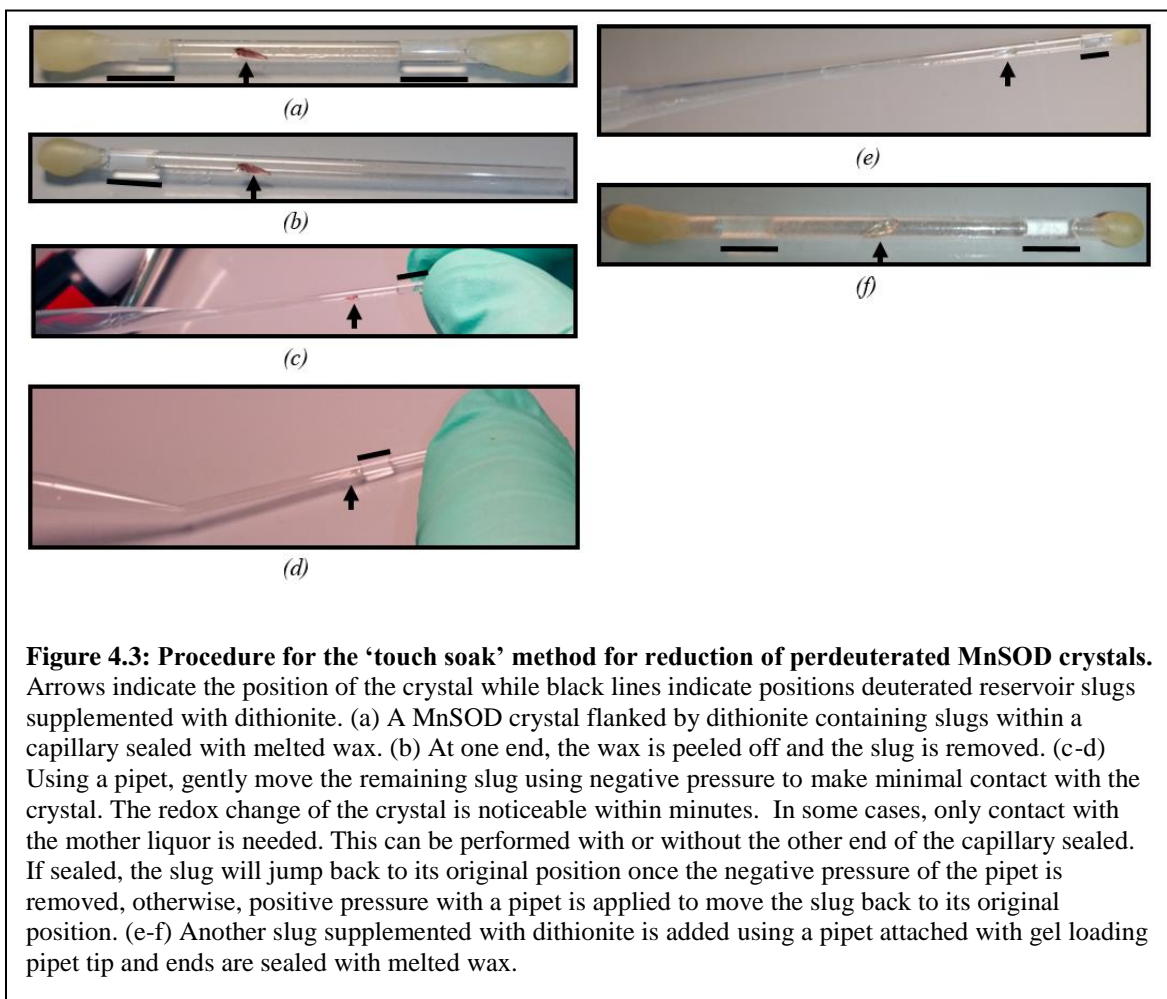
redox agent with the crystal. The speed of the redox change is proportional to the concentration of the redox agent in the reservoir slug and the distances of the slug(s) from the crystal. In general, a balance between these three elements should be considered. Redox and color changes can take between days and weeks depending on the parameters used. High amounts of a redox compound or close proximity between the slug and crystal increases the susceptibility of the sample to side effects. These include cracking of the crystal, salt or protein aggregates nucleating within the protein crystal, and/or deteriorating diffraction quality. Some crystals were more susceptible to these side effects than others when conditions are kept identical. This was probably due to differences in intrinsic quality of the crystals. The capillaries can be opened to replace the supplemented reservoir slugs with fresh ones every few days to speed up the process, but this also increases the likelihood of damaging the crystals due to handling. While vapor diffusion has the potential to be one of the least invasive techniques, one needs to compromise between time and risk when manipulating the samples.

The crystals were oxidized primarily through vapor diffusion due to the lack of apparent side effects from using 6.4 mM potassium permanganate, permitting liberal volumes of permanganate and close proximity between the slugs and the crystal (~3 cm). Potassium permanganate increased the pink color of the crystals over the course of one week (Figure 4.1b & 4.2a). During the vapor diffusion process, the pink color of the permanganate solution decreased, indicative of the decay of the oxidizing agent. Upon this observation, the capillaries were opened and the reservoir slugs were replaced with ones containing ‘fresh’ permanganate. After several replacements, the pink color of the solution stabilized within the sealed capillary and the crystals held the deep pink intensity over the course of several months, likely a consequence of saturation of the redox reaction. Subsequent neutron diffraction utilizing this method was achieved on MaNDi to 2.14 Å resolution (Table 4.1).

Reducing the manganese within the crystals using vapor diffusion was achieved but not without difficulties. Hydrogen peroxide concentrations ranging between 0.25 – 1.00 % were able to remove the pink intensity of the crystals in 1-3 d (Figure 4.2b-c), representative of divalent manganese ions within the sample, but at a consequence. The diffraction quality of these crystals seemed unaffected for ~2 wks, but was then rapidly abolished afterwards with no apparent changes to the visual quality of the samples. This may indicate saturation of the redox reaction between hydrogen peroxide and manganese and funnelling of hydrogen peroxide towards decomposing the protein by oxidizing reactions. The diffraction quality of a crystal could be compromised before the experiment is completed given the longer data collection times needed with neutrons. Even with this deleterious side effect, use of hydrogen peroxide as a reducing agent is feasible if data collection is performed within an adequate timeframe, such as with X-rays. Alternatively, hydrogen-peroxide soaked crystals could be cryotrapped for neutron data collection.

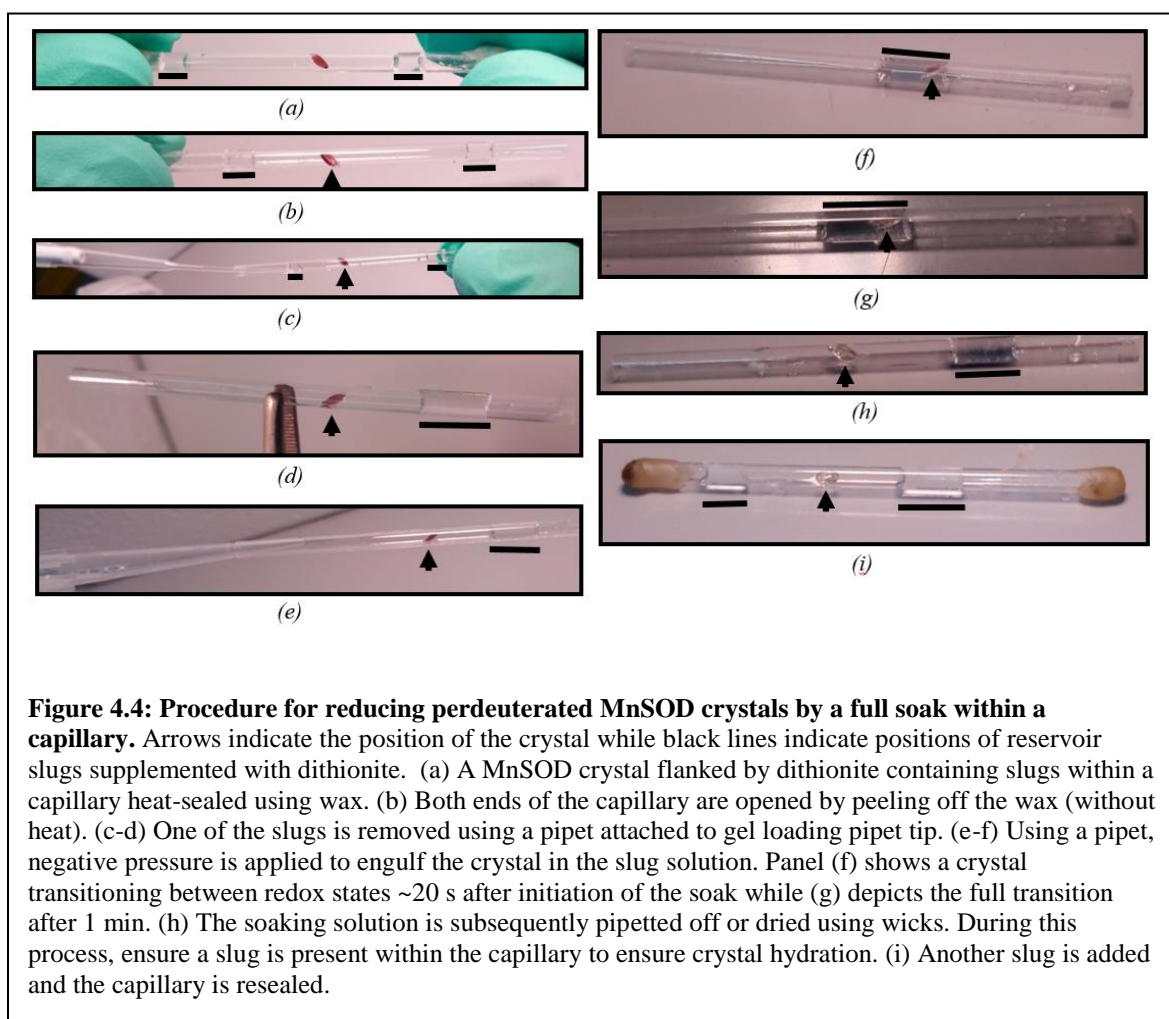
The advantage of vapor diffusion is the ability to chemically treat the crystals without direct contact, but its appeal diminishes when the higher concentrations of reagent used in the process still compromise the samples, such as with sodium dithionite. Another means to treat the samples is to lessen the concentration of the chemical agent in the reservoir slug and allow very little contact with the crystal, minimizing any potential damage to the sample. In the case of MnSOD, 0.2 *M* dithionite was able to reduce crystals with this approach, a concentration where aggregate growth was significantly less than at 0.3 *M*. This is achieved by cautiously using a pipet to move the redox agent supplemented reservoir slug within the capillary to barely create contact with the crystal (Figure 4.3). The slug is then pipetted away when the redox change is complete. The effects of the dithionite on the samples were noticeable within minutes, totally abolishing the intensity of the pink color of the crystals. In some cases, only contact with the mother liquor surrounding the crystal was needed. After redox treatment, the dithionite-supplemented reservoir slugs were replaced weekly to maintain a reducing environment within the capillary, as dithionite





decomposes in solution. This method also ensures a more extensive deuterium exchange between the crystal and the deuterated substitute reservoir than the vapor diffusion method. Neutron diffraction to a resolution where hydrogen positions could be observed was possible (Table 4.1). The advantages of this 'touch soak' method include use of a lower concentration of agent and rapid effects while difficulties can arise from the increased mosaicity and precision handling required.

MnSOD crystals that were larger in size, $> 0.4 \text{ mm}^3$, were resistant to redox changes through both vapor diffusion and touch soaking. The redox state of these crystals would revert to the native, mixed state over the course of several days. This is a consequence of the increased amounts of the metalloprotein contributing to the crystal size, requiring larger amounts of redox agent to shift the oxidation state of the crystal. In the case of sodium dithionite, increased concentrations ($> 0.3 \text{ M}$) for the vapor diffusion or touch soak method were not feasible due to the worsening of unfavorable effects on the samples. To keep the concentrations of the agent low and still achieve shifts in the oxidation state of the crystals without reversion, full soaks were performed within the capillaries. This consisted of gently engulfing the crystals with deuterated substitute reservoir slugs supplemented with 0.2 M sodium dithionite (Figure 4.4). Some samples cracked once drowned in redox solution though these were usually poor quality crystals but one must consider this risk, nonetheless. The pink intensity of the crystals faded within 1 min of soaking, after which the solution can be pipetted off and the crystal laid dry. Some crystals could be soaked in the dithionite solution for weeks and still maintain adequate diffraction quality. Once the crystals were laid dry, dithionite supplemented (0.2 M) reservoir slugs were placed in the capillary to maintain a reducing environment via vapor diffusion. After one week of the removal of the soaking solution, small aggregates were observed on the protein crystal (Figure 4.5a). These aggregates did not grow larger and did not seem to exacerbate diffraction quality. Reversion of the oxidation state was not observed after a month. Full soaks are advantageous in their ability to



ensure a redox shift of samples as well as promoting rapid deuterium exchange for neutron crystallography, though crystals are susceptible to cracking and may exhibit increased mosaicity.

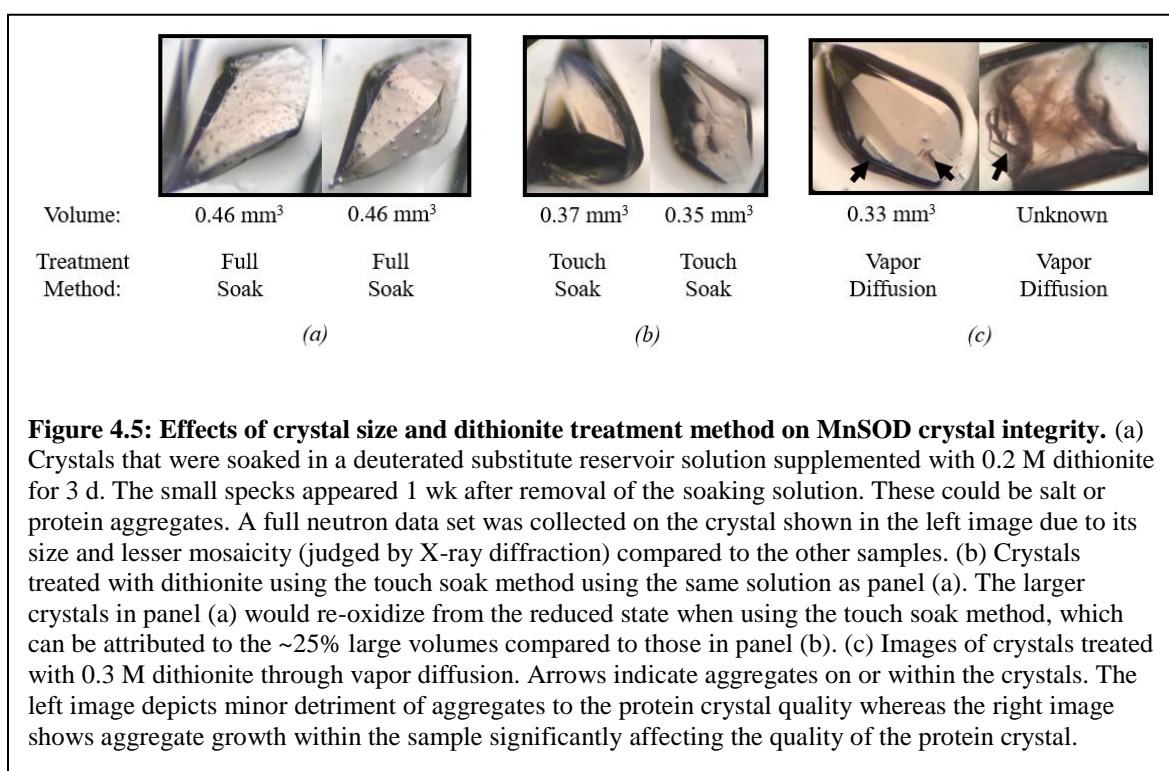
4.3.2 Optimizing Treatment Conditions and Determining Which Technique to Use

Discovering optimal conditions to treat large crystals intended for room temperature neutron diffraction has the potential to be a lengthy process. A brief workflow has been outlined to minimize the time required to find the appropriate treatment conditions for each of the three techniques. This proposed process assumes that the effects of treatment can be observed without diffraction, such as by eye or crystal absorption spectra, and that screening will be performed on large hydrogenated crystals.

(1) Find the minimum concentration of treatment agent (supplemented in substitute reservoir solution) needed to observe desired effects within minutes on samples upon a full soak. The rationale is that the concentration of treatment agent with full soaks is the least variant with crystal size as opposed to touch soaks or vapor diffusion. In addition, the change within a short timeframe is a rough indicator of whether the desired effects can be maintained with vapor diffusion in a sealed capillary after removal of the soaking solution. If the redox changes were immediate then relapse was less likely.

(2) A compatible concentration of treatment agent for touch soaking will likely be very similar to the concentration used for full soaks. Similar to the full soak, touch soaking should yield the desired effects within minutes. Touch soaking is more susceptible to reversion of the desired state due to its less rigorous nature and may require increased concentrations of agent compared to that of the full soak. The size of the crystals may also be another determinant, where smaller crystals may require lesser amounts of the treatment agent to obtain the desired effects.

(3) Vapor diffusion will require a higher concentration of treatment agent to observe changes within days/weeks compared to touch and full soak methods to compensate for its less



invasive nature. The concentrations of agent discovered from full and touch soak screens serves as a rough starting point for vapor diffusion screens, with up to 50% increases needed. Alternative ways to increase the speed of crystal changes from treatment is to decrease the amount of distance between the agent-containing slug and the sample as well as replacing the slug with freshly made agent-containing solution periodically.

4.3.3 Feasibility for Neutron Diffraction

One intent of this work was to gauge the feasibility of collecting neutron data of redox-treated, large, perdeuterated MnSOD crystals to a resolution where the positions of hydrogen atoms are observed. The possibility of this was unclear given the large unit cell dimensions of the MnSOD crystal form, which crowds diffraction spots, and the tendency for chemical crystal treatments to decrease diffraction quality, particularly through exacerbating spot crowding. Too much spot overlap ultimately reduces the resolution of the data. Neutron data sets were collected on crystals where manganese ions were manipulated to the trivalent state ('oxidized') or the divalent state ('reduced') (Table 4.1). The higher R_{merge} values than what would be expected for monochromatic X-ray data are comparable to other Laue data sets collected from neutron spallation sources [174].

Collecting data on oxidized perdeuterated MnSOD crystals did not bring any additional difficulties to those already inherent to neutron crystallography. The crystal from which data was collected was 0.3 mm³ in size and oxidized by vapor diffusion of potassium permanganate implemented into the deuterated substitute reservoir slug (Figure 4.2a, left box). Neutron data was collected and processed to 2.14 Å and is the highest resolution obtained for this crystal system.

For data collection of a reduced sample, a crystal 0.46 mm³ in size soaked in dithionite for 3 days was chosen (Figure 4.5a, left image). One week after removal of the soaking solution, small aggregates were observed on the protein crystal. These aggregates did not grow larger and did not seem to exacerbate diffraction quality. Before data collection, the slugs within the capillary

containing the sample were replaced with fresh dithionite supplemented deuterated reservoir solution. After collecting data for 16 d, the crystal maintained its redox state (i.e. colorlessness). The diffraction data was strong, with a diffraction limit of ~ 2.0 Å resolution, attributed to the size and perdeuterated qualities of the sample. Despite the extent of diffraction, the quality of the data was hampered by spot overlap at higher resolutions. This is inherently an issue because of the unit cell dimensions but was further exacerbated by the increased mosaicity from dithionite treatment, increasing the size of the Bragg reflections. From the corresponding X-ray data, the mosaicity of this crystal was 0.49° compared to the 0.26° of the oxidized crystal. Consequently, the resolution had to be cut to 2.30 Å during processing, which is still sufficient to identify hydrogen positions.

As a comparison, our previous work that details neutron data collection on a perdeuterated MnSOD crystal that was not redox manipulated [163]. This crystal was 0.26 mm^3 in volume and was collected and processed to 2.30 Å resolution. While this untreated crystal was of smaller size compared to the treated counterparts reported, it is apparent the redox manipulation methods discussed here do not significantly impair the resolution in which neutron data can be collected and processed.

4.4 Conclusions

4.4.1 Mechanism of Interaction Between Redox Agents and MnSOD Crystals

Both the size and charge of the redox agents allow an interaction with the active site manganese ion of MnSOD. The ~ 5 Å opening of the active site channel of MnSOD is large enough to accommodate both permanganate and dithionite entering and interacting with the manganese [82,175,176]. Both of these molecules are negatively charged and are likely guided to the active site by the same positive electrostatic surfaces of MnSOD that promote productive diffusion of anionic superoxide for its catalysis [82]. For the negatively-charged ascorbate, redox changes were absorbed at a much slower rate. This could be attributed to its bulkier size compared to the other agents tested. The size of ascorbate only permits it to enter the active site in specific orientations.

Nevertheless, a near direct interaction between redox agents and the active site manganese ion is possible.

The redox state can be influenced without any direct contact between the agent and the sample via vapor diffusion, indicating that permanganate, dithionite, hydrogen peroxide, and ascorbate can all diffuse through the capillary as a gas. The means by which this occurs is unclear. Diffusive water molecules could hydrate the redox agents and the evaporative hydration complex may be capable of traveling through the capillary. Nevertheless, redox agents that do not make contact with crystals within capillaries do exert observable effects (Figure 4.2).

4.4.2 Hydrogen Peroxide as a Reducing Agent and Substrate

MnSOD is unique compared to FeSOD and CuZnSOD in that the active site metal can be reduced by excessive amounts of hydrogen peroxide. MnSOD exhibits reversible product inhibition by hydrogen peroxide, which is not observed by the other SODs due to the susceptibility of Fenton chemistry by Fe and Cu. Addition of copious amounts of hydrogen peroxide to MnSOD instigates the formation of a product-inhibited complex, which can only form when Mn is in the trivalent state [104]. Subsequently, the presence of the Mn^{3+} -peroxo complex decays in conjunction with formation of Mn^{2+} SOD. This phenomenon is explained by Hearn and colleagues [65], where ample amounts of hydrogen peroxide first bind as the inhibited complex and then force the backwards reaction to produce superoxide in tandem with an electron reduction of Mn^{3+} to Mn^{2+} . The generated superoxide then can interact with a Mn^{3+} ion to instigate the forward reaction with an electron reduction to yield diatomic oxygen (O_2) and Mn^{2+} . Hydrogen peroxide is thought to be incapable of binding to Mn^{2+} due to steric hindrance of the water molecule ligated to the manganese [104]. The water molecule is deprotonated to hydroxide in the Mn^{3+} state, which accommodates space for hydrogen peroxide to bind. The generated superoxide is capable of interacting with Mn^{2+} to oxidize the cation to a trivalent (Mn^{3+}) state, but the excessive amounts of hydrogen peroxide and its cascade of reactions yields Mn^{2+} as the dominant species.

The attribute of hydrogen peroxide acting both as an inhibitor and a reducing agent explains why hydrogen peroxide soaked structures of MnSOD may not reveal peroxide at the active site. This is exemplified by two hydrogen peroxide soaked *E. coli* MnSOD structures. One soaked with 0.4% hydrogen peroxide does not reveal peroxide at the active site (PDB code 1IXB, unpublished) while another soaked using 0.008% does (PDB code 3K9S) [108]. The former contains divalent manganese ions based on QM/MM calculations [161] whereas the redox state of the latter cannot be discriminated due to the peroxide being observed with partial occupancy. The amounts of hydrogen peroxide used in these soaks may determine whether a backwards reaction is forced or only binding to form a product-inhibited complex occurs.

The slow decay of crystal diffraction quality as a result of hydrogen peroxide treatment may be a consequence of oxidative damage. Hydrogen peroxide is known to react with amino acids cysteine, methionine, lysine, histidine, and glycine [177]. Flash-freezing to cryogenic temperatures has been shown to circumvent this deleterious effect [108,161] for X-ray crystallography. Cryo-cooling is notoriously difficult for large crystals needed for neutron crystallography but is possible [178,179]. Cryogenic neutron crystallography has the potential to be amenable for large MnSOD due to the built-in Oxford Cryosystems Cobra cryostream at the MaNDi beamline, which is capable for temperatures between 80-200 K [165,180].

4.4.3 Future Directions

Neutron data is normally refined with a X-ray data set from the same crystal or another mimicking the growth and treatment conditions of the original [181]. This is because neutron and X-ray data result in different but complementary information. X-ray structures are typically of higher resolution, which can be used to derive restraints for refining neutron data. However, this poses an issue for crystal structures intended to be fully oxidized, as X-ray exposure reduces the metal of metalloproteins while neutrons do not [75]. To circumvent this issue, restraints/data from the X-ray set need to be omitted for the area of the molecule that will be influenced by redox

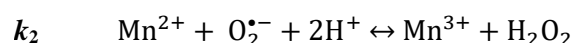
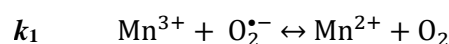
changes. For example, the active site metal ion and its ligated amino acids as well as any neighboring residues should not incorporate X-ray data during refinement. An alternative for restraining these active site molecules is to input custom restraints derived from quantum mechanical/molecular mechanics (QM/MM) or density function theory (DFT) calculations. In the case of MnSOD, DFT calculations for the oxidized human form are published [90].

Chapter 5: Neutron Structures of Oxidized and Reduced MnSOD

5.1 Introduction

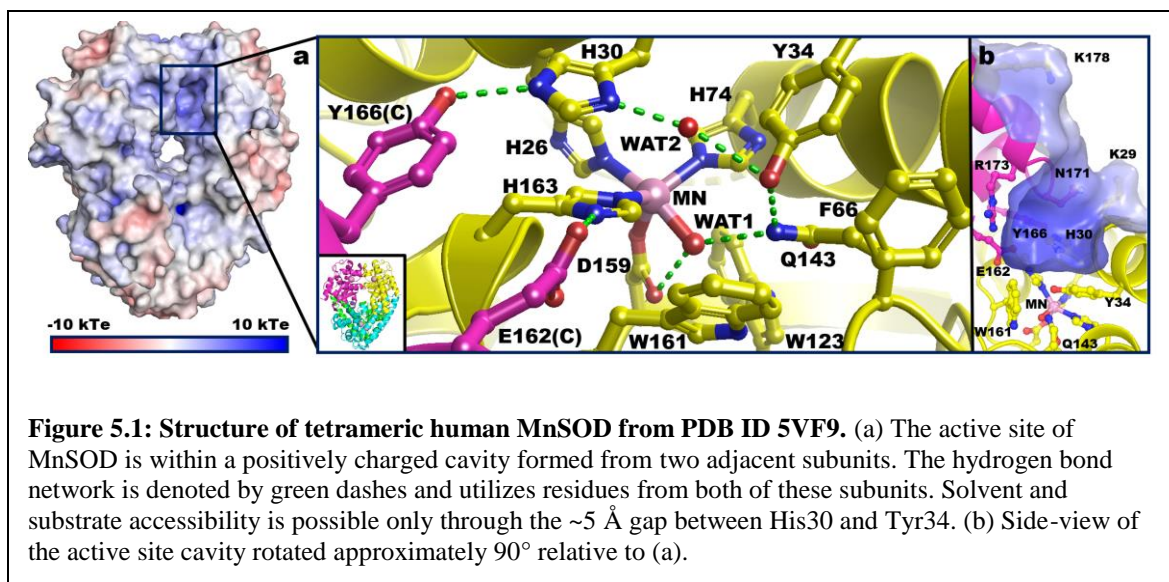
Oxidoreductases are a large class of enzymes that use unpaired electrons to facilitate redox reactions with other chemical species and are involved in nearly all aspects of life. The electron transfers performed by oxidoreductases are almost always coupled with a proton transfer [66]. Concerted proton and electron transfer (CPET) permits a thermodynamically favorable redox reaction that avoids ionized intermediates, is extremely efficient, and is an integral part of enzymes with the highest catalytic rates [67-69]. Particularly noteworthy is the prominence of CPET enzymes that regulate the concentration of reactive oxygen species (ROS) in the cell. ROS levels are central to programmed cell death and abnormal regulation by these oxidoreductases play significant roles in cancer and cardiovascular diseases [182]. CPETs are therefore of significant interest to study but a mechanistic understanding of these enzymes is still lacking. Deciphering these fundamental biochemical reactions is not only significant for its role in diseases, but for the biomedical design of CPET-dependent therapeutic interventions, irradiation protectants, and electrochemical biosensors [183,184].

Human MnSOD is a CPET-based oxidoreductase found in the mitochondrial matrix that reduces ROS levels by eliminating $O_2^{\bullet-}$ with the unpaired electrons of the active site metal. The Mn is coordinated to inner-sphere residues His26, His74, His163, Asp159, and a single-oxygen species that could be either H_2O or OH^- (designated WAT1, Figure. 5.1). Trivalent Mn oxidizes $O_2^{\bullet-}$ to O_2 ($k_1 = 1.5 \text{ nM}^{-1}\text{s}^{-1}$) [73] and the resulting divalent Mn reduces another $O_2^{\bullet-}$ molecule to H_2O_2 ($k_2 = 1.1 \text{ nM}^{-1}\text{s}^{-1}$) [73]. This is the only means the mitochondrial matrix has to keep $O_2^{\bullet-}$ levels low enough to avoid damage to macromolecules and destruction of cellular function [2].



The major endogenous source of $O_2^{\cdot -}$ is from electrons inadvertently leaking from the electron transport chain. Dysfunctional MnSOD activity, therefore, poses significant consequences on the mitochondria that contributes to several diseases. Genetic aberrations of MnSOD are associated with several cancer types, with mammary and prostate cancers being the most frequently noted in curated databases [185]. Polymorphisms of MnSOD have also been noted to be a predictor for deficient vascular function [186]. Therefore, the ability for MnSOD to utilize the high reaction rate and efficiency ($k_{cat}/K_m > \sim 10^9 \text{ M}^{-1}\text{s}^{-1}$) of its CPET mechanism is correlated with the preservation of health [73].

The CPET mechanism of MnSOD and the majority of other oxidoreductases has yet to be defined at the atomic level. The limitation in studying CPETs is the difficulty in directly detecting the protonation states of ionizable residues, solvent and ligands at the active site and correlating them with the electronic state of the active site metal. The second-sphere of MnSOD harbors five residues (His30, Tyr34, Gln143, Glu162, and Tyr166 (Figure 5.1)) and information about their protonation states would be of significant value in deciphering a catalytic mechanism. X-ray and spectroscopic techniques have been unable to provide this information due to the poor scattering of hydrogen atoms and the difficulty in discerning spectra for specific titratable positions. Neutron protein crystallography (NPC) is an emerging tool for analyzing hydrogen positions of biological macromolecules and possesses attributes that are especially useful in deciphering CPET mechanisms. In NPC, scattering of deuterium is on par with carbon, nitrogen, and oxygen, significantly increasing the ability to locate proton positions for the entire enzyme. An additional advantage is that NPC does not alter the electronic state of the metal unlike X-rays [120]. Here, we present room temperature neutron structures of human MnSOD at physiological pH in Mn^{3+} and Mn^{2+} and reveal how the atomic locations of all protons in the enzyme active site exchange when the active site metal goes through a redox cycle. To our knowledge, this study provides the first direct experimental evidence of a CPET enzymatic mechanism.



5.2 Materials and methods

5.2.1 Perdeuterated expression, purification, and crystallization

Detailed methods for recombinant MnSOD deuterated expression at ORNL biodeuteration lab, purification, and crystallization have been described previously [163]. Of note, expression was performed at 37 °C instead of the 30 °C in the citation, as this significantly increases Mn metal incorporation of MnSOD [187]. Purification and crystallization were performed with hydrogenated reagents. Deuterium exchange of crystals was performed by vapor diffusion in capillaries.

5.2.2 Redox manipulation of perdeuterated MnSOD crystals

Methods for manipulating the Mn metal of MnSOD to either Mn^{3+} or Mn^{2+} have been described previously [188]. In brief, a crystal in a quartz capillary was soaked in deuterated reservoir solutions containing either 6.4 mM potassium permanganate (KMnO_4) to achieve the Mn^{3+} state or 300 mM sodium hydrosulfite ($\text{Na}_2\text{S}_2\text{O}_4$) to achieve the Mn^{2+} state. After drying the crystal from soaking solutions, the crystal was flanked in the capillary by slugs of the deuterated reservoir soaking solutions. Fortuitously, the decomposition products of the redox agents are unable to enter the active site of MnSOD [188].

5.2.3 Neutron and X-ray data collection

Data collection was preceded by the replacement of the deuterated and redox-agent containing reservoir slugs with fresh equivalents. Time-of-flight wavelength-resolved neutron Laue diffraction data were used to collect data from the 0.46 mm^3 perdeuterated crystal using the MaNDi instrument [164,165] at the ORNL SNS using all neutrons with wavelengths between 2-4 Å. Data collection of each diffraction pattern was from the crystal held in a stationary position, with successive diffraction patterns being collected after 20° rotations along the Φ axis. A KMnO_4 -treated perdeuterated crystal of 0.46 mm^3 in volume at 296K was recorded to 2.20 Å resolution for the Mn^{3+}SOD form and subsequently treated with $\text{Na}_2\text{S}_2\text{O}_4$ to achieve the Mn^{2+}SOD state where 2.30 Å data were collected (Table 5.1). $\text{Na}_2\text{S}_2\text{O}_4$ is noted to deteriorate diffraction quality and was

observed to increase the c unit cell axis by ~ 1 Å [188]. After neutron data were collected from the crystal in the Mn^{2+}SOD state, X-ray diffraction data were collected at 296 K to 2.16 Å resolution using a Rigaku FR-E SuperBright home source. After room-temperature data collection, the crystal was not diffraction viable for Mn^{3+}SOD data collection and a sister crystal grown from the same well was used instead for obtaining X-ray data to 1.87 Å resolution.

5.2.4 Data processing and refinement

Neutron data were integrated using *MANTID* [189]. Integrated neutron data were scaled and wavelength-normalized using *LAUENORM* from the *LAUGEN* suite [171]. X-ray diffraction data were reduced using *HKL-3000* for indexing, integration, and scaling [124]. The refinement of both X-ray and neutron models was completed with *PHENIX.REFINE* from the *PHENIX* suite [190].

The X-ray model was first refined against its corresponding data set and subsequently used as the starting model for neutron refinement. X-ray refinement was performed by removal of all non-protein entities in the starting model of 5VF9 [82], simple molecular replacement through rigid-body refinement, and subsequent restrained-positional refinement. With *COOT* [126], protein was manually fit into $|F_o|-|F_c|$ peaks as needed and refined first. New solvent structure and Mn atoms were manually modelled into $|F_o|-|F_c|$ density. Torsional backbone angle restraints were derived from the X-ray model and applied to neutron refinement using a geometric target function with *PHENIX.REFINE* [190]. As D atoms were manually added during iterations of neutron refinement, the stereochemistry weight scale was manually adjusted due to the increase of atoms at stereochemically sensitive positions. The neutron refinement process was performed to model the D atoms of the active site last to limit phase bias. For the initial rounds of refinement to fit protein structure, only non-exchangeable D atoms (which have stereochemically predictable positions) were present. Afterwards, each individual exchangeable position outside the active site was inspected for residual $|F_o|-|F_c|$ nuclear density and modeled with D atoms appropriately before more

Table 5.1. Data collection and refinement statistics

Data Collection Statistics				
	Neutron		X-ray	
	Oxidized	Reduced	Oxidized	Reduced
Diffraction Source	MaNDi		Rigaku FR-E	SuperBright
Temperature (K)	296			
Space group	$P6_122$			
a, b, c (Å)	81.30, 81.30, 241.840	81.33, 81.33, 242.880	81.14, 81.14, 241.63	81.13, 81.13, 242.12
α, β, γ (°)	90, 90, 120			
Wavelengths (Å)	2-4		1.5418	
Exposure time	48 h	48 h	60 s	60 s
No. of unique reflections	24556	21719	31815	25718
Resolution range (Å)	14.64-2.20 (2.28-2.20)	14.65-2.30 (2.38-2.30)	50.00-2.02 (2.07-2.02)	50.00-2.16 (2.20-2.16)
Multiplicity	8.0 (6.1)	7.2 (5.7)	7.8 (3.5)	7.6 (4.1)
$I/\sigma(I)$	7.0 (3.40)	6.2 (3.3)	8.3 (2.0)	4.8 (2.0)
R_{merge}	0.284 (0.314)	0.277 (0.294)	-	-
R_{meas}	-	-	0.291 (0.610)	.459 (.683)
$CC_{1/2}$	0.935 (0.275)	0.943 (0.319)	0.950 (0.730)	0.804 (0.638)
R_{pim}	0.101 (0.129)	0.102 (0.124)	0.082 (0.320)	0.140 (0.326)
Data completeness (%)	98.83 (98.83)	98.94 (99.16)	100.0 (100.0)	97.5 (95.5)
Refinement Statistics				
R_{work}	0.2531	0.2662	0.2166	0.2195
R_{free}	0.2832	0.3038	0.2517	0.2636

iterations of refinement. Next, the O atoms of solvent molecules were first modelled manually outside the active site and refined to determine whether to model solvent as O, OD, or DOD using residual $|F_o| - |F_c|$ nuclear density. The omit density peaks were also used to discern the appropriate orientation of the solvent molecules. After refinement of the solvent structure outside the active site, non-D atoms of the active site were modelled, including Mn and the O of solvent. Loose Mn-coordination restraints were derived from the Mn²⁺SOD X-ray structure and applied to the Mn²⁺SOD neutron model, whereas the Mn³⁺SOD neutron model used restraints derived from our own DFT calculations. In both cases, the R-free value was improved with the application of these restraints. Last, D atoms of the active site were modeled and refined manually.

5.2.5 Computational Details

All quantum mechanical (QM) DFT calculations were performed with the NWChem 6.8 software utilizing extra fine integration grid quadrature shown to provide high precision with restricted open-shell John-Sham (ROKS) treatment [191-193]. The geometry optimizations implemented the B3LYP exchange-correlation functional dispersion corrected according to Becke and Johnson damping (DFT-D3-BJ) [194,195]. Optimizations were first performed in the gas phase until electron density converged to an energy difference of < 0.0627 kcal/mol between macro-iterations. The COSMO solvation model for real solvents was then implemented into the geometry optimizations to model the solution phase until an energy difference of < 0.31375 kcal/mol was reached between macro-iterations [196]. A less strict threshold was used for the solution phase due to its significant increase in computational load. There was no notable difference when optimizations began directly in the solution phase other than longer computational times. The def2-TZVPD basis set was used for the Mn ion whereas the 6-31+G(d,p) Pople basis set was specifically used for all other atoms due to its use in predicting pK_as under the B3LYP functional [197,198]. In accordance with other works, there was no significant benefit to using a larger Pople basis set. Likewise, a test using the relatively expensive def2-TZVPD basis set for all atoms yielded differing

free energies compared to the 6-31+G(d,p) basis set though harbored very similar ΔG_{aq}^* values which were used as the working terms for pK_a calculations described below. The QM models utilized for DFT calculations encompassed the active site residues that had the O and N atoms of the peptide backbone truncated and the C $^\alpha$ fixed. Additional fixed restraints were placed on aromatic residues found on the periphery of the active site (Phe66, Trp123, Trp166, and Tyr166) to mimic the packing found in the native enzyme. Otherwise, the atoms were free to move during geometry optimization. The nearest three water molecules found in the neutron structure counterparts, representative of the ordered solvent found at the active site, were included in the QM models in addition to the Mn-ligated solvent. The Mn ion used the high-spin quintet and sextet states for trivalent and divalent systems, respectively, in accordance with experimental observations [199].

5.2.6 Bonding orbital analysis

The JANPA software package was used to calculate Chemist's Localized Property-optimized Orbitals (CLPOs) from open-shell DFT geometry optimizations [200-203]. These are bonding and antibonding orbitals with maximum electron density computed through a series of localized basis set transformations. CLPOs are calculated with the same target quantity as Natural Bond Orbital (NBO) methods but make use of differing theory and yield highly comparable results [204-206]. The electron delocalization stabilization/destabilization energies utilized second-order perturbation theory analysis of the Fock matrix defined by the NBO methods [207] but were done in the CLPO basis of JANPA. The energy associated with electron delocalization from lone pair or bonding orbital i to antibonding orbital j is defined as

$$\Delta E_{i \rightarrow j}^2 = -q_i \frac{\langle i | \hat{F} | j \rangle^2}{\langle j | \hat{F} | j \rangle - \langle i | \hat{F} | i \rangle}$$

where q_i is the donor orbital occupancy and \hat{F} is the effective orbital Hamiltonian [207]. Values $\langle j|\hat{F}|j\rangle$ and $\langle i|\hat{F}|i\rangle$ are diagonal CLPO Fock matrix elements indicative of orbital energies and $\langle i|\hat{F}|j\rangle$ is the off-diagonal matrix element representative of perturbation.

5.3 Results and discussion

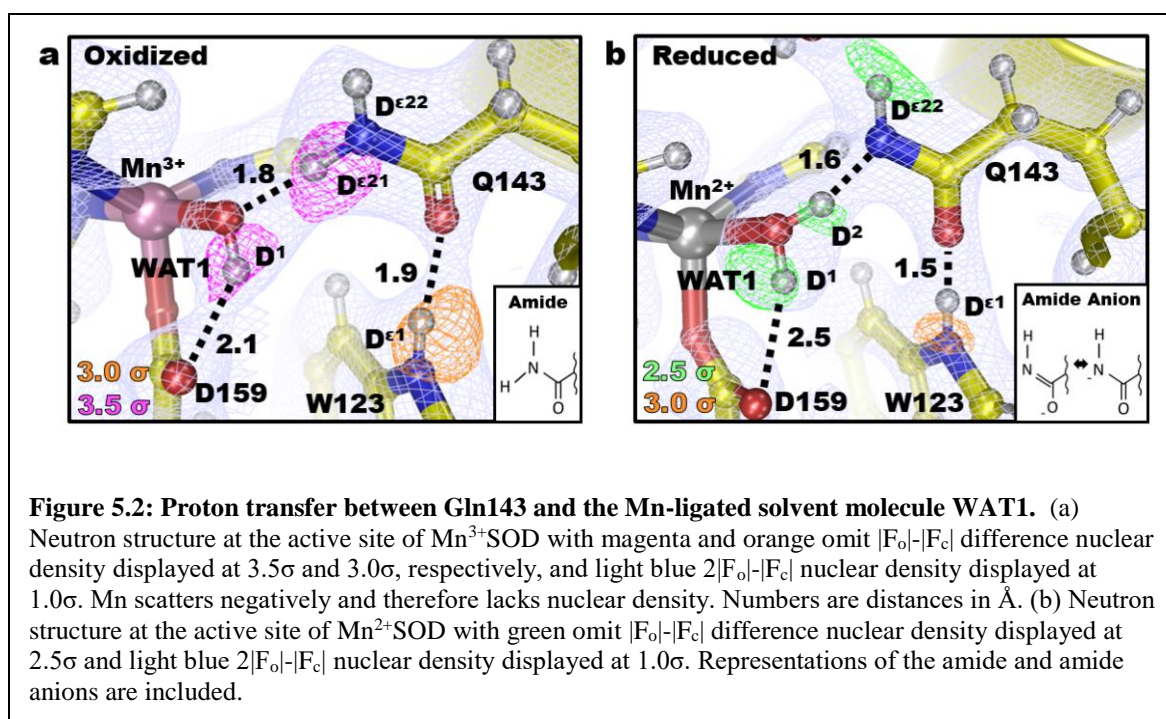
5.3.1 Direct evidence for CPETs at the active site metal with a previously unobserved and unusual glutamine deprotonation

To visualize the effect of the electronic state of the metal on the active site protons, all-atom D-labeled neutron structures were obtained for Mn^{3+}SOD and Mn^{2+}SOD to resolutions of 2.20 and 2.30 Å, respectively. The two data sets collected were from the same crystal treated with appropriate oxidizing and reducing chemicals and the redox conditions were maintained during each data collection [188]. Neutron data at these resolutions is excellent and permitted ease in the visualization of deuterium atoms. The proton structure of the two active sites without O_2^- were specifically sought to define the effects of metal redox state independent of substrate binding. We initially sought a crystallographic “check” for the success of the redox manipulations. WAT1 has historically been thought to obtain a proton ($^-\text{OH} \rightarrow \text{HOH}$) upon one-electron reduction of Mn^{3+} to Mn^{2+} for a CPET reaction but had not yet been directly observed and confirmed [69,93,104,106,107,158,161,208,209]. Indeed, careful inspection of the nuclear density between both neutron data sets suggested differential protonation of the WAT1 Mn-ligand dependent on the redox state of the Mn (Figure 5.2a-b). This was theoretically expected, verified our methods, and gave confidence in the data. To our knowledge, this is the first time the chemical reduction of the metal was visually observed to change the protonation state of an active site ligand.

For Mn^{3+}SOD , a single nuclear $|F_o|-|F_c|$ density peak for the D^1 atom of WAT1 is seen suggesting the expected deuterioxide (^-OD) molecule and is supported by the Mn-O(WAT1) distance of 1.8 Å [90,210]. The ^-OD acts as a hydrogen bond donor to the $\text{O}^{\epsilon 2}$ of Asp159 with a

distance of 2.1 Å whereas the O(WAT1) atom is acting as a hydrogen bond acceptor from D^{ε21}(Gln143) with a distance of 1.8 Å (Figure 5.2a). The data for WAT1 of Mn²⁺SOD instead has two nuclear $|F_o|-|F_c|$ density peaks for D atoms indicating the ⁻OD was converted to D₂O upon metal reduction, as expected. Further support suggesting a D₂O molecule is seen with the Mn-O(WAT1) distance of 2.2 Å [90,210]. The D¹(WAT1) atom position is similar to that found in the Mn³⁺SOD counterpart and hydrogen bonds with O^{ε2} of Asp159, albeit at a weaker interaction of 2.5 Å distance (Figure 5.2b). Surprisingly, D²(WAT1) points toward Gln143 suggesting the WAT1 of Mn²⁺SOD is acting as a hydrogen bond donor to Gln143. This means Gln143 is a hydrogen bond acceptor in Mn²⁺SOD and its D^{ε21} atom is absent. Indeed, there is a lack of nuclear density for D^{ε21} but not for D^{ε22}. This interpretation was supported when attempts to model D^{ε21} led to negative $|F_o|-|F_c|$ nuclear density. In the Mn²⁺SOD structure the hydrogen bond between D²(WAT1) and N^{ε2}(Gln143) is atypical with a bond distance of only 1.6 Å and O(WAT1)-D²(WAT1)-N^{ε2}(Gln143) angle close to 180°. These are characteristics of a short-strong hydrogen bond (SSHB), a type of hydrogen bond that is thought to stabilize particular enzymatic steps and enhance catalytic rates [211-213]. SSHBs are noteworthy in several well-studied enzymes, such as α-chymotrypsin that utilizes a SSHB between the His and Asp of its catalytic triad [212]. This creates a ~7 kcal/mol stronger interaction to substantially increase the kinetic rate. For Mn²⁺SOD, the SSHB between WAT1 and Gln143 may contribute to the stability of the unusual redox state and the high catalytic efficiency of the enzyme.

The experimental data, therefore, suggest that Gln143 is undergoing deprotonation to form an amide anion and is especially unusual because glutamine residues are not expected to act as weak acids since the pK_a of primary amides are 16 ~ 18. However, pK_a studies of less acidic secondary amides suggest pK_a values may be depressed to 7 ~ 8 depending on how the amide group is polarized (i.e. charge delocalization) [214]. This is supported by the known event of proton exchanges occurring at the amide groups of protein backbones. Moreover, several enzyme



studies suggest glutamine or asparagine-mediated proton transfers for catalysis and support the plausibility of a Gln143 \rightarrow WAT1 proton transfer. For example, an asparagine residue has been suggested to be deprotonated in prenyltransferases due to significant polarization from close proximity to a metal cation [215]. Nakamura and colleagues suggest their neutron diffraction data of cellulase Cel45A from *Phanerochaete chrysosporium* reveal proton donation and abstraction at Asn92 via amide-imidic tautomerization that is thought to be instrumental for the proton relay of the enzyme [216]. Infrared spectroscopy and computational calculations support the involvement of glutamine-mediated proton transfers in GTP hydrolysis by Ras-GAP and photoexcitation of photoreceptor proteins with the flavin-binding BLUF domain [217]. For MnSOD, the deprotonation of Gln143 for CPET to the active site ligand has not been observed before although it does explain the extremely high efficiency of the enzyme as a result of this internal proton source.

Density functional theory (DFT) quantum calculations of the active site using a system derived from the neutron structural data (inclusive of residues in Figure 5.1) support our interpretation of the nuclear density for deprotonation of Gln143. Chemist's localized property-optimized orbital (CLPO) analysis (highly akin to Natural Bond Orbitals [200,204,205]) was used to evaluate the interactions of Gln143 and WAT1 [201]. Reduction of Mn^{3+} to Mn^{2+} increases the electronegative character of the O(WAT1) lone pair facing the proximal amide proton of Gln143 (green atom, Figure 5.3a). This polarization of $^-\text{OH}(\text{WAT1})$ consequentially increases its basicity to the extent of abstracting a proton from the glutamine amide. In this way, a hard acid-hard base interaction ($\text{Mn}^{3+}\text{-}^-\text{OH}$) has become a soft acid-soft base ($\text{Mn}^{2+}\text{-OH}_2$) interaction. The bonds of the deprotonated amide reorganize to stabilize its new negatively-charged state (Figure 5.3b). The $\text{O}^{\epsilon 1}$ atom of Gln143 bears the most electronegative charge as CLPO calculations suggest less covalent electrons for the $\text{O}^{\epsilon 1}\text{-C}^{\epsilon 1}$ bond compared to that of $\text{N}^{\epsilon 2}\text{-C}^{\epsilon 1}$, with bond orders of 1.33 and 1.52, respectively (Table 5.2). The presence of a SSHB is supported as well since the new $\text{N}^{\epsilon 2}$ still has

covalent character with the donated proton (Figure 5.3c). Donor-acceptor orbital analysis from CLPOs indicate electron character is transferred from the $N^{\epsilon 2}$ lone pair orbital to the σ^* -antibonding orbital of O-H(WAT1) and is a 1.4 kcal/mol stabilizing hyperconjugation interaction (Table 5.3). As a result, the interaction between $N^{\epsilon 2}$ and the donated proton demonstrates partial σ -bonding character. The extent of covalence is 36% for the $N^{\epsilon 2}$ -H bond and 64% for O-H bond (Table 5.4). Altogether, quantum calculations support both Gln143 deprotonation and the presence of an unusual hydrogen bond between WAT1 and Gln143.

An unusual and previously undetected change in the interaction of Gln143 with the neighboring Trp123 was observed. A SSHB of 1.5 Å is seen between the $O^{\epsilon 1}$ of Gln143 and $N^{\epsilon 1}$ of Trp123 (Figure 5.2b). The same hydrogen bond is seen in Mn^{3+} SOD at a distance of 1.9 Å (Figure 5.2a). The neutron data, therefore, support the notion that $O^{\epsilon 1}$ (Gln143) harbors stronger electronegative character during the Mn^{2+} redox state. This may be a consequence of Gln143 deprotonation to the amide anion during the $Mn^{3+} \rightarrow Mn^{2+}$ redox reaction and negative charge stabilization through hydrogen bonding with Trp123. Charge stabilization is likely to be important for glutamine deprotonation as amide groups are known to deprotonate at neutral pH when electronegatively polarized at the carbonyl O atom [214]. Trp123 is especially competent at charge stabilization due to its own ability to polarize. CLPOs suggest that lone pair electrons of $N^{\epsilon 1}$ (Trp123) delocalize into the highly-conjugated aromatic ring of Trp123 when the glutamine amide is deprotonated (Figure 5.3e). Donor-acceptor analysis calculate the donation of $N^{\epsilon 1}$ (Trp123) lone pair electronic character into adjacent π^* -antibonding orbitals (Figure 5.3f) as a 20.9 kcal/mol stabilization interaction (Table 5.3). This also permits the observation of close hydrogen bond interaction between $O^{\epsilon 1}$ (Gln143) and $H^{\epsilon 1}$ (Trp123). Quantum calculations indicate an important role for Trp123 in the deprotonation of Gln143.

If an $O(WAT1)-D^{\epsilon 21}(Gln143)-N^{\epsilon 2}(Gln143)$ interaction is needed for redox cycling of Mn, mutation of Gln143 or a nearby residue that may stabilize amide deprotonation should affect

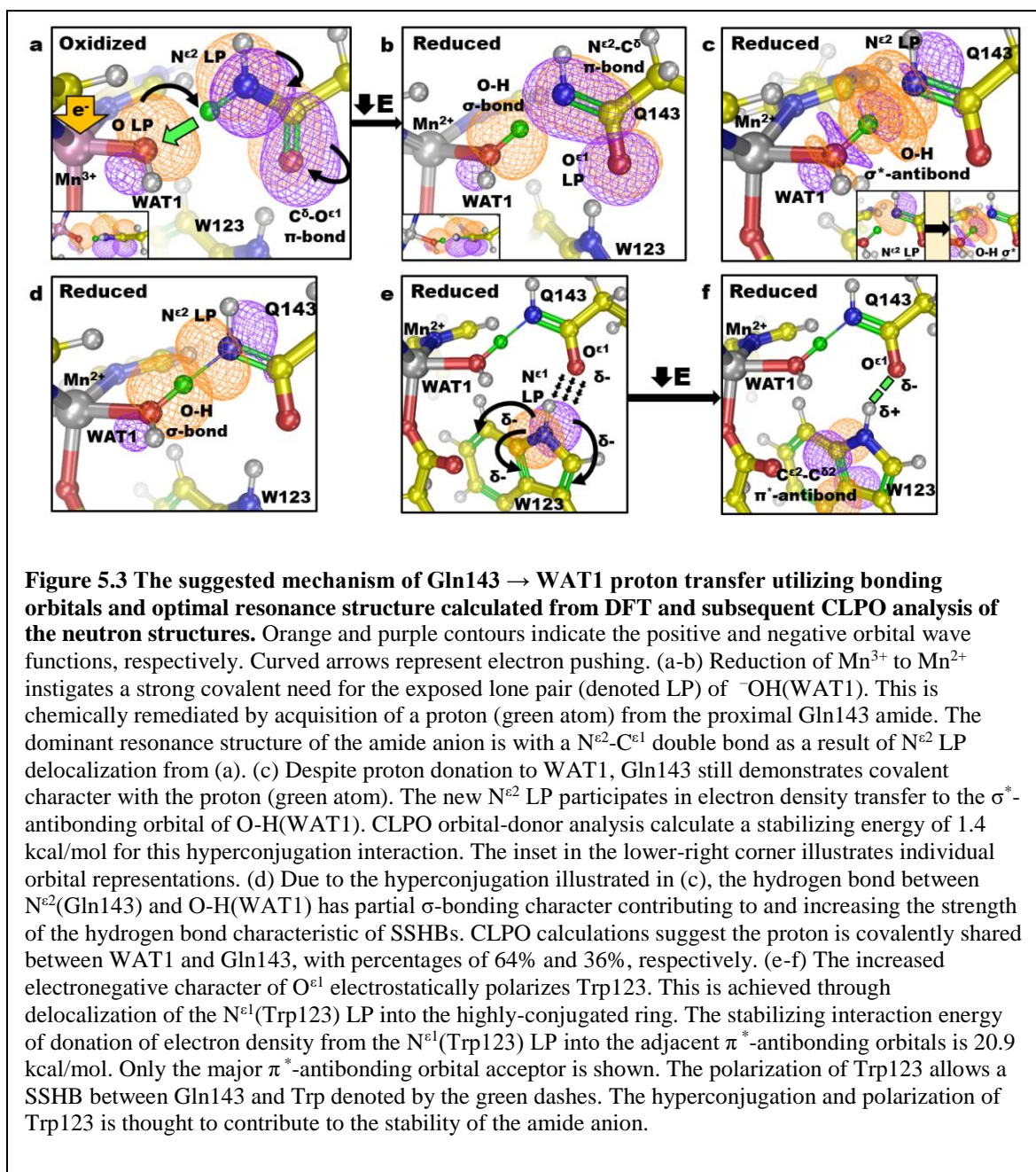


Table 5.2 Gln143 bonding character from CLPO analysis. Numbers are calculated bond order.

	Five-Coordinate Mn ³⁺ Y166(-)H30(ε)Y34(-)	Five-Coordinate Mn ³⁺ Y166(H)H30(δ)Y34(-)	Six-Coordinate Mn ²⁺ Y166(H)H30(δ)Y34(-)	Five-Coordinate Mn ²⁺ Y166(H)H30(δ)Y34(H)
N ^{ε2} -C ^{ε1}	1.36	1.37	1.56	1.52
O ^{ε1} -C ^{ε1}	1.45	1.45	1.30	1.33

Table 5.3 Charge and energy interactions of donor-acceptor CLPO analysis.

Gln143 N^{ε2} Lone Pair → Gln143 C^δ-O^{ε1} π[*]-bond				
State	Donor Occupancy (e ⁻)	Charge Transfer (e ⁻)	Acceptor Occupancy (e ⁻)	Energy (De)stabilization (kcal/mol)
Five-Coordinate Mn ³⁺ Y166(-)H30(ε)Y34(-)	1.64	0.33	0.38	↑ 12.28
Five-Coordinate Mn ³⁺ Y166(H)H30(δ)Y34(-)	1.64	0.33	0.38	↑ 10.41
Trp123 N^{ε1} Lone Pair → Trp123 C^{ε2}-C^{δ2} π[*]-bond				
State	Donor Occupancy (e ⁻)	Charge Transfer (e ⁻)	Acceptor Occupancy (e ⁻)	Energy (De)stabilization (kcal/mol)
Six-Coordinate Mn ²⁺ Y166(H)H30(δ)Y34(-)	1.57	0.15	0.52	↑ 1.35
Five-Coordinate Mn ²⁺ Y166(H)H30(δ)Y34(H)	1.58	0.15	0.52	↓ 13.52
Gln143 N^{ε2}-H^{ε2} σ-bond → Gln143 C^δ-O^{ε1} σ[*]-bond				
State	Donor Occupancy (e ⁻)	Charge Transfer (e ⁻)	Acceptor Occupancy (e ⁻)	Energy (De)stabilization (kcal/mol)
Six-Coordinate Mn ²⁺ Y166(H)H30(δ)Y34(-)	1.98	0.01	0.04	↑ 43.75
Five-Coordinate Mn ²⁺ Y166(H)H30(δ)Y34(H)	1.98	0.01	0.03	↓ 21.84
His30 N^{ε2} Lone pair → His30 O^{ε1}-N^{δ1} π[*]-bond				
State	Donor Occupancy (e ⁻)	Charge Transfer (e ⁻)	Acceptor Occupancy (e ⁻)	Energy (De)stabilization (kcal/mol)
Five-Coordinate Mn ³⁺ Y166(-)H30(ε)Y34(-)	1.50	0.25	0.45	↓ 15.57
Gln143 N^{ε2} Lone pair → WAT1 O-H σ[*]-bond				
State	Donor Occupancy (e ⁻)	Charge Transfer (e ⁻)	Acceptor Occupancy (e ⁻)	Energy (De)stabilization (kcal/mol)
Six-Coordinate Mn ²⁺ Y166(H)H30(δ)Y34(-)	1.81	0.14	0.15	↓ 0.46
Five-Coordinate Mn ²⁺ Y166(H)H30(δ)Y34(H)	1.78	0.17	0.18	↓ 1.39
His30 N^{δ1} Lone pair → His30 C^γ-C^{δ1} π[*]-bond				
State	Donor Occupancy (e ⁻)	Charge Transfer (e ⁻)	Acceptor Occupancy (e ⁻)	Energy (De)stabilization (kcal/mol)
Five-Coordinate Mn ²⁺ Y166(H)H30(δ)Y34(H)	1.53	0.16	0.30	↑ 3.48
His30 N^{ε2}-C^{ε1} π-bond → His30 C^γ-C^{δ1} π[*]-bond				
State	Donor Occupancy (e ⁻)	Charge Transfer (e ⁻)	Acceptor Occupancy (e ⁻)	Energy (De)stabilization (kcal/mol)
Five-Coordinate Mn ²⁺ Y166(H)H30(δ)Y34(H)	1.89	0.09	0.30	↑ 8.33

Table 5.4. Percent covalence of shared hydrogen atoms in SSHBs bonds from CLPO analysis.

	Five-Coordinate Mn ³⁺ Y166(-)H30(ε)Y34(-)		Five-Coordinate Mn ³⁺ Y166(H)H30(δ)Y34(-)		Six-Coordinate Mn ²⁺ Y166(H)H30(δ)Y34(-)		Five-Coordinate Mn ²⁺ Y166(H)H30(δ)Y34(H)	
(Gln143)N ^{ε2} -H- O(WAT1)	N ^{ε2}	O	N ^{ε2}	O	N ^{ε2}	O	N ^{ε2}	O
	0.92	0.08	0.92	0.08	0.29	0.71	0.36	0.64
(Tyr166)O ^η -H- N ^{ε2} (His30)	O ^η	N ^{ε2}	O ^η	N ^{ε2}	O ^η	N ^{ε2}	O ^η	N ^{ε2}
	0.20	0.80	0.77	0.23	0.76	0.24	0.79	0.21
(Tyr34)O ^η -H- O(WAT2)	O ^η	O	O ^η	O	O ^η	O	O ^η	O
	0.15	0.85	0.23	0.77	0.20	0.80	0.90	0.10
(His30)N ^{δ1} -H- O(WAT2)	N ^{δ1}	O	N ^{δ1}	O	N ^{δ1}	O	N ^{δ1}	O
	0.14	0.86	0.89	0.11	0.88	0.12	0.92	0.08

catalysis. In the literature, the Gln143Asn mutant has nearly ablated catalysis in both redox states while Trp123Phe can perform catalysis for $\text{Mn}^{3+} \rightarrow \text{Mn}^{2+}$ at deficient lower rates (20 ~ 50 %) but not at all for the $\text{Mn}^{2+} \rightarrow \text{Mn}^{3+}$ transition [144,218]. The effect of these mutations suggests that Gln143 is central to catalytic activity while Trp123 is most significant for the $\text{Mn}^{2+} \rightarrow \text{Mn}^{3+}$ half of the redox cycle. The detrimental effects for the Mn^{2+} state due to mutating residue Trp123 may therefore reflect their role in stabilizing the Gln143 amide anion. Indeed, the kinetic behaviors of these mutants were especially puzzling in past studies but amide proton transfer potentially explains them [65,91,144,219]. Further support of Gln143 amide deprotonation is found in other isoforms of MnSODs and prokaryotic FeSODs that have conserved active sites. A closer WAT1-Gln distance correlates with increased redox potentials and catalytic rates [64]. This is perhaps because of an enhanced ability for proton transfers between O(WAT1) and $\text{N}^{\epsilon 2}$ (Gln143). Past mutagenesis studies, differences in catalytic rates among isoforms, and the high catalytic rate of MnSOD may be explained by Gln143 serving as an internal proton source for CPET via amide deprotonation.

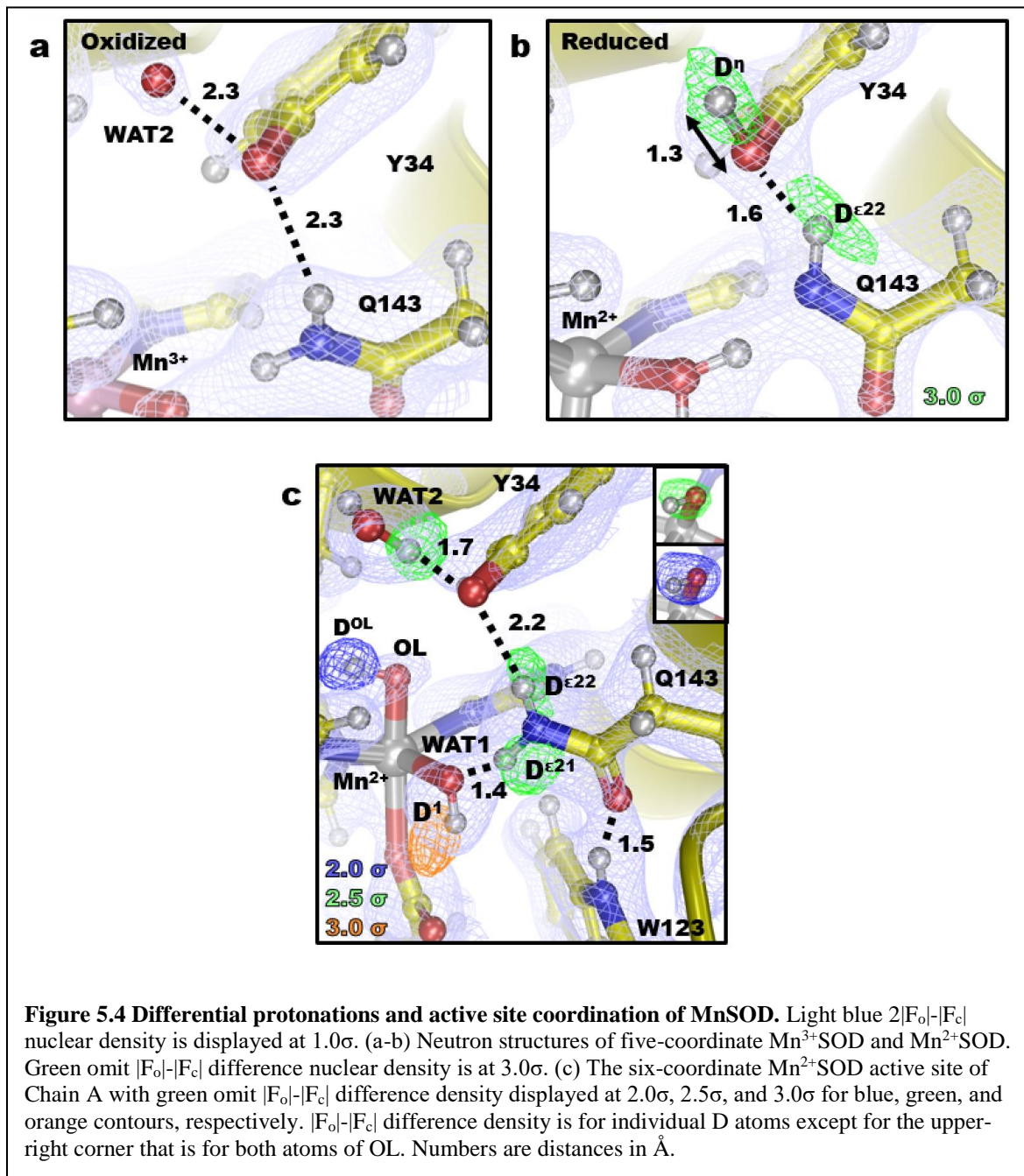
5.3.2 Tyr34 demonstrates an unusual pK_a and forms a SSHB with the Gln143 amide anion

Tyr34 is positioned near the active site solvent channel, hydrogen-bonded to Gln143 (Figure 5.1a), and has been hypothesized to be a proton source for MnSOD CPET [91]. For Mn^{3+}SOD , Tyr34 does not have a nuclear peak for its hydroxyl proton. Deprotonated Tyr34 is making a very strong hydrogen bond with a nearby solvent molecule (designated WAT2) with a 2.3 Å distance between heteroatoms O^{η} (Tyr34) and O(WAT2) (Figure 5.4a). While the deuteriums of WAT2 could not be discerned, the distance is characteristic of a SSHB where Tyr34 may be poised to accept a proton. This interpretation is supported by CLPO analysis from DFT, with 80/20 covalent sharing of the proton (Table 5.4). For Mn^{2+}SOD , a nuclear peak for the hydroxyl proton is present but not where it is expected. Refinement with the ideal 0.97 Å $\text{O}^{\eta}\text{-D}^{\eta}$ distance for Tyr34 persistently demonstrates residual $|\text{F}_o| - |\text{F}_c|$ difference density (Figure 5.5) uncharacteristic of the

other MnSOD tyrosine residues. Between refinement, restraints were incrementally loosened from the 0.97 Å ideal hydroxyl distance until the $|F_o|-|F_c|$ difference density was appropriately absent and the B factors were comparable to other nearby atoms. This yielded an unusual Oⁿ-Dⁿ bond length of 1.3 Å that points towards the solvent channel (Figure 5.4b). Intriguingly, the Oⁿ(Tyr34) atom participates in a strong 1.6 Å hydrogen bond with D^{ε22}(Gln143) in the Mn²⁺SOD structure and is significantly different than the Mn³⁺SOD distance of 2.3 Å (Figure 5.4a-b). This SSHB may potentially be explained by the increased polarization of Gln143 in Mn²⁺SOD from deprotonation to the amide anion leading to a stronger hydrogen bond interaction with Tyr34. It is unclear whether this interaction contributes to Tyr34 differential protonation though it may stabilize the amide anion of Gln143. The experimental data, therefore, suggests Tyr34 is capable of differential protonation at physiological pH, has an unusual pK_a, and participates in atypical hydrogen bonding.

Our experimental data for Tyr34 potentially makes light of the unexplained observations of previous studies investigating its role in catalysis [73,91,144]. Tyr34 has been speculated to be the proton donor to WAT1 for CPET during the Mn³⁺ → Mn²⁺ reaction though this conflicts with the pH independence of the reaction between values of 6 and 10 [62,73]. This was puzzling because CPET mechanisms are expected to have pH dependence as a result of the proton transfer part of their catalysis and Tyr34 is the closest titratable residue. Instead, the MnSOD neutron data suggest that the proton donor to WAT1 is internally sourced from Gln143 without the involvement of solvent and cannot be Tyr34 due to its observed deprotonation in the Mn³⁺ state.

An ionized tyrosine residue at physiological pH is unusual though has been visualized in studies of human carbonic anhydrase II (HCA II) that is a metalloenzyme with diffusion-limited catalytic efficiencies like MnSOD. For HCA II, joint neutron crystallography and NMR demonstrate a tyrosine residue with a pK_a of 7.10 ± 0.10 at the active site [220]. The catalytic role of an ionizable Tyr34 for MnSOD is prominent during the Mn²⁺ → Mn³⁺ redox cycle and is supported by the inability of the Tyr34Phe mutant to catalyze this step of the reaction [221]. Since



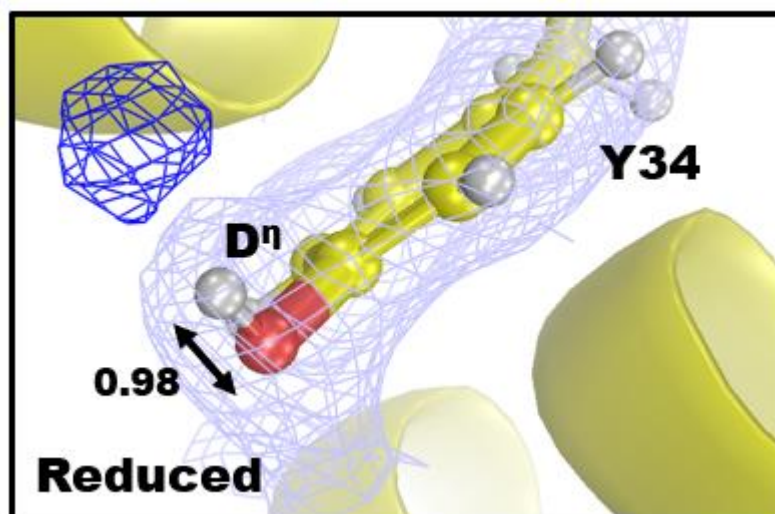


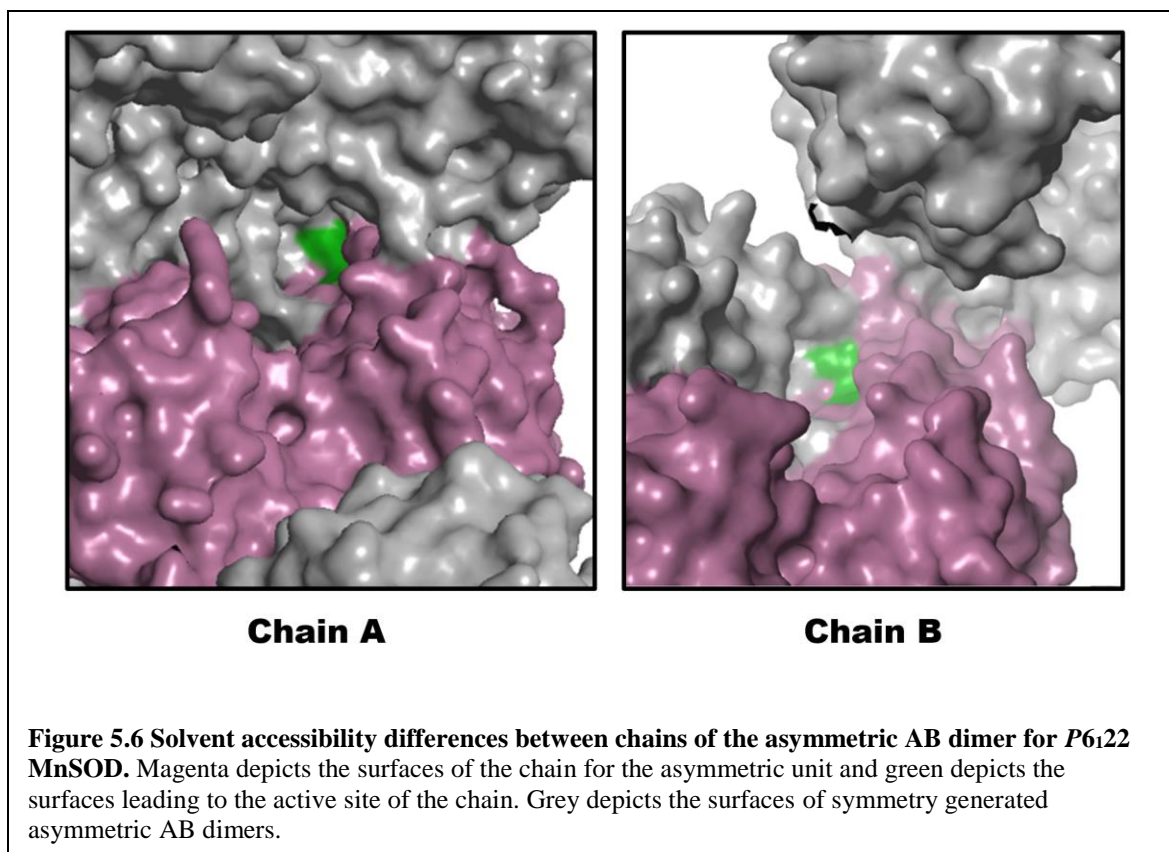
Figure 5.5 Residual density for the hydroxyl group of Tyr34 in Mn^{2+} SOD of chain B. Light blue $2|F_o| - |F_c|$ nuclear density displayed at 1.0σ . Dark blue omit $|F_o| - |F_c|$ difference density is displayed at 2.0σ . Number is distance in Å.

Tyr34 gains a proton during the $\text{Mn}^{3+} \rightarrow \text{Mn}^{2+}$ redox cycle and loses a proton during the $\text{Mn}^{2+} \rightarrow \text{Mn}^{3+}$ cycle, it is conceivable that Tyr34 serves as the source for one of the two protons involved in the protonation of the substrate to H_2O_2 . Indeed, spectroscopic data of the Tyr34Phe mutant suggests a prolonged binding of a species to the metal but could also be a result of the inability of Gln143 to deprotonate without stabilization from the Tyr34 hydroxyl group [91]. Our crystallographic neutron data has shed new light on the perplexing role of the conserved Tyr34 residue.

5.3.3 Serendipitous ligand binding to Mn^{2+} SOD helps explain catalysis

There are two subunits in the crystallographic asymmetric unit. One of the active sites of the Mn^{2+} SOD neutron structure has density for a sixth-coordinate OD^- ligand (designated OL for anionic oxygen ligand, Figure 5.4c). The 1.84 Å Mn-O distance of OL most closely supports a Mn^{2+} bound with OD^- [208] and the B-factor of OL is comparable to other molecules of the active site. The different crystallographic active site coordination of Mn^{2+} SOD may be a consequence of the crystallographic asymmetric subunits having different capacities of solvent accessibility (Figure 5.6). Likewise, OL has been observed in two X-ray crystal structures of *E. coli* MnSOD by our group when OD^- was added to the buffer system and it was also not found in every active site [99,108]. For the present study, the buffer system used for neutron data collection carefully did not include OD^- , and only appropriate ratios of K_2DPO_4 and KD_2PO_4 were used to achieve a pD equivalent to physiologically pH. We think the ligand may have resulted serendipitously from a polarized water molecule that lost a proton. Nevertheless, the bound sixth-coordinate ligand to the active site of Mn^{2+} SOD chain A has a unique combination of structural characteristics that helps explain catalysis.

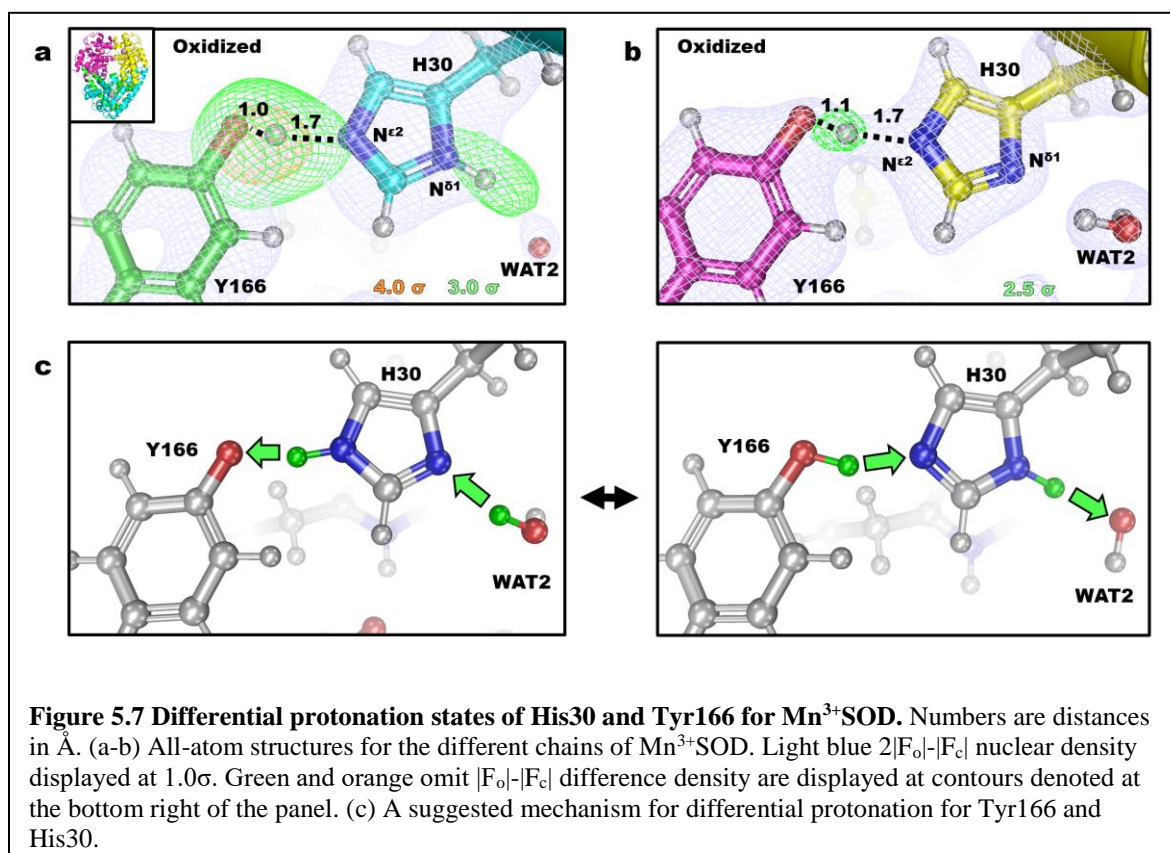
OL may help facilitate Gln143 amide deprotonation. The six-coordinate active site has a Gln143 in the canonical amide form making very strong hydrogen bonds with WAT1 and Trp123 that have bond distances of 1.4 and 1.5 Å, respectively (Figure 5.4c). These distances are



characteristic of SSHBs that may contribute to catalysis. Interestingly, the density of WAT1 is that of a hydroxide even though the Mn is stably reduced but likely has partial H₂O character given the shortness of the hydrogen bond with the nearby amide D^{ε21} proton. The Mn²⁺ protein-ligand bond lengths between the two active sites are not the same. In particular, the Mn-O^{ε2}(D159) is stretched when OL is bound. The D^{ε21}(Gln143) atom that bridges O(WAT1) and N^{ε2}(Gln143) has a slightly higher B-factor of 21 Å² when compared to the B factors of 17 Å² for O(WAT1) and 18 Å² N^{ε2}(Gln143) and may reflect movement between O(WAT1) and N^{ε2}(Gln143). Tyr34 is not protonated but appears poised to be protonated by WAT2 as indicated by a (D)WAT2-Oⁿ(Tyr34) bond distance of 1.7 Å. Binding by an anionic OL would lower the positive charge of Mn²⁺ and increasing the negative character of WAT1 to help initiate Gln143 amide deprotonation. In their investigation of active site pK_as for MnSOD activity, the Miller group suggested sixth-coordinate binding of an ⁻OH ligand to the Mn²⁺SOD active site at native conditions [158]. They note that an electronegative deprotonated Tyr34 and electropositive Mn could polarize a water molecule to have increased ⁻OH character and lose a proton. Since Tyr34 is deprotonated in the six-coordinate structure, proton abstraction from a water molecule likely occurs elsewhere, perhaps by nearby His30. As inferred by the five-coordinate Mn²⁺SOD active site structure, subsequent catalytic steps involve OL leaving the active site, perhaps by protonation to water, and Tyr34 becoming protonated.

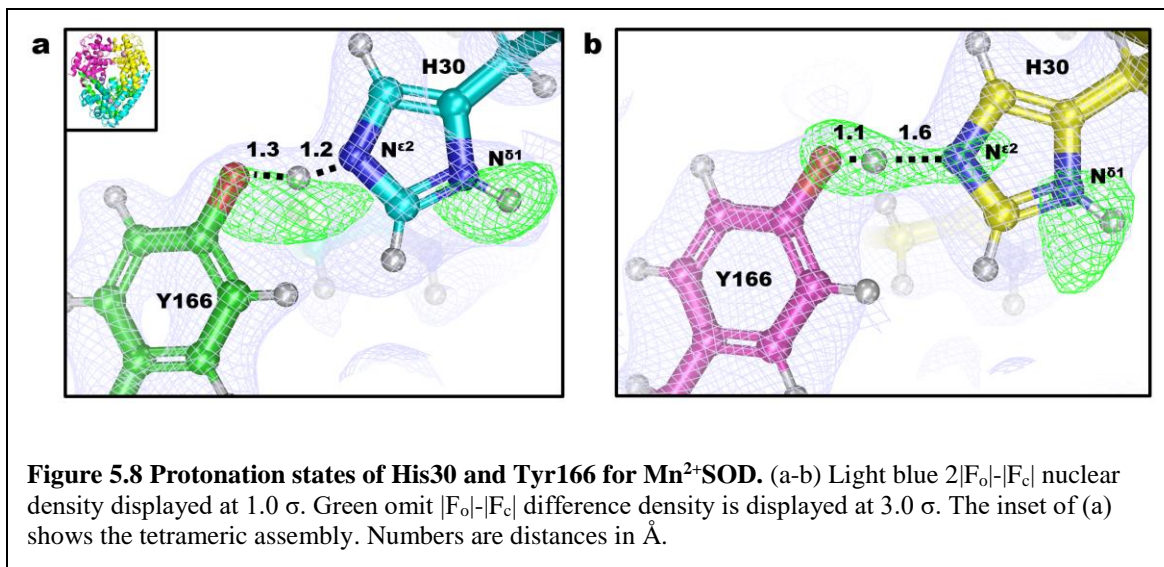
5.3.4 His30 has unusual pK_a that is tied to Tyr166 from across the dimer interface

Second sphere residue His30 is also differentially protonated. Like Tyr34, His30 is solvent-exposed and positioned at the active site solvent channel. WAT2 provides a hydrogen-bond bridge between Tyr34 and His30 (Figure 5.1a). Nuclear peaks of the neutron structures indicate differential protonation at the N^{δ1} of His30 that faces the solvent channel for Mn³⁺SOD (Figure 5.7a-b). The crystallographic asymmetric unit has one active site with N^{δ1} protonated while the



other is not protonated. This is not the case for Mn^{2+}SOD , where both chains show nuclear density for $\text{N}^{\delta 1}$ protonation (Figure 5.8). The hydrogen bond between His30 and Tyr166 for the Mn^{3+}SOD chain A active site (Figure 5.7a) appears to have strong and elongated omit $|F_o| - |F_c|$ difference density for the D atom and this is the case for all active sites of Mn^{2+}SOD . This may suggest presence of a SSHB with covalent but unequal sharing of the D atom between $\text{O}^{\eta}(\text{Tyr166})$ and $\text{N}^{\epsilon 2}(\text{His30})$ and/or movement of the D atom between the two residues. Since $\text{N}^{\epsilon 2}(\text{His30})$ is solvent inaccessible along with the entirety of Tyr166 from across the dimer interface, the hydrogen bond between the residues is within an enclosed environment and may behave atypically compared to canonical hydrogen bonds.

For the active site absent of a proton at $\text{N}^{\delta 1}$ for His30 (Figure 5.7b), the D atom between $\text{O}^{\eta}(\text{Tyr166})$ and $\text{N}^{\epsilon 2}(\text{His30})$ has a lesser $|F_o| - |F_c|$ difference density peak and appears covalent with $\text{O}^{\eta}(\text{Tyr166})$. His30 thus appears absent of protons at both of its nitrogens suggesting an imidazolate anion. We considered the presence of an imidazolate anion as chemically unlikely though deliberated over the possibility along with alternative explanations. The pK_a of [imidazole \leftrightarrow imidazolate] is 14 and compares with the pK_a s of $[\text{HOH} \leftrightarrow \text{OH}^-]$ and $[\text{HO-Tyr} \leftrightarrow \text{O}^--\text{Tyr}]$ that are 14 and 10, respectively [222]. Since the electrostatic surface area encompassing and surrounding the active site is positively charged (Figure 5.1a), it is conceivable that negatively-charged species are promoted. While it is known that active site residues have significantly perturbed pK_a s due to such effects, we could not find literature suggesting an imidazolate histidine unless it is directly bound to a metal. Alternatively, His30 may shift between singly $\text{N}^{\delta 1}$ - or $\text{N}^{\epsilon 2}$ -protonated tautomers and density may be absent due to proton movement and/or differences in solvent accessibility between crystallographic active sites (Figure 5.6). This would be similar to the histidines found in catalytic triads of proteases, where differential protonation of one nitrogen could be tied to the protonation state of the other with the help of a SSHB interaction [223]. It should be noted in the $\text{N}^{\delta 1}$ -protonated active site (Figure 5.7a) that the omit $|F_o| - |F_c|$ difference



density at 3.0σ for the $N^{\delta 1}$ -bound proton is elongated and faces towards solvent. This may be interpreted as proton exchange with solvent. Investigating the literature for other enzymes utilizing a tyrosine-histidine pair in catalysis reveals the metalloenzyme Photosystem II (PSII) that utilizes CPETs [224]. The tyrosine-histidine pair of (PSII) appears to have a SSHB that needs to be maintained for catalysis with measured pK_a values ranging between 7.3 and 8.0. For MnSOD, the Tyr166-His30 interaction is needed for catalysis though it is unclear whether the differential protonation observed at $N^{\delta 1}$ (His30) is modulated with an imidazolate anion or tautomerization.

Previous mutagenesis studies suggest that the Tyr166 and His30 interaction is needed for catalysis and support the interpretation of proton transfers occurring between $N^{\epsilon 2}$ (His30) and O^{η} (Tyr166) that may coincide with differential protonation of $N^{\delta 1}$ (His30) (Figure 5.7c). To judge whether protonation of histidine is significant for enzymatic activity, site-directed mutagenesis of His \rightarrow Gln is often performed due to the similar side-chain structures [225]. His30Gln is the only His30 mutant that has been studied that maintains the hydrogen bonding at the active site and does not significantly affect the positions of other residues at the active site [70,71]. Kinetically, the His30Gln rate for k_1 ($Mn^{3+} \rightarrow Mn^{2+}$) is 38% of the wildtype while k_2 ($Mn^{2+} \rightarrow Mn^{3+}$) is 72% [63]. The rates indicate an important role for His30 k_1 that may correspond with our observations of its differential protonation only in Mn^{3+} SOD. It should be noted that previous studies refrain from attributing differential protonations to His30 due to the similar redox potentials between wildtype (393 ± 29 mV) and His30Gln (380 ± 30 mV) [70,71,105]. However, the investigations do not consider whether compensatory protonations or deprotonations occur at nearby residues as a result of the mutation giving the appearance of an inconsequential effect. Indeed, the Tyr34Phe mutant also has an insignificant change of redox potential (435 ± 30 mV) but has nearly identical rate for k_1 (37% of wildtype) compared to His30Gln [63,70]. Drawing inference from the Tyr166Phe mutant is difficult because hydrogen bonding and side-chain conformations are significantly changed at the active site but has nearly identical measurements of redox potential (436 ± 10 mV)

compared to Tyr34Phe indicating a synonymous effect to the charge of the active site [63,70]. The neutron data for His30 and Tyr166 potentially explains past observations of MnSOD mutants that were difficult to explain and ties together changes of protonation state with kinetic and redox potential measurements.

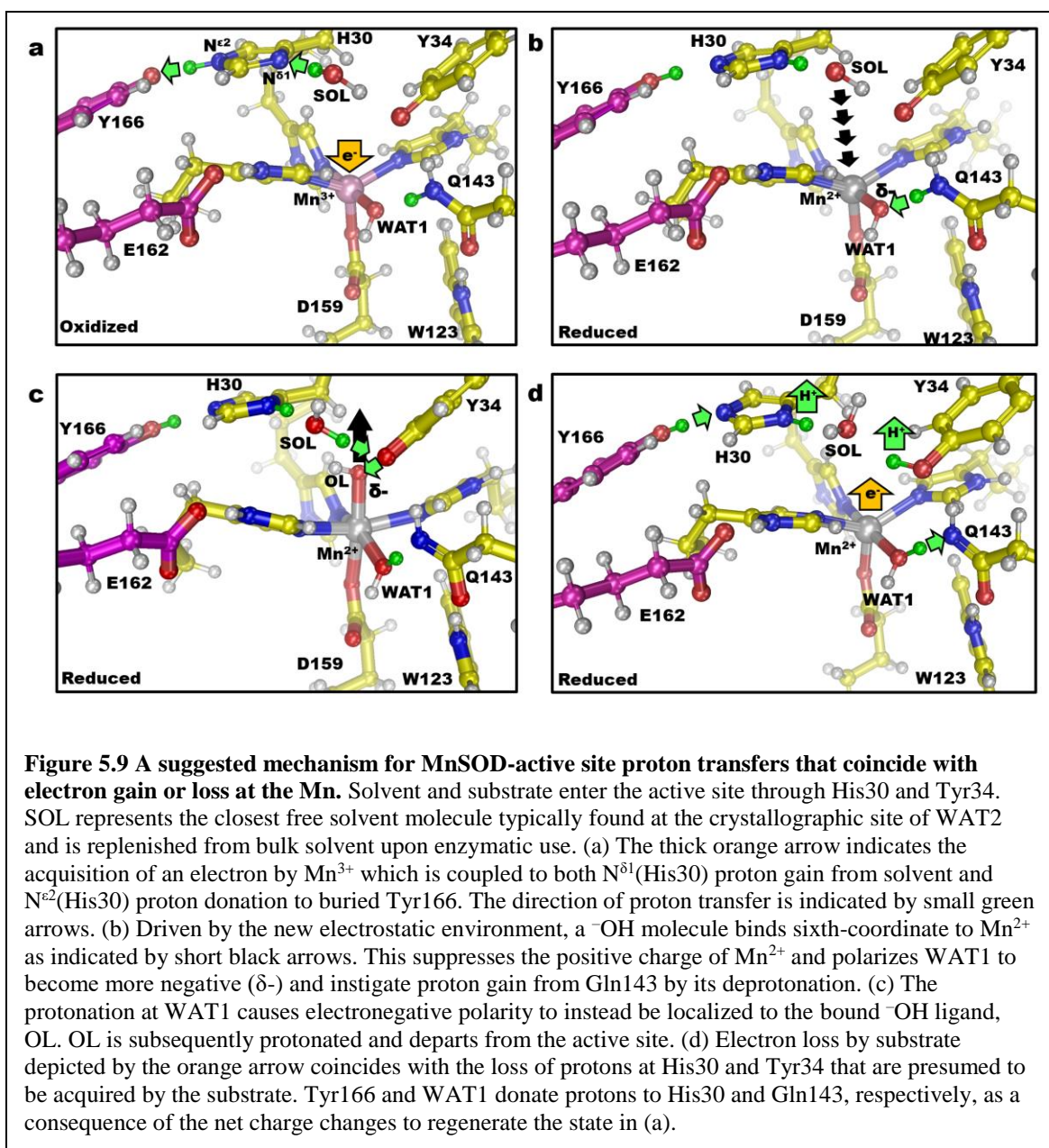
5.4 Conclusions

In total, the present work provides details for an unusual CPET mechanism for human MnSOD. Through neutron diffraction, direct evidence is observed for (1) an internal protonation mechanism via glutamine amide deprotonation supported by quantum calculations, (2) differentially protonated Tyr34, (3), alternate protonation states for His30 that may coincide with the protonation state of Tyr166 across the dimer interface, and (4) SSHBs at sites of differential protonation. As a result of obtaining neutron structures for both Mn^{3+} and Mn^{2+} states, we built a suggested mechanism that details the changes of protonation states as a result of the Mn gaining or losing an electron.

Starting from the resting state, five-coordinate Mn^{3+} acquires an electron (in reality from the substrate) that coincides with $\text{N}^{\delta 1}(\text{His30})$ acquiring a proton from the nearest solvent molecule (the crystallographic position of WAT2) and Tyr166 gaining a proton from $\text{N}^{\epsilon 2}(\text{His30})$ (Figure 5.9a). The Mn^{2+} active site then binds ^-OH to form a six-coordinate Mn^{2+} complex (Figure 5.9b). This may be the same solvent molecule that donated a proton to His30 and its binding is promoted by the electrostatics of the active site. The depression of Mn^{2+} positive charge through ^-OH binding causes negative polarization at WAT1 and triggers proton abstraction from Gln143. Consequently, the WAT1-Gln143 is more stabilizing and the electronegative polarity now localizes to OL. When substrate is present, the steps of Figure 5.9a-b describe the first CPET where proton and electron transfers are energetically coupled to an extent where they cannot be differentiated with kinetic measurements [62]. The increase of negative character for OL may cause it to act as a better proton acceptor and to be converted to H_2O by protonation from Tyr34 as suggested by the Miller group

[158] (Figure 5.9c). Tyr34 is protonated by the solvent before its proton donation to OL. Once Tyr34 is protonated again, the second CPET may occur. The substrate would then acquire an electron from Mn^{2+} and gain two protons, one from His30 and one from Tyr34, to form the H_2O_2 product (Figure 5.9d). The changes of charge due to proton and electron departure from the active site causes Gln143 to accept the same proton it previously donated to WAT1 and $\text{N}^{\epsilon 2}(\text{His30})$ accepting the proton it previously donated to Tyr166 to regenerate five-coordinate Mn^{3+} .

Altogether, the suggested mechanism utilizes two “internal” proton transfers where the protons move back-and-forth within the active site and two “external” proton transfers where the protons originate from solvent molecules to ultimately be consumed to form the product. The proton transfer between WAT1 and Gln143 is especially central to the mechanism as it permits the cyclic nature of catalysis. From this study, we have revealed, to our knowledge, the first direct coupling of electronic states to protonation states for an oxidoreductase. It is evident the CPET mechanism of MnSOD is not straightforward and is exemplified by an unusual proton donation mechanism via a glutamine deprotonation. Catalysis involves a role for nearly every active site residue. As this is one biologically relevant oxidoreductase in a sea of many, finding the protonation states at the active sites of other oxidoreductases may reveal further novel mechanisms for CPET.



Conclusions and Future Directions

6.1 Conclusions

The presented work investigated the enzymatic mechanism of human MnSOD mainly through crystallographic approaches. With X-ray crystallography, Chapter 2 investigates the means to which superoxide may bind the active site by cryotrapping the azide substrate-analog into the active site. The sixth-coordinate binding of the azide molecule suggests binding of superoxide at the same position as suggested by Lah and colleagues [93]. However, two key caveats of the study should be noted. First, the azide molecule (N_3^-) is three atoms in length while superoxide (O_2^-) is two atoms in length. The difference is critical due to the compact nature of the active site and may affect binding orientation and hydrogen bonding. Second, UV-vis spectroscopic studies suggest cryogenic temperatures may affect the coordination of the active site [101]. However, UV-vis may be perturbed by many factors for metalloenzymes and need to be used in combination with other methods [65,158]. Regardless of the nature of coordination, it is apparent that the negative charge of substrate is utilized for electrostatic guidance by the MnSOD tetramer. The electrostatic surface calculations performed in Chapter 2 demonstrate that the active sites of the tetramer are at the bottom of a positively charged pit while areas of the periphery are negatively charged. The enzyme appears to have strategic placement of charged residues for immediate guidance of substrate to the active site. This guidance has been thought to be regulated by post-translational modifications and is of immense importance to scientists seeking to increase endogenous activity of the enzyme [141]. After publication of the work presented in Chapter 2, several studies sought to investigate the effects of acetylation at Lys65 in regards to electrostatics and activity [226,227]. While Lys65 is far from the active site, its acetylation neutralizes a positive charge and perturbs the net electrostatic vectors in such a way that O_2^- diffusion to the active site is less efficient. MnSOD has other sites of modification, including those of phosphorylation and methylation that both appear to increase activity [85]. However, it is unclear whether these are electrostatic effects or otherwise. Regardless,

it is apparent that surface charges of MnSOD are important for activity and serves as a means to modulate $\text{O}_2^{\bullet -}$ consumption and H_2O_2 production.

The work of Chapter 3 sought to initiate a pipeline for neutron crystallography of human MnSOD. This constituted overcoming several challenges. First, the protein needed to be recombinantly expressed in fully deuterated media. Second, the protein was to be purified and crystallized using hydrogenated reagents but needed to be exchanged with deuterium prior to neutron data collection. Third, the crystal was to be grown to much larger size than that required for X-ray diffraction. Fourth, the unit cell dimensions of $P6_122$ MnSOD crystals were much larger than what was normally used for neutron diffraction. The longest unit cell edge for the MnSOD crystals is 240 Å while previous neutron diffraction studies used crystal forms with unit cell edges of less than 100 Å. This means that MnSOD crystals have less unit cells per volume of crystal and consequentially weaker scattering. Of note is that a high-resolution neutron data set for a unit cell of this size has not been collected prior to the present work. Paramount to collecting the high-resolution neutron data was the MaNDi instrument at ORNL. It utilizes time-of-flight Laue diffraction with a spherical detector setup to allow data collection from many scattering angles and wavelengths ranging from 2-4 Å. Such instrument parameters substantially increase the number of Bragg reflections that can be collected from a single frame of data. While the unit cell dimensions of the $P6_122$ MnSOD crystals is disadvantageous, the high symmetry allows for ~99% data completeness from 6 frames. Since a single image frame takes between 24-48 hours, the symmetry of the crystal is especially advantageous for the interest of time and resources. The work of Chapter 3 presents the technical endeavours that were overcome for $P6_122$ MnSOD crystals and hopefully contributes to pushing the limitations of neutron crystallography.

Chapter 4 takes the work of the prior chapter a step forward by developing methods for redox manipulation of perdeuterated $P6_122$ MnSOD crystals for neutron data collection. One of the advantages of neutron diffraction over X-ray diffraction is the lack of effect on the redox state of

the active site metal. Since X-rays are high-energy electromagnetic waves, they are capable of liberating electron from the atoms of a crystal, especially those of water [75]. The high redox potential of Mn^{3+}SOD means the trivalent metal will have a strong attraction to any “loose” electrons during X-ray data collection and lead to a predominately Mn^{2+}SOD for the individual protein units of the crystal [112]. Consequentially, the high-energy characteristics of X-rays make it difficult to study oxidoreductases in the oxidized state. Likewise, there was a lack of structural characterization for Mn^{3+}SOD prior to the present work. The use of neutrons as a source provided the opportunity to study both redox states of the enzyme by chemically treating the crystals prior to data collection. This is especially important for studying not only MnSOD but for all oxidoreductases due to the CPET-dependent nature of the mechanisms. For studying oxidoreductase mechanisms, the protonation states need to be coupled to particular electronic states experimentally to define a mechanism. Redox manipulation of crystals for neutron diffraction provides an avenue to acquire such direct experimental data and the present work provides an avenue for others to study oxidoreductases in such manner.

While the previous two chapters dealt with presenting the developed methods for neutron crystallography of MnSOD, Chapter 5 exhibits the experimental data ultimately obtained from such methods. Two neutron data sets, Mn^{3+}SOD and Mn^{2+}SOD , were collected from the same crystal. Prior to each data collection, the crystal was treated with the appropriate chemical to achieve the desired redox state. The data sets revealed the hydrogen position for MnSOD for the first time and coupled the electronic states with the protonation states without the presence of substrate. What was especially pronounced from the data were the highly unusual hydrogen bonds being made along with non-canonical proton transfers. For example, deprotonation of the Gln143 amide upon the redox transition of $\text{Mn}^{3+} \rightarrow \text{Mn}^{2+}$ was not expected and there was a very limited number of studies (< 5) that suggested amide deprotonation for any enzyme. This is unsurprising since the pK_a for free amide is 16~18 but Gln143 resides in a confined environment with significant charge that

greatly perturbs the apparent pK_a . The effect of charge is exemplified by the observation that *only* an addition of an electron ($Mn^{3+} \rightarrow Mn^{2+}$) that triggers the amide deprotonation event. While this is supported by QM calculations, Gln143 deprotonation also explains the perplexing observations of past MnSOD mechanistic studies. Along with the SSHBs observed, the appearance of such unusual chemical workings in a very well-studied oxidoreductases brings into question whether other oxidoreductases utilize amide deprotonation for enzymatic activity.

The culmination of work of the present dissertation provides new mechanistic revelations to the well-studied enzyme of human MnSOD. Outside the technical developments demonstrated, the work provides revelations for the means of diffusion and binding of substrate to the active site, the precise protonation states of each redox state, non-canonical hydrogen bonds and proton transfers, and ultimately the CPET enzymatic mechanism. As this is the first study of MnSOD that directly detects hydrogen positions, there still exists much work in not only discerning the mechanism but the chemical drivers of *why* the mechanism occurs in the way it does.

6.2 Future Directions

The electrostatic potential calculations of Chapter 2 lead to inquiries of the effect of post-translational modification on $O_2^{\cdot -}$ diffusion to the active site and MnSOD catalysis activity. As mentioned in the previous section, the work of the Gius group investigated the effect of acetylating Lys65 on electrostatic potential. However, this is a single lysine residue and many others may be acetylated [85]. Likewise, previous work demonstrate phosphorylation of Ser82, methylation of Lys44, and nitration of active site residue Tyr34. These modifications all have an effect on the charge of the residue by adding charge, neutralizing charge, or shielding charge (e.g. methylation). The electrostatic surface potentials of MnSOD appear to be a means of post-translational regulation and has much room to be investigated.

Chapters 3-5 provide the basis for studying the catalytic mechanism of MnSOD with more detail. These chapters present the methods for obtaining neutron structures of the enzyme and permitted the experimental acquisition of hydrogen positions for wildtype Mn^{3+}SOD and Mn^{2+}SOD at resting state. This has led to the identification of specific residues that are differentially protonated for CPET though not the specific role of the residue for enzymatic activity. For example, does a labile proton at a residue serve to modulate the redox potential, protonate substrate, stabilize another residue, or transfer to another residue? Similarly, does a residue that does not demonstrate differential protonation have a role in activity? Such questions can be investigated by utilizing point mutants. Specifically, the residues of Tyr166, His30, Tyr34, Trp123, and Trp161 are of interest because mutations of these sites are deleterious for catalytic activity. It is of interest to identify the changes of protonation states at the activity site with mutation of each residue to infer the role in enzymatic activity. Therefore, acquiring neutron structures of the point mutants in both redox forms will be instrumental in providing more details to our understanding of catalysis.

The application of cryogenic methods would further the understanding of the mechanism as well. Flash-freezing crystals after a ligand soak may cryotrap and retain a ligand-bound active site amenable to neutron structural determination. For example, soaking peroxide into a crystal with subsequent flash freezing may reveal the protonation states of the product-inhibited complex. Each ligand soak may be handled with a strategic MnSOD variant. Following the example of peroxide, the W161F mutant is known to kinetically retain the product-inhibited complex much longer than wildtype without compromising the hydrogen-bond network [63,65,71]. Cryotrapping ligands into large, perdeuterated crystals of MnSOD provide a means to explore the mechanism in regards to substrate and product.

Many crystallographic experiments are possible to further delve into the details of the MnSOD mechanism. The present work has laid a foundation in which MnSOD variants and other active site states may be systematically investigated.

Appendix 1: Preliminary Refinement of the Cryo-trapped W161F MnSOD-Peroxide Complex

Introduction

An interesting and unique feature of human MnSOD's enzymatic mechanism is that product-inhibition limits the output of hydrogen peroxide. Wild-type MnSOD uses this alternative pathway 50% of the time during steady-state conditions and is thought to be characterized by a peroxide anion (O_2^{2-}) bound at the active site ($\text{M}^{3+}\text{--O}_2^{2-}$). This occurs after the first half-reaction of the canonical pathway (note that a M^{2+} oxidation state precludes formation of $\text{M}^{3+}\text{--O}_2^{2-}$). To relieve inhibition at the active site, an alternative proton transfer relay is used to protonate peroxide anion to hydrogen peroxide [72,228]. The product-inhibited pathway is perhaps the least known attribute of the enzyme.

The Borgstahl group published the only cryotrapped X-ray structure of a *Escherichia coli* MnSOD-peroxide complex [108]. This was a landmark study because previously it was not clear that cryotrapping would work on such a fast enzyme and side-on binding of a dioxygen ligand to Mn was revealed. The lack of information on hydrogens in those electron density maps made the precise interpretation of the ligands bound to the four unique active site structures in the crystal impossible. Of note, *E. coli* MnSOD has less product-inhibition than human MnSOD [64]. This means that the *E. coli* structure contains a mixture of ligands from both the canonical and product-inhibited pathways. Also, hydrogen peroxide is known to force the backwards reaction of MnSOD [72]. A hydroperoxyl (HO_2^{\cdot}) intermediate is also thought to exist [64]. These issues made the mechanism hard to decipher from the *E. coli* structure because the double-oxygen species were difficult to differentiate from each other using only X-ray data.

For this study, cryogenic neutron diffraction of the W161F variant is used to analyze the MnSOD-peroxide complex. This way, the active site species may be discerned by protonation state in addition to visualizing the proton relay of the product-inhibited mechanism. The W161F

MnSOD variant was strategically chosen as catalysis is through the product-inhibited pathway exclusively and inhibition release is slow [219].

Materials and methods

Detailed methods for recombinant MnSOD deuterated expression at ORNL biodeuteration lab, purification, and crystallization have been described previously [163]. Of note, expression of the W161F variant was performed at 37 °C instead of the 30 °C in the citation, as this significantly increases Mn metal incorporation of MnSOD [187]. Prior to data collection, a large W161F crystal was soaked with increasing concentrations of deuterated potassium phosphate solution, pD 7.8, while maintaining 1% deuterated peroxide (D_2O_2). After 5 minutes, the crystal was flash frozen with a cryostream before data collection at MaNDi. Neutron data were collected to 2.30 Å resolution with 99% completeness (Table A-1.1). An identical protocol was utilized to collect cryogenic X-ray data using a Rigaku FR-E SuperBright home source. Neutron data were integrated using *MANTID* [189]. Integrated neutron data were scaled and wavelength-normalized using *LAUENORM* from the *LAUGEN* suite [171]. X-ray diffraction data were reduced using *HKL-3000* for indexing, integration, and scaling [124]. Preliminary refinement of both the X-ray and neutron models were performed with *PHENIX.REFINE* from the *PHENIX* suite [190].

Table A-1.1 Data collection statistics

	W161F MnSOD-Peroxide	
	Neutron	X-ray
Diffraction Source	MaNDi	Rigaku FR-E ⁺ SuperBright
Temperature (K)	100	
Space group	<i>P</i> 6 ₁ 22	
<i>a</i> , <i>b</i> , <i>c</i> (Å)	77.8, 77.8, 236.8	78.4, 78.4, 236.97
<i>α</i> , <i>β</i> , <i>γ</i> (°)	90, 90, 120	
Wavelengths (Å)	2-4	1.5418
No. of unique reflections	19467	34472
Resolution range (Å)	14.82-2.30 (2.38-2.30)	50.0-1.87 (1.91-1.87)
Multiplicity	9.72 (7.02)	6.5 (5.2)
<i>I</i> / <i>σ</i> (<i>I</i>)	9.7 (5.6)	11.4 (2.0)
<i>R</i> _{merge}	0.279 (0.286)	-
<i>R</i> _{meas}	0.294 (0.306)	0.12 (0.76)
Data completeness (%)	99.01 (98.04)	93.8 (89.3)

Results

X-ray data collection yielded electron density for a dioxygen species in two locations. Elongated density is seen between putative proton transfer residues His30 and Tyr34 (Figure A-1.1a). This site has been speculated to bind substrate and/or product but has not been seen before [72,228]. The second location is within covalent bond distance of the Mn ion (Figure A-1.1b) and has been seen before but only at partial occupancies [108]. Here, the data refines a dioxygen species at full occupancy to temperature factors comparable to the rest of the active site. Neutron data was subsequently collected to 2.3 Å on cryocooled D₂O₂-soaked perdeuterated W161F crystals and yielded nuclear density similar to that of the X-ray counterpart (Figure A-1.2a-b). Preliminary refinement has begun to reveal unexpected protonation states demonstrated by a low-barrier hydrogen bond seen between His30 and Tyr166 (Figure A-1.2c).

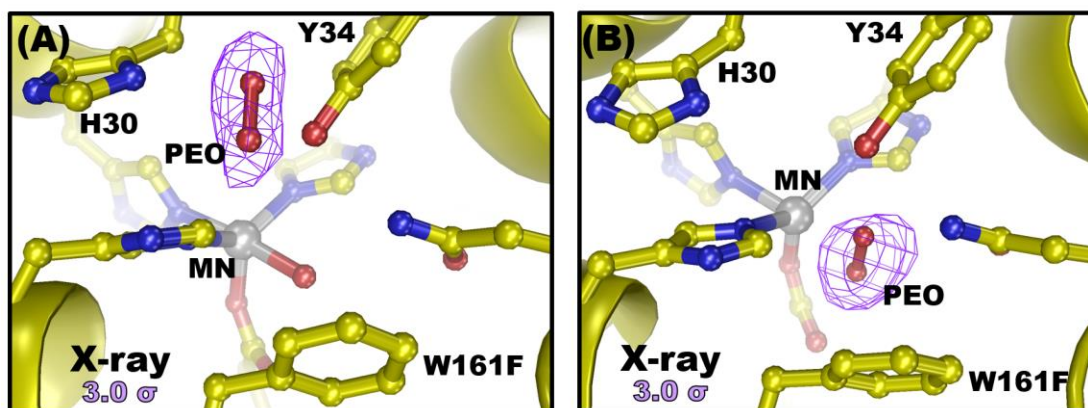
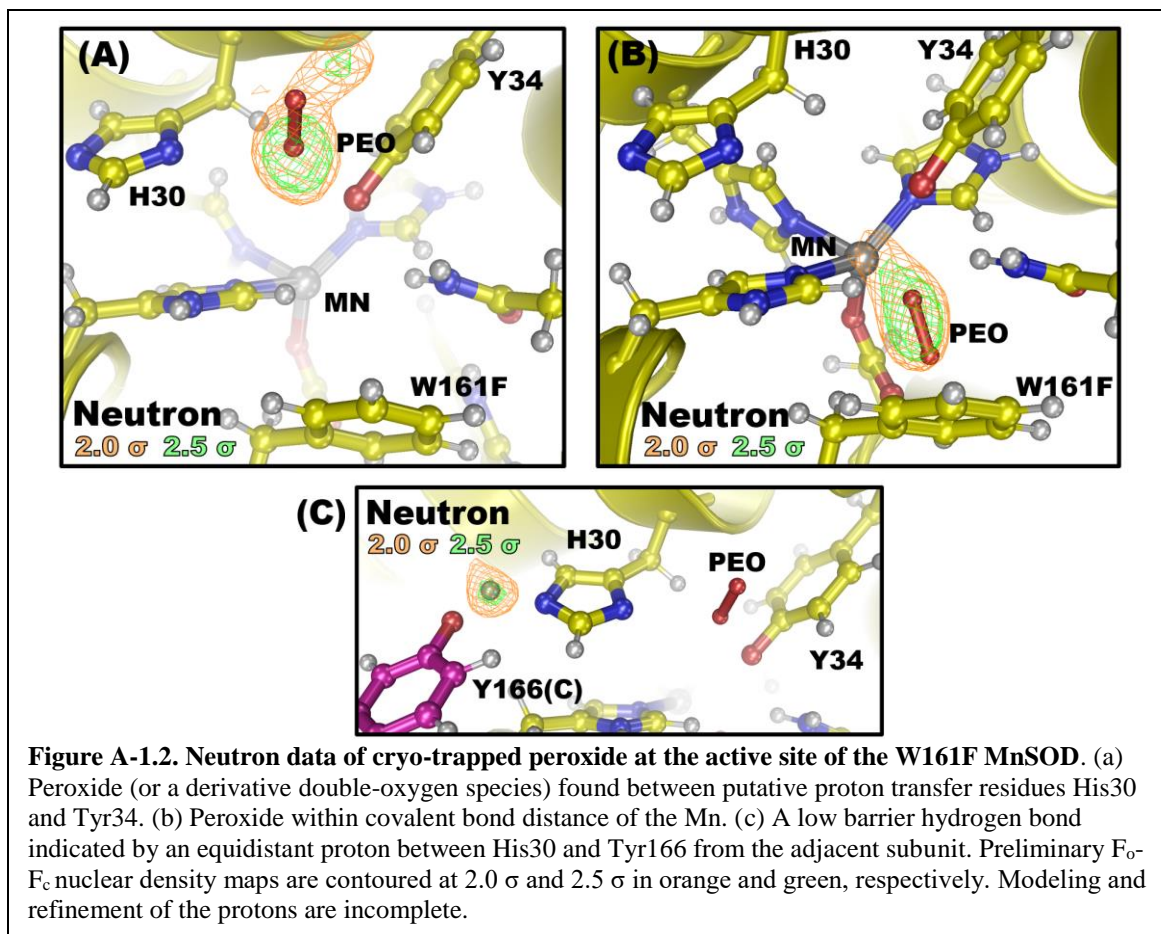


Figure A-1.1. X-ray data of cryo-trapped peroxide at the active site of the W161F MnSOD. (a) Peroxide (or a derivative double-oxygen species) found between putative proton transfer residues His30 and Tyr34. (b) Peroxide within covalent bond distance of the Mn. A single oxygen-containing molecule thought to be involved in proton transfers is normally found here. $F_o - F_c$ electron density maps are contoured at 3.0σ .



Appendix 2: Preliminary Refinement of Y34F MnSOD in Oxidized Form

Introduction

The enzymatic mechanism harbors an alternative pathway that leads to product-inhibition by peroxide. This alternative pathway 50% of the time during steady-state conditions and is thought to be characterized by a peroxide anion (O_2^{2-}) bound at the active site ($\text{M}^{3+}\text{-O}_2^{2-}$). To relieve inhibition at the active site, an alternative proton transfer relay is used to protonate peroxide anion to hydrogen peroxide [72,228]. Kinetic studies show that active site residue Tyr34 mediates access to product-inhibited reactions by comparing rates between the wildtype enzyme with the Y34F mutant [73]. The Y34F mutant uses the alternative product-inhibited pathway ~99% of the time and implicates a role for the hydroxyl group of Tyr34 in permitting canonical activity. Our previous wildtype oxidized and reduced neutron structures demonstrate that Tyr34 is differentially protonated. The residue is ionized in the Mn^{3+}SOD state and protonated in the Mn^{2+}SOD state. To better understand the role of Tyr34, neutron structures for the Y34F mutant in Mn^{3+} and Mn^{2+} states are desired. Here, preliminary refinement of Y34F Mn^{3+}SOD neutron data is presented.

Materials and methods

Detailed methods for recombinant MnSOD deuterated expression at ORNL biodeuteration lab, purification, and crystallization have been described previously [163]. Of note, expression was performed at 37 °C instead of the 30 °C in the citation, as this significantly increases Mn metal incorporation of MnSOD [187]. Purification and crystallization were performed with hydrogenated reagents. Deuterium exchange of crystals was performed by vapor diffusion in capillaries. Methods for manipulating the Mn metal of MnSOD to Mn^{3+} have been described previously [188]. In brief, a crystal in a quartz capillary was soaked in deuterated reservoir solutions containing either 6.4 mM potassium permanganate (KMnO_4) to achieve the Mn^{3+} state. After drying the crystal from soaking solutions, the crystal was flanked in the capillary by slugs of the deuterated reservoir

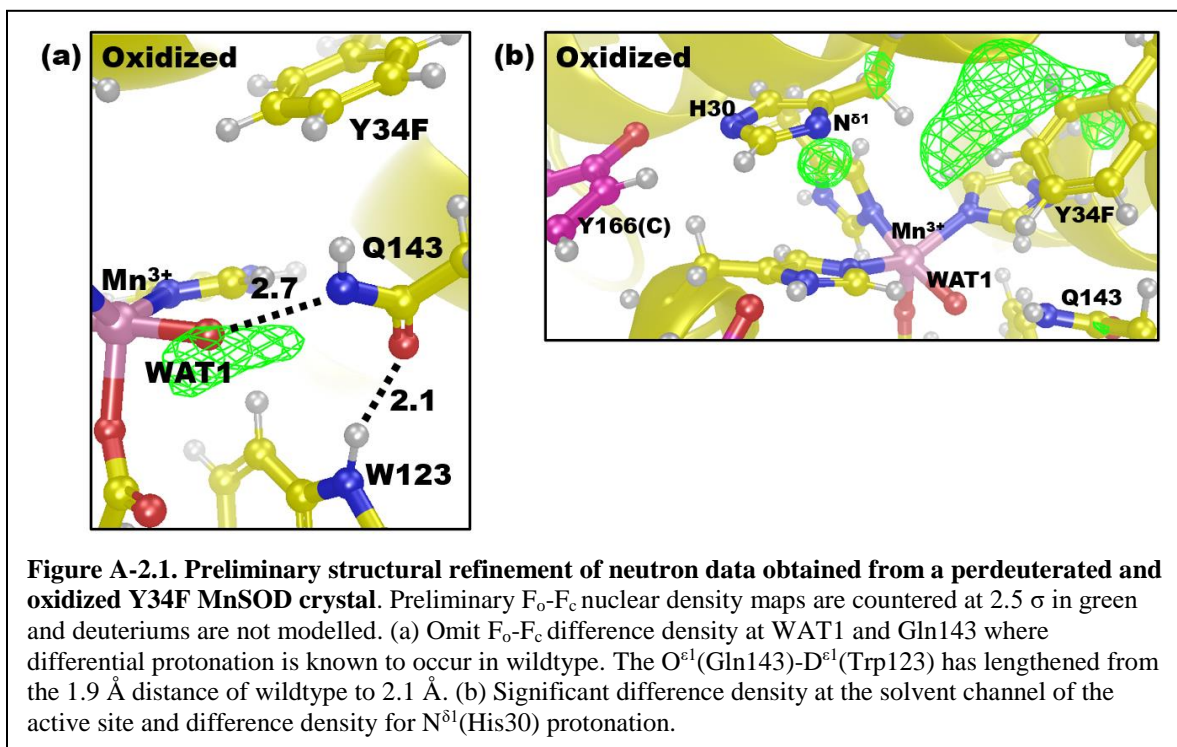
soaking solutions. Fortuitously, the decomposition products of the redox agent are unable to enter the active site of MnSOD [188]. Neutron data were collected to 2.30 Å resolution (Table A-2.1) and integrated using *MANTID* [189]. Integrated neutron data were scaled and wavelength-normalized using *LAUENORM* from the *LAUGEN* suite [171]. Preliminary refinement of the neutron model was performed with *PHENIX.REFINE* from the *PHENIX* suite [190].

Table A-2.1 Data collection statistics
Y34F Mn³⁺SOD

	Neutron
Diffraction Source	MaNDi
Temperature (K)	296
Space group	<i>P</i> 6 ₁ 22
<i>a</i> , <i>b</i> , <i>c</i> (Å)	79.3, 79.3, 240.6
<i>α</i> , <i>β</i> , <i>γ</i> (°)	90, 90, 120
Wavelengths (Å)	2-4
No. of unique reflections	20703
Resolution range (Å)	14.39-2.28 (2.36-2.28)
Multiplicity	7.79 (6.15)
<i>I</i> /σ(<i>I</i>)	7.4 (3.7)
<i>R</i> _{merge}	0.246 (0.323)
<i>R</i> _{meas}	0.263 (0.349)
Data completeness (%)	97.78 (88.40)

Results

The preliminary structural refinement has yet to include exchangeable deuterium atoms at the active site though has notable features and omit $F_o - F_c$ difference density. The phenylalanine at position 34 has caused a slight structural shift of the Gln143 residue. Specifically, the $O^{\epsilon 1}(\text{Gln143}) - D^{\epsilon 1}(\text{Trp123})$ has lengthened from the 1.9 Å distance of wildtype to 2.1 Å (Figure A-2.1a). This is significant because this hydrogen bond is thought to stabilize the amide anion of Gln143 in the Mn^{2+} redox state and may explain why the Y34F mutant cannot perform the fast $\text{Mn}^{2+} \rightarrow \text{Mn}^{3+}$ redox reaction. Despite this structural shift, the WAT1-Gln143 SSHB is maintained from the wildtype structure and omit difference density suggests at least one deuterium for the WAT1 monooxygen species. Significant omit difference density is also seen at the solvent channel between Phe34 and His30 along with density suggesting $N^{\delta 1}(\text{His30})$ protonation (Figure A-2.1b). The work of Chapter 2 and Appendix 1 has suggested that a dioxygen species related to catalysis binds at this position and relates to His30 protonation though more refinement needs to occur to explore this possibility. The preliminary refinement of neutron data obtained from a perdeuterated and oxidized Y34F MnSOD crystal already reveals interesting data related to catalysis.



References

1. Warner, H.R. Superoxide Dismutase, Aging, and Degenerative Disease. *Free Radic. Biol. Med.* **1994**, *17*, 249-258.
2. Fukai, T.; Ushio-Fukai, M. Superoxide Dismutases: Role in Redox Signaling, Vascular Function, and Diseases. *Antioxid. Redox Signal.* **2011**, *15*, 1583-1606.
3. Miao, L.; St Clair, D.K. Regulation of Superoxide Dismutase Genes: Implications in Disease. *Free Radic. Biol. Med.* **2009**, *47*, 344-356.
4. Jastroch, M.; Divakaruni, A.S.; Mookerjee, S.; Treberg, J.R.; Brand, M.D. Mitochondrial Proton and Electron Leaks. *Essays Biochem.* **2010**, *47*, 53-67.
5. Islam, M.T. Oxidative Stress and Mitochondrial Dysfunction-Linked Neurodegenerative Disorders. *Neurol. Res.* **2017**, *39*, 73-82.
6. Van Houten, B.; Woshner, V.; Santos, J.H. Role of Mitochondrial DNA in Toxic Responses to Oxidative Stress. *DNA Repair (Amst)* **2006**, *5*, 145-152.
7. McCord, J.M.; Fridovich, I. Superoxide Dismutase: The First Twenty Years (1968-1988). *Free Radic. Biol. Med.* **1988**, *5*, 363-369.
8. Landis, G.N.; Tower, J. Superoxide Dismutase Evolution and Life Span Regulation. *Mech. Ageing Dev.* **2005**, *126*, 365-379.
9. van der Vliet, A. Antioxidant Defense in the Lung. In *Comparative Biology of the Normal Lung (Second Edition)*, Elsevier Inc.: 2015; pp 489-507.
10. Perry, J.J.; Shin, D.S.; Getzoff, E.D.; Tainer, J.A. The Structural Biochemistry of the Superoxide Dismutases. *Biochim. Biophys. Acta* **2010**, *1804*, 245-262.
11. Sentman, M.L.; Granstrom, M.; Jakobson, H.; Reaume, A.; Basu, S.; Marklund, S.L. Phenotypes of Mice Lacking Extracellular Superoxide Dismutase and Copper- and Zinc-Containing Superoxide Dismutase. *J. Biol. Chem.* **2006**, *281*, 6904-6909.
12. Noor, R.; Mittal, S.; Iqbal, J. Superoxide Dismutase – Applications and Relevance to Human Diseases. *Med. Sci. Monit.* **2002**, *8*, 210-215.
13. Elchuri, S.; Oberley, T.D.; Qi, W.; Eisenstein, R.S.; Jackson Roberts, L.; Van Remmen, H.; Epstein, C.J.; Huang, T.T. Cuznsod Deficiency Leads to Persistent and Widespread Oxidative Damage and Hepatocarcinogenesis Later in Life. *Oncogene* **2005**, *24*, 367-380.
14. Saccon, R.A.; Bunton-Stasyshyn, R.K.; Fisher, E.M.; Fratta, P. Is Sod1 Loss of Function Involved in Amyotrophic Lateral Sclerosis? *Brain* **2013**, *136*, 2342-2358.
15. Lebovitz, R.M.; Zhang, H.; Vogel, H.; Cartwright, J., Jr.; Dionne, L.; Lu, N.; Huang, S.; Matzuk, M.M. Neurodegeneration, Myocardial Injury, and Perinatal Death in Mitochondrial Superoxide Dismutase-Deficient Mice. *Proc. Natl. Acad. Sci. U. S. A.* **1996**, *93*, 9782-9787.
16. Li, Y.; Huang, T.T.; Carlson, E.J.; Melov, S.; Ursell, P.C.; Olson, J.L.; Noble, L.J.; Yoshimura, M.P.; Berger, C.; Chan, P.H.; Wallace, D.C.; Epstein, C.J. Dilated Cardiomyopathy and Neonatal Lethality in Mutant Mice Lacking Manganese Superoxide Dismutase. *Nat. Genet.* **1995**, *11*, 376-381.
17. Drose, S.; Brandt, U. The Mechanism of Mitochondrial Superoxide Production by the Cytochrome Bc1 Complex. *J. Biol. Chem.* **2008**, *283*, 21649-21654.
18. Sies, H.; Berndt, C.; Jones, D.P. Oxidative Stress. *Annu. Rev. Biochem.* **2017**, *86*, 715-748.
19. Melser, S.; Lavie, J.; Benard, G. Mitochondrial Degradation and Energy Metabolism. *Biochim. Biophys. Acta* **2015**, *1853*, 2812-2821.

20. Jezek, J.; Cooper, K.F.; Strich, R. Reactive Oxygen Species and Mitochondrial Dynamics: The Yin and Yang of Mitochondrial Dysfunction and Cancer Progression. *Antioxidants (Basel)* **2018**, *7*.
21. Nita, M.; Grzybowski, A. The Role of the Reactive Oxygen Species and Oxidative Stress in the Pathomechanism of the Age-Related Ocular Diseases and Other Pathologies of the Anterior and Posterior Eye Segments in Adults. *Oxid. Med. Cell. Longev.* **2016**, *2016*, 3164734.
22. Muller, F.L.; Lustgarten, M.S.; Jang, Y.; Richardson, A.; Van Remmen, H. Trends in Oxidative Aging Theories. *Free Radic. Biol. Med.* **2007**, *43*, 477-503.
23. Gao, L.; Laude, K.; Cai, H. Mitochondrial Pathophysiology, Reactive Oxygen Species, and Cardiovascular Diseases. *Vet. Clin. North Am. Small Anim. Pract.* **2008**, *38*, 137-155, vi.
24. Pacher, P.; Beckman, J.S.; Liaudet, L. Nitric Oxide and Peroxynitrite in Health and Disease. *Physiol. Rev.* **2007**, *87*, 315-424.
25. Villanueva, C.; Giulivi, C. Subcellular and Cellular Locations of Nitric Oxide Synthase Isoforms as Determinants of Health and Disease. *Free Radic. Biol. Med.* **2010**, *49*, 307-316.
26. Giulivi, C.; Kato, K.; Cooper, C.E. Nitric Oxide Regulation of Mitochondrial Oxygen Consumption I: Cellular Physiology. *Am. J. Physiol. Cell Physiol.* **2006**, *291*, C1225-1231.
27. Lacza, Z.; Pankotai, E.; Busija, D.W. Mitochondrial Nitric Oxide Synthase: Current Concepts and Controversies. *Front Biosci (Landmark Ed)* **2009**, *14*, 4436-4443.
28. Brown, G.C.; Borutaite, V. Inhibition of Mitochondrial Respiratory Complex I by Nitric Oxide, Peroxynitrite and S-Nitrosothiols. *Biochim. Biophys. Acta* **2004**, *1658*, 44-49.
29. Cantu, D.; Schaack, J.; Patel, M. Oxidative Inactivation of Mitochondrial Aconitase Results in Iron and H₂O₂-Mediated Neurotoxicity in Rat Primary Mesencephalic Cultures. *PLoS One* **2009**, *4*, e7095.
30. Pearce, L.L.; Martinez-Bosch, S.; Manzano, E.L.; Winnica, D.E.; Epperly, M.W.; Peterson, J. The Resistance of Electron-Transport Chain Fe-S Clusters to Oxidative Damage During the Reaction of Peroxynitrite with Mitochondrial Complex Ii and Rat-Heart Pericardium. *Nitric Oxide* **2009**, *20*, 135-142.
31. Lopez, C.J.; Qayyum, I.; Mishra, O.P.; Delivoria-Papadopoulos, M. Effect of Nitration on Protein Tyrosine Phosphatase and Protein Phosphatase Activity in Neuronal Cell Membranes of Newborn Piglets. *Neurosci. Lett.* **2005**, *386*, 78-81.
32. Sultana, R.; Perluigi, M.; Allan Butterfield, D. Lipid Peroxidation Triggers Neurodegeneration: A Redox Proteomics View into the Alzheimer Disease Brain. *Free Radic. Biol. Med.* **2013**, *62*, 157-169.
33. Riley, P.A. Free Radicals in Biology: Oxidative Stress and the Effects of Ionizing Radiation. *Int. J. Radiat. Biol.* **1994**, *65*, 27-33.
34. Sun, Y.; Yin, Y.; Zhang, J.; Yu, H.; Wang, X.; Wu, J.; Xue, Y. Hydroxyl Radical Generation and Oxidative Stress in Carassius Auratus Liver, Exposed to Pyrene. *Ecotoxicol. Environ. Saf.* **2008**, *71*, 446-453.
35. Lipinski, B. Hydroxyl Radical and Its Scavengers in Health and Disease. *Oxid. Med. Cell. Longev.* **2011**, *2011*, 809696.
36. Thomas, C.; Mackey, M.M.; Diaz, A.A.; Cox, D.P. Hydroxyl Radical Is Produced Via the Fenton Reaction in Submitochondrial Particles under Oxidative Stress: Implications for Diseases Associated with Iron Accumulation. *Redox Rep* **2013**, *14*, 102-108.
37. Cadenas, E.; Davies, K.J. Mitochondrial Free Radical Generation, Oxidative Stress, and Aging. *Free Radic. Biol. Med.* **2000**, *29*, 222-230.
38. Goldstein, S.; Merenyi, G. The Chemistry of Peroxynitrite: Implications for Biological Activity. *Methods Enzymol.* **2008**, *436*, 49-61.

39. Beckman, J.S.; Beckman, T.W.; Chen, J.; Marshall, P.A.; Freeman, B.A. Apparent Hydroxyl Radical Production by Peroxynitrite: Implications for Endothelial Injury from Nitric Oxide and Superoxide. *Proc. Natl. Acad. Sci. U. S. A.* **1990**, *87*, 1620-1624.
40. Kell, D.B. Towards a Unifying, Systems Biology Understanding of Large-Scale Cellular Death and Destruction Caused by Poorly Liganded Iron: Parkinson's, Huntington's, Alzheimer's, Prions, Bactericides, Chemical Toxicology and Others as Examples. *Arch. Toxicol.* **2010**, *84*, 825-889.
41. Davies, K.J. Protein Damage and Degradation by Oxygen Radicals. I. General Aspects. *J. Biol. Chem.* **1987**, *262*, 9895-9901.
42. Guo, C.; Sun, L.; Chen, X.; Zhang, D. Oxidative Stress, Mitochondrial Damage and Neurodegenerative Diseases. *Neural Regen Res* **2013**, *8*, 2003-2014.
43. van der Veen, R.C.; Roberts, L.J. Contrasting Roles for Nitric Oxide and Peroxynitrite in the Peroxidation of Myelin Lipids. *J. Neuroimmunol.* **1999**, *95*, 1-7.
44. Giulivi, C.; Boveris, A.; Cadenas, E. Hydroxyl Radical Generation During Mitochondrial Electron Transfer and the Formation of 8-Hydroxydesoxyguanosine in Mitochondrial DNA. *Arch. Biochem. Biophys.* **1995**, *316*, 909-916.
45. Agarwal, A.; Tvrdá, E.; Mulgund, A. Oxidative Stress in Preeclampsia. In *Handbook of Fertility*, Watson, R.R., Ed. Academic Press: 2015; pp 283-290.
46. Yasui, M.; Kanemaru, Y.; Kamoshita, N.; Suzuki, T.; Arakawa, T.; Honma, M. Tracing the Fates of Site-Specifically Introduced DNA Adducts in the Human Genome. *DNA Repair (Amst)* **2014**, *15*, 11-20.
47. Radi, R. Nitric Oxide, Oxidants, and Protein Tyrosine Nitration. *Proc. Natl. Acad. Sci. U. S. A.* **2004**, *101*, 4003-4008.
48. Quint, P.; Reutzel, R.; Mikulski, R.; McKenna, R.; Silverman, D.N. Crystal Structure of Nitrated Human Manganese Superoxide Dismutase: Mechanism of Inactivation. *Free Radic. Biol. Med.* **2006**, *40*, 453-458.
49. Radi, R.; Cassina, A.; Hodara, R.; Quijano, C.; Castro, L. Peroxynitrite Reactions and Formation in Mitochondria. *Free Radic. Biol. Med.* **2002**, *33*, 1451-1464.
50. Turko, I.V.; Li, L.; Aulak, K.S.; Stuehr, D.J.; Chang, J.Y.; Murad, F. Protein Tyrosine Nitration in the Mitochondria from Diabetic Mouse Heart. Implications to Dysfunctional Mitochondria in Diabetes. *J. Biol. Chem.* **2003**, *278*, 33972-33977.
51. Kilinc, K.; Kilinc, A. Mutagenic Actions of Nitrogen Oxides. *Indoor Built Environ* **2005**, *14*, 503-512.
52. Yang, J.L.; Weissman, L.; Bohr, V.A.; Mattson, M.P. Mitochondrial DNA Damage and Repair in Neurodegenerative Disorders. *DNA Repair (Amst)* **2008**, *7*, 1110-1120.
53. Nissanka, N.; Moraes, C.T. Mitochondrial DNA Damage and Reactive Oxygen Species in Neurodegenerative Disease. *FEBS Lett.* **2018**, *592*, 728-742.
54. Imlay, J.A. Iron-Sulphur Clusters and the Problem with Oxygen. *Mol. Microbiol.* **2006**, *59*, 1073-1082.
55. Wallace, M.A.; Liou, L.L.; Martins, J.; Clement, M.H.; Bailey, S.; Longo, V.D.; Valentine, J.S.; Gralla, E.B. Superoxide Inhibits 4Fe-4S Cluster Enzymes Involved in Amino Acid Biosynthesis. Cross-Compartment Protection by Cuzn-Superoxide Dismutase. *J. Biol. Chem.* **2004**, *279*, 32055-32062.
56. Urrutia, P.J.; Mena, N.P.; Nunez, M.T. The Interplay between Iron Accumulation, Mitochondrial Dysfunction, and Inflammation During the Execution Step of Neurodegenerative Disorders. *Front. Pharmacol.* **2014**, *5*, 38.
57. Xu, W.; Barrientos, T.; Andrews, N.C. Iron and Copper in Mitochondrial Diseases. *Cell Metab.* **2013**, *17*, 319-328.

58. Halliwell, B.; Clement, M.V.; Long, L.H. Hydrogen Peroxide in the Human Body. *FEBS Lett.* **2000**, *486*, 10-13.
59. Bienert, G.P.; Schjoerring, J.K.; Jahn, T.P. Membrane Transport of Hydrogen Peroxide. *Biochim. Biophys. Acta* **2006**, *1758*, 994-1003.
60. Liochev, S.L. The Role of Iron-Sulfur Clusters in in Vivo Hydroxyl Radical Production. *Free Radic. Res.* **1996**, *25*, 369-384.
61. Netto, L.E.; Antunes, F. The Roles of Peroxiredoxin and Thioredoxin in Hydrogen Peroxide Sensing and in Signal Transduction. *Mol. Cells* **2016**, *39*, 65-71.
62. Hsu, J.L.; Hsieh, Y.; Tu, C.; O'Connor, D.; Nick, H.S.; Silverman, D.N. Catalytic Properties of Human Manganese Superoxide Dismutase. *J. Biol. Chem.* **1996**, *271*, 17687-17691.
63. Abreu, I.A.; Cabelli, D.E. Superoxide Dismutases-a Review of the Metal-Associated Mechanistic Variations. *Biochim. Biophys. Acta* **2010**, *1804*, 263-274.
64. Sheng, Y.; Abreu, I.A.; Cabelli, D.E.; Maroney, M.J.; Miller, A.F.; Teixeira, M.; Valentine, J.S. Superoxide Dismutases and Superoxide Reductases. *Chem. Rev.* **2014**, *114*, 3854-3918.
65. Hearn, A.S.; Stroupe, M.E.; Cabelli, D.E.; Lepock, J.R.; Tainer, J.A.; Nick, H.S.; Silverman, D.N. Kinetic Analysis of Product Inhibition in Human Manganese Superoxide Dismutase. *Biochemistry* **2001**, *40*, 12051-12058.
66. Costentin, C.; Robert, M.; Saveant, J.M. Concerted Proton-Electron Transfers: Electrochemical and Related Approaches. *Acc. Chem. Res.* **2010**, *43*, 1019-1029.
67. Carneiro, P.; Duarte, M.; Videira, A. Characterization of Apoptosis-Related Oxidoreductases from *Neurospora Crassa*. *PLoS One* **2012**, *7*, e34270.
68. Chang, C.J.; Chang, M.C.; Damrauer, N.H.; Nocera, D.G. Proton-Coupled Electron Transfer: A Unifying Mechanism for Biological Charge Transport, Amino Acid Radical Initiation and Propagation, and Bond Making/Breaking Reactions of Water and Oxygen. *Biochim. Biophys. Acta* **2004**, *1655*, 13-28.
69. Miller, A.F.; Padmakumar, K.; Sorkin, D.L.; Karapetian, A.; Vance, C.K. Proton-Coupled Electron Transfer in Fe-Superoxide Dismutase and Mn-Superoxide Dismutase. *J. Inorg. Biochem.* **2003**, *93*, 71-83.
70. Hearn, A.S.; Fan, L.; Lepock, J.R.; Luba, J.P.; Greenleaf, W.B.; Cabelli, D.E.; Tainer, J.A.; Nick, H.S.; Silverman, D.N. Amino Acid Substitution at the Dimeric Interface of Human Manganese Superoxide Dismutase. *J. Biol. Chem.* **2004**, *279*, 5861-5866.
71. Hearn, A.S.; Stroupe, M.E.; Cabelli, D.E.; Ramilo, C.A.; Luba, J.P.; Tainer, J.A.; Nick, H.S.; Silverman, D.N. Catalytic and Structural Effects of Amino Acid Substitution at Histidine 30 in Human Manganese Superoxide Dismutase: Insertion of Valine C Gamma into the Substrate Access Channel. *Biochemistry* **2003**, *42*, 2781-2789.
72. Hearn, A.S.; Tu, C.; Nick, H.S.; Silverman, D.N. Characterization of the Product-Inhibited Complex in Catalysis by Human Manganese Superoxide Dismutase. *J. Biol. Chem.* **1999**, *274*, 24457-24460.
73. Perry, J.J.; Hearn, A.S.; Cabelli, D.E.; Nick, H.S.; Tainer, J.A.; Silverman, D.N. Contribution of Human Manganese Superoxide Dismutase Tyrosine 34 to Structure and Catalysis. *Biochemistry* **2009**, *48*, 3417-3424.
74. Afanas'ev, I.B.; Kuprianova, N.S. Kinetics and Mechanism of the Reactions of the Superoxide Ion in Solutions. II. The Kinetics of Protonation of the Superoxide Ion by Water and Ethanol. *Int. J. Chem. Kinet.* **1983**, *15*.
75. Carugo, O.; Djinojic Carugo, K. When X-Rays Modify the Protein Structure: Radiation Damage at Work. *Trends Biochem. Sci.* **2005**, *30*, 213-219.
76. Gamarra, D.; Elcoroaristizabal, X.; Fernandez-Martinez, M.; de Pancorbo, M.M. Association of the C47t Polymorphism in Sod2 with Amnesic Mild Cognitive Impairment

- and Alzheimer's Disease in Carriers of the Apoeepsilon4 Allele. *Dis. Markers* **2015**, 2015, 746329.
77. Shimoda-Matsubayashi, S.; Matsumine, H.; Kobayashi, T.; Nakagawa-Hattori, Y.; Shimizu, Y.; Mizuno, Y. Structural Dimorphism in the Mitochondrial Targeting Sequence in the Human Manganese Superoxide Dismutase Gene. A Predictive Evidence for Conformational Change to Influence Mitochondrial Transport and a Study of Allelic Association in Parkinson's Disease. *Biochem. Biophys. Res. Commun.* **1996**, 226, 561-565.
 78. Kim, A. Modulation of Mnsod in Cancer: Epidemiological and Experimental Evidence. *Toxicol Res* **2010**, 26, 83-93.
 79. Borgstahl, G.E.; Parge, H.E.; Hickey, M.J.; Johnson, M.J.; Boissinot, M.; Hallewell, R.A.; Lepock, J.R.; Cabelli, D.E.; Tainer, J.A. Human Mitochondrial Manganese Superoxide Dismutase Polymorphic Variant Ile58thr Reduces Activity by Destabilizing the Tetrameric Interface. *Biochemistry* **1996**, 35, 4287-4297.
 80. Zhang, H.J.; Yan, T.; Oberley, T.D.; Oberley, L.W. Comparison of Effects of Two Polymorphic Variants of Manganese Superoxide Dismutase on Human Breast MCF-7 Cancer Cell Phenotype. *Cancer Res.* **1999**, 59, 6276-6283.
 81. Hernandez-Saavedra, D.; McCord, J.M. Paradoxical Effects of Thiol Reagents on Jurkat Cells and a New Thiol-Sensitive Mutant Form of Human Mitochondrial Superoxide Dismutase. *Cancer Res.* **2003**, 63, 159-163.
 82. Azadmanesh, J.; Trickel, S.R.; Borgstahl, G.E.O. Substrate-Analog Binding and Electrostatic Surfaces of Human Manganese Superoxide Dismutase. *J. Struct. Biol.* **2017**, 199, 68-75.
 83. Salvatori, I.; Valle, C.; Ferri, A.; Carri, M.T. Sirt3 and Mitochondrial Metabolism in Neurodegenerative Diseases. *Neurochem. Int.* **2017**, 109, 184-192.
 84. Kim, H.S.; Patel, K.; Muldoon-Jacobs, K.; Bisht, K.S.; Aykin-Burns, N.; Pennington, J.D.; van der Meer, R.; Nguyen, P.; Savage, J.; Owens, K.M.; Vassilopoulos, A.; Ozden, O.; Park, S.H.; Singh, K.K.; Abdulkadir, S.A.; Spitz, D.R.; Deng, C.X.; Gius, D. Sirt3 Is a Mitochondria-Localized Tumor Suppressor Required for Maintenance of Mitochondrial Integrity and Metabolism During Stress. *Cancer Cell* **2010**, 17, 41-52.
 85. Candas, D.; Li, J.J. Mnsod in Oxidative Stress Response-Potential Regulation Via Mitochondrial Protein Influx. *Antioxid. Redox Signal.* **2014**, 20, 1599-1617.
 86. Edwards, R.A.; Whittaker, M.M.; Whittaker, J.W.; Baker, E.N.; Jameson, G.B. Outer Sphere Mutations Perturb Metal Reactivity in Manganese Superoxide Dismutase. *Biochemistry* **2001**, 40, 15-27.
 87. Leveque, V.J.; Stroupe, M.E.; Lepock, J.R.; Cabelli, D.E.; Tainer, J.A.; Nick, H.S.; Silverman, D.N. Multiple Replacements of Glutamine 143 in Human Manganese Superoxide Dismutase: Effects on Structure, Stability, and Catalysis. *Biochemistry* **2000**, 39, 7131-7137.
 88. Ramilo, C.A.; Leveque, V.; Guan, Y.; Lepock, J.R.; Tainer, J.A.; Nick, H.S.; Silverman, D.N. Interrupting the Hydrogen Bond Network at the Active Site of Human Manganese Superoxide Dismutase. *J. Biol. Chem.* **1999**, 274, 27711-27716.
 89. Quint, P.S.; Domsic, J.F.; Cabelli, D.E.; McKenna, R.; Silverman, D.N. Role of a Glutamate Bridge Spanning the Dimeric Interface of Human Manganese Superoxide Dismutase. *Biochemistry* **2008**, 47, 4621-4628.
 90. Abreu, I.A.; Rodriguez, J.A.; Cabelli, D.E. Theoretical Studies of Manganese and Iron Superoxide Dismutases: Superoxide Binding and Superoxide Oxidation. *J. Phys. Chem. B* **2005**, 109, 24502-24509.
 91. Guan, Y.; Hickey, M.J.; Borgstahl, G.E.O.; Hallewell, R.A.; Lepock, J.R.; O'Connor, D.; Hsieh, Y.; Nick, H.S.; Silverman, D.N.; Tainer, J.A. Crystal Structure of Y34f Mutant Human

- Mitochondrial Manganese Superoxide Dismutase and the Functional Role of Tyrosine 34. *Biochemistry* **1998**, *37*, 4722-4730.
92. Getzoff, E.D.; Tainer, J.A.; Weiner, P.K.; Kollman, P.A.; Richardson, J.S.; Richardson, D.C. Electrostatic Recognition between Superoxide and Copper, Zinc Superoxide Dismutase. *Nature* **1983**, *306*, 287-290.
 93. Lah, M.S.; Dixon, M.M.; Patridge, K.A.; Stallings, W.C.; Fee, J.A.; Ludwig, M.L. Structure-Function in Escherichia Coli Iron Superoxide Dismutase: Comparisons with the Manganese Enzyme from Thermus Thermophilus. *Biochemistry* **1995**, *34*, 1646-1660.
 94. Ludwig, M.L.; Metzger, A.L.; Patridge, K.A.; Stallings, W.C. Manganese Superoxide Dismutase from Thermus Thermophilus. A Structural Model Refined at 1.8 Å Resolution. *J. Mol. Biol.* **1991**, *219*, 335-358.
 95. Tierney, D.L.; Fee, J.A.; Ludwig, M.L.; Penner-Hahn, J.E. X-Ray Absorption Spectroscopy of the Iron Site in Escherichia Coli Fe(III) Superoxide Dismutase. *Biochemistry* **1995**, *34*, 1661-1668.
 96. Bull, C.; Fee, J.A. Steady-State Kinetic Studies of Superoxide Dismutases: Properties of the Iron Containing Protein from Escherichia Coli. *J. Am. Chem. Soc.* **1985**, *107*, 3295-3304.
 97. Misra, H.P.; Fridovich, I. Inhibition of Superoxide Dismutases by Azide. *Arch. Biochem. Biophys.* **1978**, *189*, 317-322.
 98. Hunter, G.J.; Trinh, C.H.; Bonetta, R.; Stewart, E.E.; Cabelli, D.E.; Hunter, T. The Structure of the Caenorhabditis Elegans Manganese Superoxide Dismutase Mnsod-3-Azide Complex. *Protein Sci.* **2015**, *24*, 1777-1788.
 99. Borgstahl, G.E.O.; Pokross, M.; Chehab, R.; Sekher, A.; Snell, E.H. Cryo-Trapping the Six-Coordinate, Distorted-Octahedral Active Site of Manganese Superoxide Dismutase. *J. Mol. Biol.* **2000**, *296*, 951-959.
 100. Whittaker, M.M.; Whittaker, J.W. A "Thermophilic Shift" in Ligand Interactions for Thermus Thermophilus Manganese Superoxide Dismutase. *J. Biol. Inorg. Chem.* **1997**, *2*, 667-671.
 101. Whittaker, M.M.; Whittaker, J.W. Low-Temperature Thermochromism Marks a Change in Coordination for the Metal Ion in Manganese Superoxide Dismutase. *Biochemistry* **1996**, *35*, 6762-6770.
 102. Jackson, T.A.; Karapetian, A.; Miller, A.F.; Brunold, T.C. Spectroscopic and Computational Studies of the Azide-Adduct of Manganese Superoxide Dismutase: Definitive Assignment of the Ligand Responsible for the Low-Temperature Thermochromism. *J. Am. Chem. Soc.* **2004**, *126*, 12477-12491.
 103. Surekha, V.; Byrd, R.A.; Miller, A. Mapping the Effects of Metal Ion Reduction and Substrate Analog Binding to Fe-Superoxide Dismutase by Nmr Spectroscopy. *Magn. Reson. Chem.* **2000**, 5329-5339.
 104. Srnec, M.; Aquilante, F.; Ryde, U.; Rulisek, L. Reaction Mechanism of Manganese Superoxide Dismutase Studied by Combined Quantum and Molecular Mechanical Calculations and Multiconfigurational Methods. *J. Phys. Chem. B* **2009**, 6074-6086.
 105. Leveque, V.J.; Vance, C.K.; Nick, H.S.; Silverman, D.N. Redox Properties of Human Manganese Superoxide Dismutase and Active-Site Mutants. *Biochemistry* **2001**, *40*, 10586-10591.
 106. Noodleman, L.; Lovell, T.; Han, W.G.; Li, J.; Himo, F. Quantum Chemical Studies of Intermediates and Reaction Pathways in Selected Enzymes and Catalytic Synthetic Systems. *Chem. Rev.* **2004**, *104*, 459-508.

107. Li, J.; Fisher, C.L.; Konecny, R.; Bashford, D.; Noodleman, L. Density Functional and Electrostatic Calculations of Manganese Superoxide Dismutase Active Site Complexes in Protein Environments. *Inorg. Chem.* **1999**, *38*, 929-939.
108. Porta, J.; Vahedi-Faridi, A.; Borgstahl, G.E.O. Structural Analysis of Peroxide-Soaked Mnsod Crystals Reveals Side-on Binding of Peroxide to Active-Site Manganese. *J. Mol. Biol.* **2010**, *399*, 377-384.
109. Wintjens, R.; Noel, C.; May, A.C.; Gerbod, D.; Dufernez, F.; Capron, M.; Viscogliosi, E.; Rooman, M. Specificity and Phenetic Relationships of Iron- and Manganese-Containing Superoxide Dismutases on the Basis of Structure and Sequence Comparisons. *J Biol Chem* **2004**, *279*, 9248-9254.
110. Edwards, R.A.; Whittaker, M.M.; Whittaker, J.W.; Baker, E.N.; Jameson, G.B. Removing a Hydrogen Bond in the Dimer Interface of Escherichia Coli Manganese Superoxide Dismutase Alters Structure and Reactivity. *Biochemistry* **2001**, *40*, 4622-4632.
111. Konecny, R.; Li, J.; Fisher, C.L.; Dillet, V.; Bashford, D.; Noodleman, L. Cuzn Superoxide Dismutase Geometry Optimization, Energetics, and Redox Potential Calculations by Density Functional and Electrostatic Methods. *Inorg. Chem.* **1999**, *38*, 940-950.
112. Heimdal, J.; Kaukonen, M.; Srnec, M.; Rulisek, L.; Ryde, U. Reduction Potentials and Acidity Constants of Mn Superoxide Dismutase Calculated by Qm/Mm Free-Energy Method. *Chem. Phys. Chem.* **2011**, 3337-3347.
113. Nielsen, J.E.; McCammon, J.A. Calculating Pka Values in Enzyme Active Sites. *Protein Sci.* **2003**, *12*, 1894-1901.
114. Stallings, W.C.; Metzger, A.L.; Patridge, K.A.; Fee, J.A.; Ludwig, M.L. Structure-Function Relationships in Iron and Manganese Superoxide Dismutases. *Free Radic. Res. Commun.* **1991**, *12-13 Pt 1*, 259-268.
115. Srnec, M.; Aquilante, F.; Ryde, U.; Rulisek, L. Reaction Mechanism of Manganese Superoxide Dismutase Studied by Combined Quantum and Molecular Mechanical Calculations and Multiconfigurational Methods. *The journal of physical chemistry. B* **2009**, *113*, 6074-6086.
116. Rulisek, L.; Jensen, K.P.; Lundgren, K.; Ryde, U. The Reaction Mechanism of Iron and Manganese Superoxide Dismutases Studied by Theoretical Calculations. *Journal of computational chemistry* **2006**, *27*, 1398-1414.
117. Jauncey, G.E. The Scattering of X-Rays and Bragg's Law. *Proc. Natl. Acad. Sci. U. S. A.* **1924**, *10*, 57-60.
118. Shu, F.; Ramakrishnan, V.; Schoenborn, B.P. Enhanced Visibility of Hydrogen Atoms by Neutron Crystallography on Fully Deuterated Myoglobin. *Proc. Natl. Acad. Sci. U. S. A.* **2000**, *97*, 3872-3877.
119. Blakeley, M.P.; Langan, P.; Niimura, N.; Podjarny, A. Neutron Crystallography: Opportunities, Challenges, and Limitations. *Curr. Opin. Struct. Biol.* **2008**, *18*, 593-600.
120. O'Dell, W.B.; Bodenheimer, A.M.; Meilleur, F. Neutron Protein Crystallography: A Complementary Tool for Locating Hydrogens in Proteins. *Arch. Biochem. Biophys.* **2016**, *602*, 48-60.
121. Whittaker, M.M.; Whittaker, J.W. A "Thermophilic Shift" in Ligand Interactions for *Thurmus Thermophilus* Manganese Superoxide Dismutase. *J. Biol. Inorg. Chem.* **1997**, *2*, 667-671.
122. Bull, C.; Fee, J.A. Steady-State Kinetic Studies of Superoxide Dismutases: Properties of the Iron Containing Protein from *Escherichia Coli*. *J. Am. Chem. Soc.* **1985**, *107*, 3295-3304.
123. Steinman, H.M. Construction of an *Escherichia Coli* K-12 Strain Deleted for Manganese and Iron Superoxide Dismutase Genes and Its Use in Cloning the Iron Superoxide

- Dismutase Gene of *Legionella Pneumophila*. *Molecular & general genetics* : MGG **1992**, 232, 427-430.
124. Minor, W.; Cymborowski, M.; Otwinowski, Z.; Chruszcz, M. Hkl-3000: The Integration of Data Reduction and Structure Solution--from Diffraction Images to an Initial Model in Minutes. *Acta Cryst. D* **2006**, 62, 859-866.
 125. Murshudov, G.N.; Skubak, P.; Lebedev, A.A.; Pannu, N.S.; Steiner, R.A.; Nicholls, R.A.; Winn, M.D.; Long, F.; Vagin, A.A. Refmac5 for the Refinement of Macromolecular Crystal Structures. *Acta crystallographica. Section D, Biological crystallography* **2011**, 67, 355-367.
 126. Emsley, P.; Cowtan, K. Coot: Model-Building Tools for Molecular Graphics. *Acta Cryst. D* **2004**, 60, 2126-2132.
 127. Chen, V.B.; Arendall, W.B., 3rd; Headd, J.J.; Keedy, D.A.; Immormino, R.M.; Kapral, G.J.; Murray, L.W.; Richardson, J.S.; Richardson, D.C. Molprobity: All-Atom Structure Validation for Macromolecular Crystallography. *Acta Cryst. D* **2010**, 66, 12-21.
 128. Dolinsky, T.J.; Czodrowski, P.; Li, H.; Nielsen, J.E.; Jensen, J.H.; Klebe, G.; Baker, N.A. Pdb2pqr: Expanding and Upgrading Automated Preparation of Biomolecular Structures for Molecular Simulations. *Nucleic Acids Res.* **2007**, 35, W522-525.
 129. Neves, R.P.; Sousa, S.F.; Fernandes, P.A.; Ramos, M.J. Parameters for Molecular Dynamics Simulations of Manganese-Containing Metalloproteins. *J. Chem. Theory Comput.* **2013**, 9, 2718-2732.
 130. Baker, N.A.; Sept, D.; Joseph, S.; Holst, M.J.; McCammon, J.A. Electrostatics of Nanosystems: Application to Microtubules and the Ribosome. *Proc. Natl. Acad. Sci. U. S. A.* **2001**, 98, 10037-10041.
 131. Borgstahl, G.E.; Parge, H.E.; Hickey, M.J.; Beyer, W.F., Jr.; Hallewell, R.A.; Tainer, J.A. The Structure of Human Mitochondrial Manganese Superoxide Dismutase Reveals a Novel Tetrameric Interface of Two 4-Helix Bundles. *Cell* **1992**, 71, 107-118.
 132. Tabares, L.C.; Cortez, N.; Hiraoka, B.Y.; Yamakura, F.; Un, S. Effects of Substrate Analogues and Ph on Manganese Superoxide Dismutases. *Biochemistry* **2006**, 45, 1919-1929.
 133. Borgstahl, G.E.; Pokross, M.; Chehab, R.; Sekher, A.; Snell, E.H. Cryo-Trapping the Six-Coordinate, Distorted-Octahedral Active Site of Manganese Superoxide Dismutase. *Journal of molecular biology* **2000**, 296, 951-959.
 134. Getzoff, E.D.; Tainer, J.A.; Weiner, P.K.; Kollman, P.A.; Richardson, J.S.; Richardson, D.C. Electrostatic Recognition between Superoxide and Copper, Zinc Superoxide Dismutase. *Nature* **1983**, 306, 287-290.
 135. Whittaker, M.M.; Whittaker, J.W. A Glutamate Bridge Is Essential for Dimer Stability and Metal Selectivity in Manganese Superoxide Dismutase. *The Journal of biological chemistry* **1998**, 273, 22188-22193.
 136. Chan, V.W.; Bjerrum, M.J.; Borders, C.L., Jr. Evidence That Chemical Modification of a Positively Charged Residue at Position 189 Causes the Loss of Catalytic Activity of Iron-Containing and Manganese-Containing Superoxide Dismutases. *Archives of biochemistry and biophysics* **1990**, 279, 195-201.
 137. Borders, C.L., Jr.; Chan, V.W.; Bjerrum, M.J. The Positive Charge at Position 189 Is Essential for the Catalytic Activity of Iron- and Manganese-Containing Superoxide Dismutases. *Free radical research communications* **1991**, 12-13 Pt 1, 279-285.
 138. Ozden, O.; Park, S.H.; Kim, H.S.; Jiang, H.; Coleman, M.C.; Spitz, D.R.; Gius, D. Acetylation of Mnsod Directs Enzymatic Activity Responding to Cellular Nutrient Status or Oxidative Stress. *Aging* **2011**, 3, 102-107.

139. Sarsour, E.H.; Kalen, A.L.; Goswami, P.C. Manganese Superoxide Dismutase Regulates a Redox Cycle within the Cell Cycle. *Antioxidants & redox signaling* **2014**, *20*, 1618-1627.
140. Qiu, X.; Brown, K.; Hirschey, M.D.; Verdin, E.; Chen, D. Calorie Restriction Reduces Oxidative Stress by Sirt3-Mediated Sod2 Activation. *Cell Metab.* **2010**, *12*, 662-667.
141. Tao, R.; Coleman, M.C.; Pennington, J.D.; Ozden, O.; Park, S.H.; Jiang, H.; Kim, H.S.; Flynn, C.R.; Hill, S.; Hayes McDonald, W.; Olivier, A.K.; Spitz, D.R.; Gius, D. Sirt3-Mediated Deacetylation of Evolutionarily Conserved Lysine 122 Regulates Mnsod Activity in Response to Stress. *Molecular cell* **2010**, *40*, 893-904.
142. Sarsour, E.H.; Kalen, A.L.; Xiao, Z.; Veenstra, T.D.; Chaudhuri, L.; Venkataraman, S.; Reigan, P.; Buettner, G.R.; Goswami, P.C. Manganese Superoxide Dismutase Regulates a Metabolic Switch During the Mammalian Cell Cycle. *Cancer Res.* **2012**, *72*, 3807-3816.
143. Ramilo, C.A.; Leveque, V.; Guan, Y.; Lepock, J.R.; Tainer, J.A.; Nick, H.S.; Silverman, D.N. Interrupting the Hydrogen Bond Network at the Active Site of Human Manganese Superoxide Dismutase*. *J Biol Chem* **1999**, 274.
144. Greenleaf, W.B.; Perry, J.J.; Hearn, A.S.; Cabelli, D.E.; Lepock, J.R.; Stroupe, M.E.; Tainer, J.A.; Nick, H.S.; Silverman, D.N. Role of Hydrogen Bonding in the Active Site of Human Manganese Superoxide Dismutase. *Biochemistry* **2004**, *43*, 7038-7045.
145. Larsson, G.; Tornkvist, M. Rapid Sampling, Cell Inactivation and Evaluation of Low Extracellular Glucose Concentrations During Fed-Batch Cultivation. *J. Biotechnol.* **1996**, *49*, 69-82.
146. Holme, T.; Arvidson, S.; Lindholm, B.; Pavlu, B. Enzymes--Laboratory-Scale Production. *Process Biochem.* **1970**, *5*, 62-66.
147. Meilleur, F.; Weiss, K.L.; Myles, D.A. Deuterium Labeling for Neutron Structure-Function-Dynamics Analysis. *Methods Mol Biol* **2009**, *544*, 281-292.
148. Cold Spring Harbor Lab, N.Y. Preparation of 0.1 M Potassium Phosphate Buffer at 25°C. *Cold Spring Harb Protoc* **2006**.
149. Coates, L.; Stoica, A.D.; Hoffmann, C.; Richards, J.; Cooper, R. The Macromolecular Neutron Diffractometer (Mandi) at the Spallation Neutron Source, Oak Ridge: Enhanced Optics Design, High-Resolution Neutron Detectors and Simulated Diffraction. *J Appl Crystallogr* **2010**, *43*, 570-577.
150. Coates, L.; Cuneo, M.J.; Frost, M.J.; He, J.; Weiss, K.L.; Tomanicek, S.J.; McFeeters, H.; Vandavasi, V.G.; Langan, P.; Iverson, E.B. *J Appl Crystallogr* **2015**, *48*, 1302-1306.
151. Arnold, O.; Bilheux, J.C.; Borreguero, J.M.; Buts, A.; Campbell, S.I.; Chapon, L.; Doucet, M.; Draper, N.; Leal, R.F.; Gigg, M.A.; Lynch, V.E.; Markyadsen, A.; Mikkelsen, D.J.; Mikkelsen, R.L.; Miller, R.; Palmen, K.; Parker, P.; Passos, G.; Perring, T.G.; Peterson, P.F.; Ren, S.; Reuter, M.A.; Sayici, A.T.; Taylor, J.W.; Taylor, R.J.; Tolchenoy, R.; Zhou, W.; Zikowsky, J. Mantid-Data Analysis and Visualization Package for Neutron Scattering and Mu Sr Experiments. *Nucl Instrum Meth A* **2014**, *764*, 156-166.
152. Campbell, J.W.; Hao, Q.; Harding, M.M.; Nguti, N.D.; Wilkinson, C. Lauegen Version 6.0 and Intldm. *J Appl Crystallogr* **1998**, *31*, 496-502.
153. Kabsch, W. *Acta Cryst D* **2010**, *66*, 125-132.
154. Winn, M.D.; Ballard, C.C.; Cowtan, K.D.; Dodson, E.J.; Emsley, P.; Evans, P.R.; Keegan, R.M.; Krissinel, E.B.; Leslie, A.G.; McCoy, A.; McNicholas, S.J.; Murshudov, G.N.; Pannu, N.S.; Potterton, E.A.; Powell, H.R.; Read, R.J.; Vagin, A.; Wilson, K.S. Overview of the Ccp4 Suite and Current Developments. *Acta Cryst. D* **2011**, *67*, 235-242.
155. Blakeley, M.P. Neutron Macromolecular Crystallography. *Crystallogr. Rev.* **2011**, *15*, 157-218.

156. Langan, P.; Fisher, Z.; Kovalevsky, A.; Mustyakimov, M.; Sutcliffe Valone, A.; Unkefer, C.; Waltman, M.J.; Coates, L.; Adams, P.D.; Afonine, P.V.; Bennett, B.; Dealwis, C.; Schoenborn, B.P. Protein Structures by Spallation Neutron Crystallography. *J. Synchrotron. Radiat.* **2008**, *15*, 215-218.
157. Azadmanesh, J.; Borgstahl, G.E.O. A Review of the Catalytic Mechanism of Human Manganese Superoxide Dismutase. *Antioxidants (Basel)* **2018**, *7*.
158. Maliekal, J.; Karapetian, A.; Vance, C.; Yikilmaz, E.; Wu, Q.; Jackson, T.; Brunold, T.C.; Spiro, T.G.; Miller, A.F. Comparison and Contrasts between the Active Site Pks of Mn-Superoxide Dismutase and Those of Fe-Superoxide Dismutase. *J. Am. Chem. Soc.* **2002**, *124*, 15064-15075.
159. Golden, E.A.; Vrielink, A. *Aust. J. Chem.* **2014**, *67*, 1751-1762.
160. Hale, G.M.; Dodder, D.C.; Seagrave, J.D.; Berman, B.L.; Phillips, T.W. Neutron-Triton Cross Sections and Scattering Lengths Obtained from P-3He Scattering. *Phys. Rev. C Nucl. Phys.* **1990**, *42*, 438-440.
161. Rulisek, L.; Ryde, U. Structure of Reduced and Oxidized Manganese Superoxide Dismutase: A Combined Computational and Experimental Approach. *J. Phys. Chem. B* **2006**, *110*, 11511-11518.
162. Schaffner, I.; Mlynek, G.; Flego, N.; Puhlinger, D.; Libiseller-Egger, J.; Coates, L.; Hofbauer, S.; Bellei, M.; Furtmuller, P.G.; Battistuzzi, G.; Smulevich, G.; Djinojic Carugo, K.; Obinger, C. *ACS Catal.* **2017**, *7*, 7962-7976.
163. Azadmanesh, J.; Trickel, S.R.; Weiss, K.L.; Coates, L.; Borgstahl, G.E.O. Preliminary Neutron Diffraction Analysis of Challenging Human Manganese Superoxide Dismutase Crystals. *Acta Cryst. F* **2017**, *73*, 235-240.
164. Coates, L.; Stoica, A.D.; Hoffmann, C.; Richards, J.; Cooper, R. The Macromolecular Neutron Diffractometer (Mandi) at the Spallation Neutron Source, Oak Ridge: Enhanced Optics Design, High-Resolution Neutron Detectors and Simulated Diffraction. *J. Appl. Crystallogr.* **2010**, *43*, 570-577.
165. Coates, L.; Cuneo, M.J.; Frost, M.J.; He, J.; Weiss, K.L.; Tomanicek, S.J.; McFeeters, H.; Vandavasi, V.G.; Langan, P.; Iverson, E.B. The Macromolecular Neutron Diffractometer Mandi at the Spallation Neutron Source. *J. Appl. Crystallogr.* **2015**, *48*, 1302-1306.
166. Sheng, Y.; Butler Gralla, E.; Schumacher, M.; Cascio, D.; Cabelli, D.E.; Valentine, J.S. Six-Coordinate Manganese(3+) in Catalysis by Yeast Manganese Superoxide Dismutase. *Proc. Natl. Acad. Sci. U. S. A.* **2012**, *109*, 14314-14319.
167. Sheng, Y.; Durazo, A.; Schumacher, M.; Gralla, E.B.; Cascio, D.; Cabelli, D.E.; Valentine, J.S. Tetramerization Reinforces the Dimer Interface of Mnsod. *PLoS One* **2013**, *8*, e62446.
168. Law, N.A.; Caudle, M.T.; Pecoraro, V.L. Manganese Redox Enzymes and Model Systems: Properties, Structures, and Reactivity. *Adv. Inorg. Chem.* **1998**, *46*, 305-440.
169. Whittaker, J.W.; Whittaker, M.M. Active Site and Spectral Studies on Manganese Superoxide Dismutase. *J. Am. Chem. Soc.* **1991**, *113*, 5528-5540.
170. Arnold, O.; Bilheux, J.C.; Borreguero, J.M.; Buts, A.; Campbell, S.I.; Chapon, L.; Doucet, M.; Draper, N.; Leal, R.F.; Gigg, M.A.; Lynch, V.E.; Markyarden, A.; Mikkelsen, D.J.; Mikkelsen, R.L.; Miller, R.; Palmen, K.; Parker, P.; Passos, G.; Perring, T.G.; Peterson, P.F.; Ren, S.; Reuter, M.A.; Sayici, A.T.; Taylor, J.W.; Taylor, R.J.; Tolchenoy, R.; Zhou, W.; Zikoysky, J. Mantid—Data Analysis and Visualization Package for Neutron Scattering and M Sr Experiments. *Nucl. Instrum. Meth. A* **2014**, *764*, 156-166.
171. Campbell, J.W. Lauegen, an X-Windows-Based Program for the Processing of Laue Diffraction Data. *J. Appl. Crystallogr.* **1995**, *28*, 228-236.

172. Campbell, J.W.; Hao, Q.; Harding, M.M.; Nguti, N.D.; Wilkinson, C. *J. Appl. Crystallogr.* **1998**, *31*, 496-502.
173. Ranguelova, K.; Ganini, D.; Bonini, M.G.; London, R.E.; Mason, R.P. Kinetics of the Oxidation of Reduced Cu,Zn-Superoxide Dismutase by Peroxymonocarbonate. *Free Radic. Biol. Med.* **2012**, *53*, 589-594.
174. Chen, J.C.; Hanson, B.L.; Fisher, S.Z.; Langan, P.; Kovalevsky, A.Y. Direct Observation of Hydrogen Atom Dynamics and Interactions by Ultrahigh Resolution Neutron Protein Crystallography. *Proc. Natl. Acad. Sci. U. S. A.* **2012**, *109*, 15301-15306.
175. Buhl, M. Structure, Dynamics, and Magnetic Shieldings of Permanganate Ion in Aqueous Solution. A Density Functional Study. *J. Phys. Chem. A* **2002**, *106*, 10505-10509.
176. Weinrach, J.B.; Meyer, D.R.; Guy, J.T.; Michalski, P.E.; Carter, K.L.; Grubisha, D.S.; Bennett, D.W. *J. Cryst. Spec. Rsrch.* **1992**, *22*, 291-301.
177. Finnegan, M.; Linley, E.; Denyer, S.P.; McDonnell, G.; Simons, C.; Maillard, J.Y. Mode of Action of Hydrogen Peroxide and Other Oxidizing Agents: Differences between Liquid and Gas Forms. *J. Antimicrob. Chemother.* **2010**, *65*, 2108-2115.
178. Casadei, C.M.; Gumiero, A.; Metcalfe, C.L.; Murphy, E.J.; Basran, J.; Concilio, M.G.; Teixeira, S.C.; Schrader, T.E.; Fielding, A.J.; Ostermann, A.; Blakeley, M.P.; Raven, E.L.; Moody, P.C. Heme Enzymes. Neutron Cryo-Crystallography Captures the Protonation State of Ferryl Heme in a Peroxidase. *Science* **2014**, *345*, 193-197.
179. Li, L.; Shukla, S.; Meilleur, F.; Standaert, R.F.; Pierce, J.; Myles, D.A.A.; Cuneo, M.J. Neutron Crystallographic Studies of T4 Lysozyme at Cryogenic Temperature. *Protein Sci.* **2017**, *26*, 2098-2104.
180. Coates, L.; Tomanicek, S.J.; Schrader, T.E.; Weiss, K.L.; Ng, J.D.; Juttner, P.; Ostermann, A. *J. Appl. Crystallogr.* **2014**, *47*, 1431-1434.
181. Afonine, P.V.; Mustyakimov, M.; Grosse-Kunstleve, R.W.; Moriarty, N.W.; Langan, P.; Adams, P.D. Joint X-Ray and Neutron Refinement with Phenix.Refine. *Acta Cryst. D* **2010**, *66*, 1153-1163.
182. Wallace, D.C. Mitochondria and Cancer. *Nat. Rev. Cancer* **2012**, *12*, 685-698.
183. Xu, F. Applications of Oxidoreductases: Recent Progress. *Industrial Biotechnology* **2015**, *1*, 38-50.
184. Batinic-Haberle, I.; Reboucas, J.S.; Spasojevic, I. Superoxide Dismutase Mimics: Chemistry, Pharmacology, and Therapeutic Potential. *Antioxid. Redox Signal.* **2010**, *13*, 877-918.
185. Pinero, J.; Bravo, A.; Queralt-Rosinach, N.; Gutierrez-Sacristan, A.; Deu-Pons, J.; Centeno, E.; Garcia-Garcia, J.; Sanz, F.; Furlong, L.I. Disgenet: A Comprehensive Platform Integrating Information on Human Disease-Associated Genes and Variants. *Nucleic Acids Res.* **2017**, *45*, D833-D839.
186. Valenti, L.; Conte, D.; Piperno, A.; Dongiovanni, P.; Fracanzani, A.L.; Fraquelli, M.; Vergani, A.; Gianni, C.; Carmagnola, L.; Fargion, S. The Mitochondrial Superoxide Dismutase A16v Polymorphism in the Cardiomyopathy Associated with Hereditary Haemochromatosis. *J. Med. Genet.* **2004**, *41*, 946-950.
187. Whittaker, M.M.; Whittaker, J.W. Metallation State of Human Manganese Superoxide Dismutase Expressed in *Saccharomyces Cerevisiae*. *Arch. Biochem. Biophys.* **2012**, *523*, 191-197.
188. Azadmanesh, J.; Lutz, W.E.; Weiss, K.L.; Coates, L.; Borgstahl, G.E.O. Redox Manipulation of the Manganese Metal in Human Manganese Superoxide Dismutase for Neutron Diffraction. *Acta Cryst. F* **2018**, *74*, 677-687.

189. Sullivan, B.; Archibald, R.; Azadmanesh, J.; Vandavasi, V.G.; Langan, P.S.; Coates, L.; Lynch, V.; Langan, P. Braggnet: Integrating Bragg Peaks Using Neural Networks. *J. Appl. Crystallogr.* **2019**, *52*, 854-863.
190. Afonine, P.V.; Grosse-Kunstleve, R.W.; Echols, N.; Headd, J.J.; Moriarty, N.W.; Mustyakimov, M.; Terwilliger, T.C.; Urzhumtsev, A.; Zwart, P.H.; Adams, P.D. Towards Automated Crystallographic Structure Refinement with Phenix.Refine. *Acta Cryst. D* **2012**, *68*, 352-367.
191. Papas, B.N.; Schaefer III, H.F. Concerning the Precision of Standard Density Functional Programs: Gaussian, Molpro, Nwchem, Q-Chem, and Gamess. *Comput. Theor. Chem.* **2006**, *768*, 175-181.
192. Wheeler, S.E.; Houk, K.N. Integration Grid Errors for Meta-Gga-Predicted Reaction Energies: Origin of Grid Errors for the M06 Suite of Functionals. *J. Chem. Theory Comput.* **2010**, *6*, 395-404.
193. Valiev, M.; Bylaska, E.J.; Govind, N.; Kowalski, K.; Straatsma, T.P.; Van Dam, H.J.J.; Wang, D.; Nieplocha, J.; Apra, E.; Windus, T.L.; De Jong, W.A. Nwchem: A Comprehensive and Scalable Open-Source Solution for Large Scale Molecular Simulation. *Comput. Phys. Commun.* **2010**, *181*, 1477-1489.
194. Grimme, S.; Ehrlich, S.; Goerigk, L. Effect of the Damping Function in Dispersion Corrected Density Functional Theory. *J. Comput. Chem.* **2011**, *32*, 1456-1465.
195. Becke, A.D. Becke's Three Parameter Hybrid Method Using the Lyp Correlation Functional. *J. Chem. Phys.* **1993**, *98*, 5648.
196. Klamt, A. Conductor-Like Screening Model for Real Solvents: A New Approach to the Quantitative Calculation of Solvation Phenomena. *J. Phys. Chem.* **1995**, *99*, 2224-2235.
197. Thapa, B.; Schlegel, H.B. Density Functional Theory Calculation of Pka's of Thiols in Aqueous Solution Using Explicit Water Molecules and the Polarizable Continuum Model. *J. Phys. Chem. A* **2016**, *120*, 5726-5735.
198. Zhang, S.; Baker, J.; Pulay, P. A Reliable and Efficient First Principles-Based Method for Predicting Pk(a) Values. 1. Methodology. *J. Phys. Chem. A* **2010**, *114*, 425-431.
199. Vance, C.K.; Miller, A.F. Novel Insights into the Basis for Escherichia Coli Superoxide Dismutase's Metal Ion Specificity from Mn-Substituted Fesod and Its Very High E(M). *Biochemistry* **2001**, *40*, 13079-13087.
200. Nikolaienko, T.Y.; Bulavin, L.A.; Hovorun, D.M. Janpa: An Open Source Cross-Platform Implementation of the Natural Population Analysis on the Java Platform. *Comput. Theor. Chem.* **2010**, *1050*, 15-22.
201. Nikolaienko, T.Y.; Bulavin, L.A. Localized Orbitals for Optimal Decomposition of Molecular Properties. *Int. J. Quantum Chem.* **2019**, *119*, e25798.
202. Nikolaienko, T.Y.; Chuiko, V.S.; Bulavin, L.A. The Dataset of Covalent Bond Lengths Resulting from the First-Principle Calculations. *Comput. Theor. Chem.* **2019**, *1163*, 112508.
203. Nikolaienko, T.Y.; Bulavin, L.A.; Hovorun, D.M. Can We Treat Ab Initio Atomic Charges and Bond Orders as Conformation-Independent Electronic Structure Descriptors? *RSC Advances* **2016**, *6*, 74785-74796.
204. Nikolaienko, T.Y. The Maximum Occupancy Condition for the Localized Property-Optimized Orbitals. *Phys. Chem. Chem. Phys.* **2019**, *21*, 5285-5294.
205. Glendening, E.D.; Landis, C.R.; Weinhold, F. Nbo 7.0: New Vistas in Localized and Delocalized Chemical Bonding Theory. *J. Comput. Chem.* **2019**, *40*, 2234-2241.
206. Nikolaienko, T.Y.; S., K.E.; Dolgonos, G.A. On the Existence of He-He Bond in the Endohedral Fullerene He2@ C60. *J. Comput. Chem.* **2018**, *39*, 1090-1102.

207. Reed, A.E.; Curtiss, L.A.; Weinhold, F. Intermolecular Interactions from a Natural Bond Orbital, Donor-Acceptor Viewpoint. *Chem. Rev.* **1988**, *88*, 899-926.
208. Rulisek, L.; Jensen, K.P.; Lundgren, K.; Ryde, U. The Reaction Mechanism of Iron and Manganese Superoxide Dismutases Studied by Theoretical Calculations. *J. Comput. Chem.* **2006**, *27*.
209. Han, W.G.; Lovell, T.; Noodleman, L. Coupled Redox Potentials in Manganese and Iron Superoxide Dismutases from Reaction Kinetics and Density Functional/Electrostatics Calculations. *Inorg. Chem.* **2002**, *41*, 205-218.
210. Heimdal, J.; Kaukonen, M.; Srnec, M.; Rulisek, L.; Ryde, U. Reduction Potentials and Acidity Constants of Mn Superoxide Dismutase Calculated by Qm/Mm Free-Energy Methods. *Chemphyschem* **2011**, *12*, 3337-3347.
211. Remer, L.C.; Jensen, J.H. Toward a General Theory of Hydrogen Bonding: The Short, Strong Hydrogen Bond. *J. Phys. Chem. A* **2000**, *104*, 9266-9275.
212. Gerlt, J.A.; Kreevoy, M.M.; Cleland, W.; Frey, P.A. Understanding Enzymic Catalysis: The Importance of Short, Strong Hydrogen Bonds. *Chem. Biol.* **1997**, *4*, 259-267.
213. Kumar, P.; Agarwal, P.K.; Cuneo, M.J. On the Case of the Misplaced Hydrogens. *ChemBioChem* **2020**.
214. Eriksson, M.A.; Hard, T.; Nilsson, L. On the Ph Dependence of Amide Proton Exchange Rates in Proteins. *Biophys. J.* **1995**, *69*, 329-339.
215. Malwal, S.R.; Gao, J.; Hu, X.; Yang, Y.; Liu, W.; Huang, J.W.; Ko, T.P.; Li, L.; Chen, C.C.; O'Dowd, B.; Khade, R.L.; Zhang, Y.; Zhang, Y.; Oldfield, E.; Guo, R.T. Catalytic Role of Conserved Asparagine, Glutamine, Serine, and Tyrosine Residues in Isoprenoid Biosynthesis Enzymes. *ACS Catal.* **2018**, *8*, 4299-4312.
216. Nakamura, A.; Ishida, T.; Kusaka, K.; Yamada, T.; Fushinobu, S.; Tanaka, I.; Kaneko, S.; Ohta, K.; Tanaka, H.; Inaka, K.; Higuchi, Y.; Niimura, N.; Samejima, M.; Igarashi, K. "Newton's Cradle" Proton Relay with Amide-Imidic Acid Tautomerization in Inverting Cellulase Visualized by Neutron Crystallography. *Sci Adv* **2015**, *1*, e1500263.
217. Grigorenko, B.L.; Khrenova, M.G.; Nemukhin, A.V. Amide-Imide Tautomerization in the Glutamine Side Chain in Enzymatic and Photochemical Reactions in Proteins. *Phys. Chem. Chem. Phys.* **2018**, *20*, 23827-23836.
218. Hsieh, Y.; Guan, Y.; Tu, C.; Bratt, P.J.; Angerhofer, A.; Lepock, J.R.; Hickey, M.J.; Tainer, J.A.; Nick, H.S.; Silverman, D.N. Probing the Active Site of Human Manganese Superoxide Dismutase: The Role of Glutamine 143. *Biochemistry* **1998**, *37*, 4731-4739.
219. Cabelli, D.E.; Guan, Y.; Leveque, V.; Hearn, A.S.; Tainer, J.A.; Nick, H.S.; Silverman, D.N. Role of Tryptophan 161 in Catalysis by Human Manganese Superoxide Dismutase. *Biochemistry* **1999**, *38*, 11686-11692.
220. Michalczyk, R.; Unkefer, C.J.; Bacik, J.P.; Schrader, T.E.; Ostermann, A.; Kovalevsky, A.Y.; McKenna, R.; Fisher, S.Z. Joint Neutron Crystallographic and Nmr Solution Studies of Tyr Residue Ionization and Hydrogen Bonding: Implications for Enzyme-Mediated Proton Transfer. *Proc. Natl. Acad. Sci. U. S. A.* **2015**, *112*, 5673-5678.
221. MacMillan-Crow, L.A.; Thompson, J.A. Tyrosine Modifications and Inactivation of Active Site Manganese Superoxide Dismutase Mutant (Y34f) by Peroxynitrite. *Arch. Biochem. Biophys.* **1999**, *366*, 82-88.
222. Walba, H.; Isensee, R.W. Acidity Constants of Some Arylimidazoles and Their Cations. *J. Org. Chem.* **1961**, *26*, 2789-2791.
223. Dodson, G.; Wlodawer, A. Catalytic Triads and Their Relatives. *Trends Biochem. Sci.* **1998**, *23*, 347-352.

- 224. Styring, S.; Sjöholm, J.; Mamedov, F. Two Tyrosines That Changed the World: Interfacing the Oxidizing Power of Photochemistry to Water Splitting in Photosystem II. *Biochim. Biophys. Acta* **2012**, *1817*, 76-87.
- 225. Ehrig, T.; Hurley, T.D.; Edenberg, H.J.; Bosron, W.F. General Base Catalysis in a Glutamine for Histidine Mutant at Position 51 of Human Liver Alcohol Dehydrogenase. *Biochemistry* **1991**, *30*, 1062-1068.
- 226. Lu, J.; Zhang, H.; Chen, X.; Zou, Y.; Li, J.; Wang, L.; Wu, M.; Zang, J.; Yu, Y.; Zhuang, W.; Xia, Q.; Wang, J. A Small Molecule Activator of Sirt3 Promotes Deacetylation and Activation of Manganese Superoxide Dismutase. *Free Radic. Biol. Med.* **2017**, *112*, 287-297.
- 227. Zhu, Y.; Zou, X.; Dean, A.E.; Brien, J.O.; Gao, Y.; Tran, E.L.; Park, S.H.; Liu, G.; Kieffer, M.B.; Jiang, H.; Stauffer, M.E.; Hart, R.; Quan, S.; Satchell, K.J.F.; Horikoshi, N.; Bonini, M.; Gius, D. Lysine 68 Acetylation Directs Mnsod as a Tetrameric Detoxification Complex Versus a Monomeric Tumor Promoter. *Nat Commun* **2019**, *10*, 2399.
- 228. Jackson, T.A.; Karapetian, A.; Miller, A.F.; Brunold, T.C. Probing the Geometric and Electronic Structures of the Low-Temperature Azide Adduct and the Product-Inhibited Form of Oxidized Manganese Superoxide Dismutase. *Biochemistry* **2005**, *44*, 1504-1520.